THE UNIVERSITY OF CHICAGO

MULTI-MODAL VALIDATION OF MR MICROSTRUCTURE IMAGING IN THE MOUSE BRAIN

A DISSERTATION SUBMITTED TO
THE FACULTY OF THE DIVISION OF THE BIOLOGICAL SCIENCES
AND THE PRITZKER SCHOOL OF MEDICINE
IN CANDIDACY FOR THE DEGREE OF
DOCTOR OF PHILOSOPHY

COMMITTEE ON MEDICAL PHYSICS

BY
TIMOTHY SCOTT TRINKLE

CHICAGO, ILLINOIS
DECEMBER 2021

To my family.

Contents

List of Figures

List of Tables

ACKNOWLEDGMENTS

The work presented in this dissertation would not have been possible without the assistance and support of a number of people I would like to thank here. I am very grateful to have worked under the guidance of my advisor Patrick La Rivière. Patrick is a truly inspiring and creative scientist who has been a continually encouraging teacher, mentor, friend, and fellow coffee enthusiast during my time at the University of Chicago. Sean Foxley collected all MRI data presented in this dissertation and directly supervised the work presented in Chapter 4. He also served with Sam Armato and Tim Carroll on my thesis committee; I would like to thank all three of them for their valuable feedback and suggestions. Bobby Kasthuri, Vandana Sampathkumar, and others in the Kasthuri Lab acquired the microCT and electron microscopy data used in chapter 2, and assisted with sample preparation for MRI data used in chapters 3 and 4. I would also like to thank Răzvan Gămănuţ and Henry Kennedy for sharing additional tracer data for work presented in Chapter 3.

Insights from discussions with Talon Chandler made their way into nearly every page of this dissertation. I would like to thank him for his constant encouragement, advice, and friendship, for yelling about Python and Emacs from day one, and for many car rides to the rock climbing gym. Phil Vargas, Dimple Modgil, Bryan Quigley, Corey Smith, Ben Preusser, Hadley Smith, Geneva Schlafly, Nikolaj Reiser, Baiyang Dai, Chineze Egwudo, and all rotating members of the La Rivière lab have also helped foster a supportive, collaborative research environment and have been a pleasure to work with.

Sam Hendley, Adam Hasse, and Jennie Crosby were phenomenal classmates, friends, and fellow travelers with me on a particularly unpleasant afternoon on Martha's Vineyard. I would like to thank the three of them as well as Neville Eclov, Eyjólfur Guðmundsson, Kayla Robinson, Joe Foy, Jordan Fuhrman, Isabelle Hu, Brittany Broder, Lindsay Douglas, Linnea Kremer, Mira Liu, Natalie Baughan, Julian Bertini, Mena Shenouda, Andrew McVea, Madeleine Durkee, and other current and former members of the GPMP community for

friendship, journal clubs, and lunch breaks at the duck pond.

I would like to thank Ruth Magaña, Julie Hlavaty, Hoang Ngo, Maya Suraj and Elena Rizzo for providing valuable administrative assistance, as well as Chun-Wai Chan for helpful computational support.

Throughout my academic career, I have benefited from the instruction of multiple exceptional teachers. I would like to specifically thank Joel Adams, Rajasekhar Narisetty, and Richard Horner, all of whom introduced me to subjects and modes of analysis that continue to deeply shape how I think.

My time at the University of Chicago would not have been nearly as enjoyable without the friendship of Inna Gertsenshteyn and Zion Rodman, I would like to thank them for many coffee breaks, walks, movie nights, and open mics, as well as their cats Obie and Pushkin for their unwavering support. Amar Risbud has been a great friend and roommate while completing this research from home through quarantines and lockdowns. I would like to specifically thank him for multiple much-needed rewatches of *Stop Making Sense*. I would also like to thank Will Deyo, Logan Greenhaw, and Jessica Alvarez for their multiple phone calls, visits, and lifelong friendship.

Finally, I want to thank Tim and Cheryl, my parents and earliest teachers, as well as Caitlyn, Bryan, Matthew, Jack, Jones, and Leonora for their constant love and support.

This work was supported by funds from the National Institutes of Health under grants F31NS113571, U01MH109100, R01EB026300, EB026300, S10OD025081, S10RR021039, and P30CA14599. This research also used resources of the Advanced Photon Source and Argonne Leadership Computing Facility, both of which are U.S. Department of Energy (DOE) Office of Science User Facilities operated for the DOE Office of Science by Argonne National Laboratory: contract No. DE-AC02-06CH11357.

ABSTRACT

The mammalian nervous system consists of a complicated network of biological structures, with functional subsystems constrained by a structural architecture that operates at scales spanning many orders of spatial magnitude. Our understanding of the architecture of the brain has been mediated through developments in biological imaging, though all imaging approaches are constrained by tradeoffs in achievable resolution, sensitivity, and field of view. Electron microscopy can be used to image nano-scale synapses, but only across small volumes, while magnetic resonance imaging (MRI) can be used to image whole brains but with spatial resolutions more coarse by several orders of magnitude.

Developments in MR microstructural imaging methods such as diffusion MRI (dMRI) and echo-planar spectroscopic imaging (EPSI) help bridge the resolution and field of view gap by estimating cellular properties such as fiber orientations, myelin integrity, and long-range connectivity across the brain using clinically feasible acquisition sequences. These MR approaches rely on biophysical signal models to reconstruct sub-resolution properties of the underlying tissue. The theme of this dissertation is the development of tools and analysis methods used to perform multi-modal validation studies for these MR microstructural imaging models in the mouse brain, with specific focus on dMRI reconstructions and tractography.

First, we demonstrate the utility of whole-brain synchrotron microcomputed tomography as a validation modality for the estimation of nerve fiber orientations with dMRI. MicroCT provides isotropic resolution across whole mouse brains with no physical sectioning, addressing limitations in existing optical-based dMRI validation methods. Computer vision tools were developed to estimate fiber orientations that were spatially registered to dMRI data of the same specimen. Comparisons between modalities show good agreement in the representation of local fiber geometries and long-range trajectories, demonstrating the utility of synchrotron microCT for future dMRI validation studies. Furthermore, we show that

microCT is compatible with follow-up electron microscopy, forming a multi-modal imaging pipeline capable of colocalizing structures across five orders of magnitude of resolution.

Next, we perform statistical analysis with geometric surrogate graphs to explore the role of spatial embedding in the topological properties of the mouse structural brain network measured with neural tracer imaging and dMRI tractography. We find that spatial embedding plays a considerably larger role in the topology of tractography networks than tracer networks. Tractography underestimates long-range connectivity, which leads to geometric biases in the estimated modular structure and placement of hub nodes. Our results demonstrate the caution required in the interpretation of tractography-derived network measurements that rely on long-range connections and motivate additional geometric consideration in the design of future tractography validation studies.

Finally, we analyze MR spectra from control and dysmyelinated mouse brain with EPSI to reveal limitations in existing biophysical compartmental models traditionally used for myelin imaging. We show that spectra estimated from these biophysical models fail to accurately predict the extent of asymmetric broadening in white-matter voxels, leading ultimately to compromised sensitivity to important differences in white-matter structure.

Throughout, we highlight the value that high-resolution ground-truth imaging brings towards an understanding of the nature of the MR reconstruction problems themselves.

CHAPTER 1

INTRODUCTION

THE mammalian nervous system consists of an incredibly complicated network of biological structures, with functional subsystems shaped and constrained by a structural architecture that operates at scales spanning many orders of spatial magnitude. Individual neurons communicate via nanometer-scale junctions called synapses, while groups of neurons form complex feedback circuits and white-matter tracts that integrate spatially segregated functional regions across centimeter scale distances within the brain.

Our understanding of the architecture of the brain has been mediated through developments in biological imaging since the early microscopy experiments of Santiago Ramón y Cajal[1]. Optical imaging methods have helped uncover the structure of neurons and glial cells in the brain and have guided cell recording studies responsible for countless advances in basic neuroscience. On the macro scale, imaging modalities such as computed tomography, positron emission tomography, and magnetic resonance imaging (MRI) have revolutionized clinical diagnosis and the understanding of a number of neurological disease processes. No single imaging modality, however, is capable of fully characterizing the architecture of the mammalian brain; each is constrained by tradeoffs in achievable resolution, sensitivity, and field of view. At the smallest spatial scale, automated serial electron microscopy (EM) methods can achieve nanometer-level resolutions and produce saturated reconstructions of neurons and glial cells with subcellular detail[2], but only across extremely small volumes: imaging just a single cubic millimeter of brain tissue with an isotropic voxel size of 4 nm would result in nearly 16 petabytes of data[3]. MRI and other clinical modalities are sensitive to microstructural tissue features across volumes as large as entire human brains, but are limited to macroscopic spatial resolutions on the order of millimeters.

Accordingly, a full understanding of the basic structure and function of the mammalian nervous system and its pathologies requires the development of multi-modal imaging pipelines,

where low-resolution modalities can provide important spatial context for information derived from high-resolution modalities, and high-resolution modalities can provide insight into the fundamental microstructural basis of signals from low-resolution modalities.

The theme of this dissertation is the development of tools and analysis methods for performing such multi-modal imaging studies for the validation of MRI microstructural imaging methods in the mouse brain, with specific focus on diffusion MRI (dMRI) reconstructions and tractography methods.

1.1 Diffusion MRI

The Brownian motion of spins measured with nuclear magnetic resonance (NMR) causes a small amount of dephasing that leads to a measurable decrease in signal magnitude. In 1965, Stejskal and Tanner designed a pulsed-gradient spin-echo NMR sequence to map this signal attenuation to a measurement of the apparent diffusion coefficient (ADC)[4]. In his landmark 1973 paper[5] introducing the concept of MRI, Paul Lauterbur speculated on the capacity of the new imaging technique to perform similar *spatial* measurements of water diffusion:

> Variations on the experiment, to be described later, permit the generation of two- or three-dimensional images displaying chemical compositions, *diffusion coefficients* [emphasis added] and other properties of objects measurable by spectroscopic techniques.

The amount of diffusion-caused spin dephasing in an MRI experiment depends on γ, the gyromagnetic ratio of the water proton, the diffusion time t during which the spins diffuse and dephase, and $|\boldsymbol{G}|$, the magnitude of the diffusion gradient vector[6]. These properties are combined into a quantity called the b-value. For a standard Stejskal-Tanner sequence with pulses of duration δ separated by a time interval Δ, the b-value is given by

$$b = \gamma^2 |\boldsymbol{G}|^2 \delta^2 \left(\Delta - \delta/3\right). \tag{1.1}$$

As the b-value increases, either via the use of stronger diffusion gradients or a longer diffusion time, the spins are allowed to dephase more and the signal will become more attenuated, which can be modeled with the following simplistic monoexponential decay relationship:

$$S(b) = S_0 \exp(-bD), \tag{1.2}$$

where $S(b)$ is the signal at b-value b, S_0 is the baseline T2-weighted signal without diffusion sensitization (also referred to as the b_0 image), and D is the ADC[6]. Accordingly, spatial measurements of the ADC can be made by acquiring images with multiple b-values and fitting the data to equation 1.2 to estimate D.

1.1.1 Diffusion tensor imaging

Further development in dMRI came in 1990, when Moseley observed that the diffusion process was anisotropic in white matter[7]: neurons in white matter fiber bundles can be modeled as densely packed cylinders where water molecules are free to diffuse down the long axis but restricted in their abiliity to diffuse in the orthogonal plane by the axonal cell membranes. Accordingly, the ADC measurement in equation 1.2 is dependent on the orientation of the diffusion gradient $\boldsymbol{G}$. To derive gradient-independent measures of ADC, investigators proposed to acquire a baseline S_0 image as well as three diffusion images along orthogonal directions and average the three resulting ADC estimates, a simple approach that remains clinically useful today[6].

Douek et al.[8] recognized that the diffusion anisotropy that complicated ADC estimates offered an opportunity to recover the orientation of white-matter fibers. This work was expanded on by Peter Basser et al. in two seminal papers in 1994[9,10] providing a fully 3D mathematical framework for diffusion tensor imaging (DTI). The diffusion tensor $\boldsymbol{D}$ is simply

a 3×3 symmetric, positive definite matrix, written as

$$\boldsymbol{D} = \begin{pmatrix} D_{xx} & D_{xy} & D_{xz} \\ D_{xy} & D_{yy} & D_{yz} \\ D_{xz} & D_{yz} & D_{zz} \end{pmatrix}, \tag{1.3}$$

which leads to an expansion of the scalar diffusion equation (equation 1.2) to

$$S(\boldsymbol{g}, b) = S_0 \exp\left(-b\boldsymbol{g}^T \boldsymbol{D}\boldsymbol{g}\right), \tag{1.4}$$

where $\boldsymbol{g}$ is a unit vector in the direction of the diffusion gradient $\boldsymbol{G}$. Accordingly, with at least six diffusion-weighted images and one S_0 image, it is possible to estimate the six unknown coefficients of the $\boldsymbol{D}$ at each voxel with a simple linear or nonlinear least-squares reconstruction. The quantity

$$\boldsymbol{g}^T \boldsymbol{D}\boldsymbol{g} = D_{xx}g_x^2 + D_{yy}g_y^2 + D_{zz}g_z^2 + 2D_{xy}g_x g_y + 2D_{xz}g_x g_z + 2D_{yz}g_y g_z \tag{1.5}$$

is just the equation of an ellipsoid in three dimensions. Properties of the DTI ellipsoid at each voxel can be calculated from eigenanalysis of the corresponding diffusion tensor. For example, fractional anisotropy[11] (FA) is a rotationally invariant scalar metric that quantifies the anisotropy of a diffusion tensor from 0–1:

$$\mathrm{FA} = \frac{3}{2}\sqrt{\frac{(\lambda_1 - \lambda_2)^2 + (\lambda_1 - \lambda_3)^2 + (\lambda_2 - \lambda_3)^2}{\lambda_1^2 + \lambda_2^2 + \lambda_3^2}}, \tag{1.6}$$

where λ_1, λ_2, and λ_3 are the three eigenvalues of the diffusion tensor. FA is used clinically as a biomarker for white-matter integrity, since a high FA value corresponds to a highly anisotropic tensor that reflects the presence of highly organized, coherent fiber bundles oriented primarily along a single direction. An example axial slice of a mouse brain FA image is

shown in Figure 1.1a. The principal diffusion direction can also be extracted as the principal eigenvector of the diffusion tensor and indicates the primary orientation of white matter nerve fibers. This orientation is commonly visualized using a directionally encoded color scheme in which red, green, and blue color channels are mapped to orientation components along the left–right, inferior–superior, and anterior–posterior axes, respectively. A sample directionally-encoded color image is shown in Figure 1.1b.

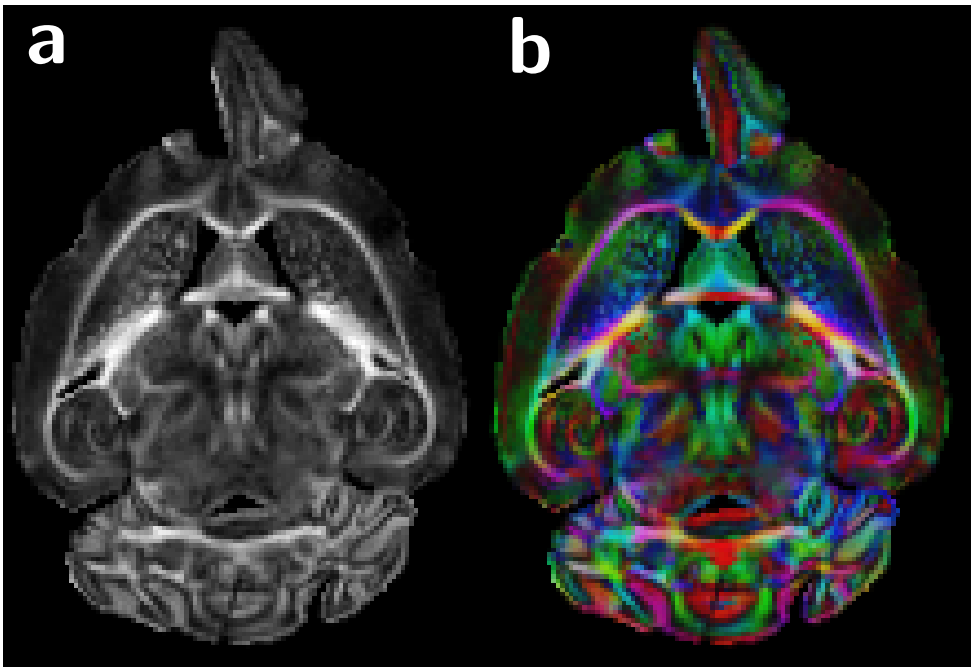

Figure 1.1: Sample FA and directionally-encoded color images. (a) Axial slice of an FA image. Note the gray-white matter contrast. (b) A directionally-encoded color image. Red, green, and blue color channels are mapped to orientation components along the left–right, inferior–superior, and anterior–posterior axes, respectively, and brightness is mapped to FA in order to emphasize white-matter tracts.

1.1.2 High angular resolution diffusion imaging

One limitation of DTI is that it rests on a Gaussian diffusion model assumption[6] and can thus only model a single fiber population at each voxel. In the extremely common condition of a voxel containing multiple crossing or fanning fiber populations, the Gaussian assump-

tion is violated and DTI-derived metrics such as the FA and principal diffusion direction are biased. The attempt to overcome this limitation led to the development of so-called high angular resolution diffusion imaging (HARDI) techniques[6]. HARDI describes a family of acquisition and modeling approaches unified in their goal to use new sampling and reconstruction techniques to recover more high-fidelity estimates of the diffusion process and underlying tissue microstructure.

The true diffusion process at every voxel can be represented by a diffusion propagator function $p(\boldsymbol{r}, t)$, which gives the probability of any displacement $\boldsymbol{r}$ during the diffusion time t. Some HARDI techniques, such as diffusion spectrum imaging[12,13], attempt to directly estimate the diffusion propagator by acquiring a large number of diffusion-weighted images with diffusion gradient orientations and b-values sampling a 3D Cartesian grid. A faster and more clinically relevant approach is to sample multiple diffusion directions along a single "shell" of b-values and instead estimate the orientation distribution function (ODF) Ψ, defined as the radial integral of the diffusion propagator in spherical coordinates[6]:

$$\Psi(\theta, \phi) = \int_0^\infty p(r, \theta, \phi) r^2 \mathrm{d}r, \tag{1.7}$$

where θ and ϕ are the polar and azimuth angles, respectively.

An early approach to recovering the ODF was the model-free q-Ball imaging method developed by Tuch[14,15], which made use of the Funk-Radon transform and a basis of spherical harmonic functions to efficiently map the HARDI signal to an ODF aligned with the underlying fiber population without any a priori knowledge about the number or organization of fiber populations.

A more common current approach is to model the diffusion signal as a spherical convolution[16,17] of the underlying fiber orientation distribution and a "fiber response function" or kernel. In this method, the response function is typically estimated directly from the data using voxels with high FA or within tracts known to be highly homogeneous such as

the corpus callosum. The fiber ODF (fODF) is then estimated using spherical deconvolution techniques. A number of metrics can then be extracted from the fODF to characterize the underlying tissue microstructure, including the number, orientation, and "apparent fiber density"[18] of distinct fiber populations.

1.1.3 Tractography

The estimation of fiber orientations from dMRI measurements allows for the development of fiber tractography pipelines, where local orientation measurements are used to trace the potential trajectories of long-range white-matter pathways[19]. Tractography reconstructions have the potential to estimate an in vivo wiring diagram or "connectome" of the brain[20], and have also been used for neurosurgical planning[21].

Basser et al. used a DTI reconstruction to deterministically trace pathways from the principal diffusion directions of neighboring voxels in vivo[22]. Recent HARDI efforts have focused instead on the development of probabilistic approaches in which fODF reconstructions from HARDI data are treated as spherical probability distributions giving the likelihood of a fiber continuing along any given direction. With these approaches, tractography experiments are performed multiple times to quantify the likelihood of connectivity between two regions[23].

Both deterministic and probabilistic tractography are typically performed with the use of streamlines. Streamlines begin with the selection of a "seed" point. The local orientation information is sampled at the seed point, taken from the principal diffusion direction in the case of deterministic methods, or sampled from the fODF in the case of probabilistic methods. A step with a user-defined length is then taken in the direction of the chosen fiber orientation, at which point a new orientation is sampled. Typically, this process continues until a user-defined stopping criteria is reached. Common heuristic criteria include terminating or discarding a streamline when it exits the brain, reaches an fODF or tensor with a low fiber density or FA, has a curvature exceeding a given threshold, or reaches a

maximum length constraint. Tractography results are also often regularized with additional approaches such choosing anatomically-meaningful initial seed locations[24] and the use of quantitative post-processing techniques to filter spurious streamlines[25,26]. Some pipelines also take a global optimization approach to simultaneously reconstruct the configuration of all fiber pathways that best explain the estimated fiber orientation information rather than propagate individual streamlines[27,28].

A visual demonstration of the entire dMRI tractography pipeline is shown in Figure 1.2. Figure 1.2a shows a representative coronal slice of a mouse brain b_0 image. Figure 1.2b shows a grid of fODFs overlaying the b_0 image constructed using spherical deconvolution. These fODFs were used to generate streamlines with probabilistic tractography, shown in Figure 1.2c. Note the strong fiber density along the known white-matter pathways of the corpus callosum and anterior commissure.

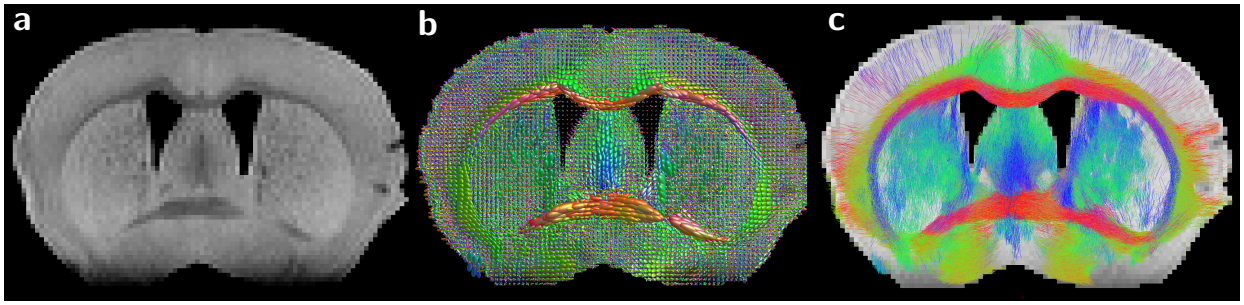

Figure 1.2: The dMRI tractography pipeline. (a) Representative coronal slice of a mouse brain b_0 image. (b) b_0 image with fODFs represented as 3D glyphs. (c) Streamline tractography. visualization. Red, green, and blue color in (b) and (c) represent orientation components along the left–right, inferior–superior, and anterior–posterior axes, respectively.

1.2 Dissertation overview

In all applications of dMRI, the macroscopic signal is used to estimate properties of the local tissue microstructure that are not directly resolvable by the imaging system; axons have diameters on the order of microns[29], whereas clinical dMRI voxels are on the order of millimeters. Likewise, long-range fiber trajectories estimated from tractography streamlines

represent only potential pathways consistent with the underlying diffusion data. Accordingly, new methods for fODF reconstruction, tractography, and connectivity analysis need to be benchmarked with additional high-resolution imaging modalities.

Chapter 2 gives an overview of existing validation techniques and introduces synchrotron x-ray microcomputed tomography (microCT) as a novel validation modality for dMRI. By performing fiber orientation extraction with a computer-vision technique called structure tensor analysis, we demonstrate that whole-brain microCT addresses a number of limitations of existing validation pipelines and will be important for future fODF and tractography validation studies.

Chapter 3 introduces the concept of the "connectome" and the use of graph theory for characterizing brain networks. We then use public neural tracer optical imaging data and a statistical analysis framework using random geometric surrogate graphs to demonstrate geometric bias in current dMRI tractography routines stemming from a dramatic underestimation of connectivity at long distances.

Chapter 4 demonstrates how dMRI itself can be used for validation and characterization of additional MR microstructural imaging techniques. Specifically, we examine biases in popular biophysical models for myelin imaging with spectroscopic MR data and use dMRI to identify white matter voxels and characterize water proton resonance spectra with respect to the presence of crossing fibers and the relative angle between fiber orientations and the main magnetic field.

Finally, we summarize results and offer concluding remarks in Chapter 5.

CHAPTER 2

VALIDATION OF DMRI ORIENTATION DISTRIBUTION FUNCTIONS USING SYNCHROTRON X-RAY MICROCOMPUTED TOMOGRAPHY

2.1 Introduction

2.1.1 Diffusion MRI Validation

DIFFUSION magnetic resonance imaging (dMRI) is an MRI method that seeks to recover microanatomical tissue properties from a macroscopic, spatio-angular profile of the MRI signal attenuation resulting from the restricted diffusion of water molecules[30,31]. Several dMRI acquisition and modeling approaches have been developed to exploit the mapping between tissue microstructure and the resulting diffusion signal in order to estimate various tissue properties, including fiber integrity[32,33], cellular compartmental analysis[34–36], axon diameters[37,38], and long-range fiber trajectories[19]. Metrics derived from dMRI reconstructions have played an important role in the understanding and clinical diagnosis of several neurological disease processes[39] but are limited by the relatively poor spatial resolution of the data. Axons have diameters on the order of microns[29], while typical clinical dMRI voxels are on the order of millimeters for in vivo human acquisitions. This discrepancy in scale introduces uncertainties in the reconstruction of microstructural tissue properties and long-range fiber pathways. Accordingly, dMRI methods require validation with ground-truth imaging across spatial scales capable of resolving micron-level cellular architectures as well as centimeter-level fiber pathways and measures of connectivity across whole brains.

Efforts to validate dMRI reconstructions have primarily relied on optical imaging techniques. For the validation of local fiber orientation and dispersion properties estimated from dMRI, several groups have used histological analysis of tissue sections[40–44], polarized

light imaging[45,46] and optical coherence tomography[47,48]. Various optical imaging methods have also been combined with fluorescent neural tracer injections to validate tractography pipelines in a number of species[49–53].

While optical imaging methods provide sufficient detail to characterize tissue microstructure and specifically delineate white matter pathways, they also come with a number of limitations. The low penetration depth of optical light requires the tissue to be physically sectioned into thin slices. Three-dimensional (3D) representations of the tissue sample are generated either by virtual stacking of natively two-dimensional images of each slice[54] or through deconvolution methods with confocal acquisitions[44,55]. In both cases, the slice thickness is generally several times greater than the best achievable in-plane resolution, leading to anisotropic voxel sizes. Furthermore, the slice cutting and mounting are associated with tissue distortions that make slice alignment difficult[56], preventing the ability to confidently trace small structures such as individual myelinated axons across slice boundaries. These limitations potentially bias the estimation of 3D fiber orientations and complicate the process of spatially registering the ground-truth and dMRI datasets. Optical acquisitions can also be prohibitively labor-intensive to deliver sufficient volumetric data across whole brains, requiring a method of preselecting target regions for imaging. Neural tracer studies are similarly limited to imaging projections to or from a single injection region per specimen, making ground-truth, whole-brain connectivity studies extremely costly.

2.1.2 Synchrotron x-ray microcomputed tomography

In contrast to optical photons, x-rays have high penetration depth in biological tissues, allowing for whole-sample imaging without physical sectioning. While x-rays have poor absorption contrast in biological tissues, advances in metal staining[57,58] protocols allow for the high-contrast imaging of ex vivo samples.

A synchrotron is a form of particle accelerator that can generate an extremely high

photon flux of potentially monochromatic x-rays with a high brilliance and small beam divergence[59]. In the standard detection chain, synchrotron x-rays transmitted by the sample are absorbed by a scintillating material, and the emitted scintillation light is focused onto a charge-coupled device camera[60]. The high photon flux and detector optics allow for rapid acquisitions at histological resolutions. Together with a rotating sample stage, tomographic reconstruction techniques have been used to create volumetric microcomputed tomography (microCT) images of neurological biological samples from mice[61], zebrafish[62], and other samples.

Recent work has shown the ability to acquire micron-level microCT scans of the whole mouse brain and register them with both prior whole-brain dMRI and subsequent region-of-interest electron microscopy (EM) data[63]. In this chapter, we demonstrate that this whole brain MRI–microCT imaging and registration pipeline provides a potential alternative, complementary ground-truth dataset to optical techniques for the validation of dMRI. Synchrotron microCT addresses the limitations of optical imaging by providing isotropic, micron-level spatial resolution across whole mouse brains with no physical sectioning, allowing for future studies validating dMRI methods at the scale of local microstructural features up to long-range white matter pathways.

2.1.3 Author contributions

This chapter was originally published in *Magnetic Resonance in Medicine* under the title "Synchrotron X-ray micro-CT as a validation dataset for diffusion MRI in whole mouse brain."[64] with co-authors Sean Foxley, Narayanan Kasthuri and Patrick La Rivière. The author was responsible for all analysis, figures, and text in the chapter, while the co-authors were responsible for the conception of the imaging pipeline project, the collection of all data, and manuscript review. Figure 2.14 was created by the author for inclusion in an additional manuscript titled "Multi-modal imaging of a single mouse brain over five orders

of magnitude of resolution"[63], published in *NeuroImage* with co-authors Sean Foxley, Vandana Sampathkumar, Vincent De Andrade, Anastasia Sorokina, Katrina Norwood, Patrick La Rivière, and Narayanan Kasthuri. The author performed the multi-modal registration presented in the figure, while the additional authors were responsible for project conception, data acquisition, additional analysis, and manuscript writing.

2.2 Methods

2.2.1 Animal procedures and tissue preparation

All procedures performed on animals followed protocols approved by the Institutional Animal Care and Use Committee and were in compliance with the Animal Welfare Act and the NIH guide for the Care and Use of Laboratory Animals. An eight week-old, female C57BL/6 mouse (26 g) was anesthetized with 60 mg/kg pentobarbital. The animal was then injected with heparin intraperitoneally and sacrificed by intercardial perfusion with 0.01 M phosphate buffer saline solution. This was immediately followed by 4% paraformaldehyde (pH 7.4)/PBS fixative solution. The brain was extracted from the skull and post-fixed in the same fixative overnight at 4°C and washed in PBS for 74 hours to remove fixative before imaging.

2.2.2 MRI acquisition and analysis

Prior to MRI experiments, the brain was submerged in Fluorinert (FC-3283, 3M Electronics) to improve shimming and mitigate susceptibility-mismatch artifacts. Data were acquired at 9.4 Tesla (20 cm internal diameter, horizontal bore, Bruker BioSpec Small Animal MR System, Bruker Biospin, Billerica, MA) using a 6 cm performance gradient insert (maximum gradient strength: 1000 mT/m, Bruker Biospin) and a 35 mm internal diameter quadrature volume coil (Rapid MR International, Columbus, Ohio). Diffusion data were acquired with a conventional 3D spin-echo/Stejskal-Tanner diffusion-weighted sequence at 150 μm isotropic

resolution across 30 diffusion-encoding directions at a b-value of 3000 s/mm^2 (TR=400 ms, TE=18.5 ms, δ=5 ms, Δ=11.04 ms, receiver bandwidth=200 kHz, partial Fourier along first phase encoding direction=7/8, number of b_0s = 10, duration=55 h 19 min 40 sec).

For anatomical reference, a water peak-height image was constructed from 3D echo-planar spectroscopic imaging (EPSI) data of the same sample. This technique has been shown to be a high fidelity T2*-weighted source of image contrast[65] and is particularly sensitive to local susceptibility changes associated with the presence of myelin in white matter[66]. Data were acquired at 50 µm isotropic resolution using a multi-gradient echo sequence with an oscillating readout gradient train. Sequence parameters were chosen so that the entire voxel-wise free induction decay was sampled to the noise floor with sufficiently high temporal resolution (TR=1000 ms, TE of first echo=3.41 ms, echo spacing=3.41 ms, number of echoes=128, receiver bandwidth=100 kHz, flip angle=84.3°, 50 µm isotropic resolution, 4 averages, and duration=21 h 23 min 44 s). Image contrast in the water peak-height image was produced by taking the maximum voxel-wise signal amplitude of the water spectrum.

A number of preprocessing steps were performed on the diffusion data before further analysis. The raw data were denoised using the `dwidenoise` protocol in the MRTrix3 software package[67–69]. The diffusion data and associated b-vectors were then rotated until they were aligned with the neurological display convention. Brain segmentation was performed on the 10 averaged b_0 volumes, using a thresholding routine implemented in the Dipy package[70]. The resulting brain mask was inspected in ImageJ[71] to manually remove any segmentation errors.

Fiber orientation distribution functions (fODFs) were calculated from the data within the brain mask using constrained spherical deconvolution[16,17]. The response function was estimated directly from the data using the `tournier` algorithm[72] implemented in MRTrix3. Fitting was then performed with the Dipy package for further analysis in Python, with λ=3 and $\tau = 0.1$, up to a maximum spherical harmonic order of $\ell_{\max} = 4$. The data were also fit

to a weighted least-squares tensor model[10] in Dipy in order to calculate the scalar fractional anisotropy (FA) metric[30].

2.2.3 Synchrotron x-ray microCT acquisition

The sample preparation and data acquisition protocol used for microCT imaging has been published in an additional study[63] and is summarized here for completeness. Following dMRI acquisition, the brain was stained using the brain-wide reduced-osmium staining pyrogallol-mediated amplification protocol[57,58]. This protocol is widely used for EM imaging of large biological samples and its utility for improving contrast in microCT has been demonstrated[61]. MicroCT data were acquired at the sector 32-ID beamline of the Advanced Photon Source at Argonne National Laboratory with a central x-ray beam energy of 25.5 keV. Raw projection data had a field of view of 2.25×1.41 mm^2. A 6×18 grid of such acquisitions was collected to cover a total field of view sufficient to image the whole brain rotated around its rostral-caudal axis. This process was repeated across 3600 rotation angles. The projections were digitally aligned and stitched together using a mosaic tomography technique[73] and reconstructed into a single volume with an isotropic voxel size of 1.17 μm using the open-source TomoPy package[74], developed at the Advanced Photon Source.

A representative sagittal slice of the microCT data is shown in Figure 2.1. Insets in the figure highlight the visibility of individual myelinated axons and neuronal soma in the brainstem. The full microCT data can be viewed online through Neuroglancer at the following link: http://tinyurl.com/cxmbjy6b.

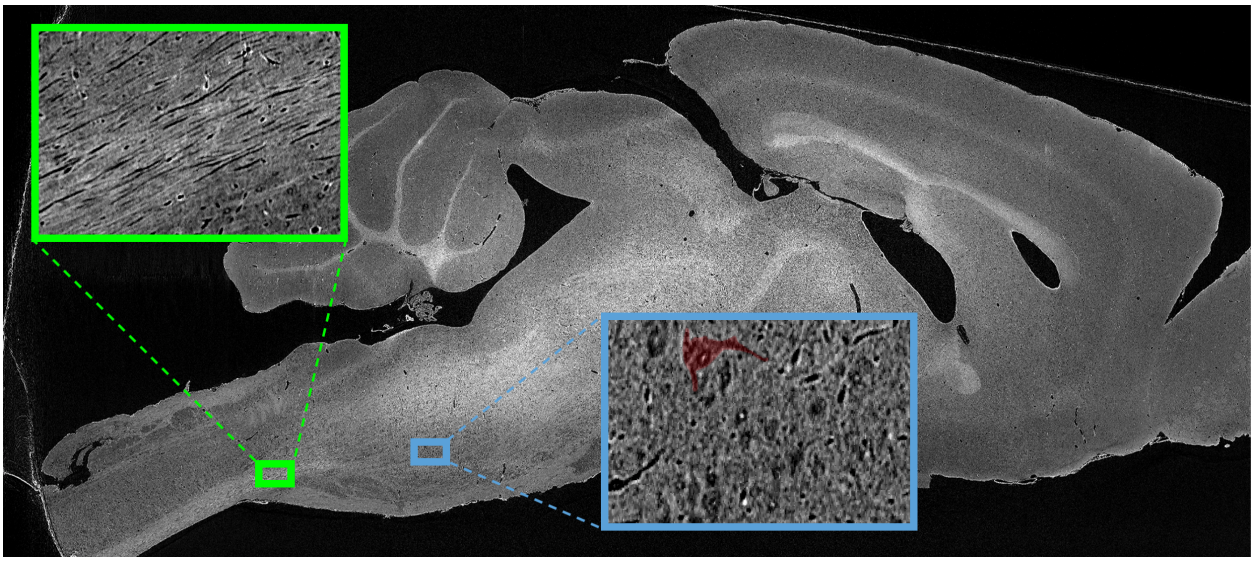

Figure 2.1: A representative sagittal slice of whole-brain microCT data. Insets show individual myelinated axons (left/green) and neuronal somas (right/blue, cell manually highlighted) in the brainstem.

2.2.4 Calculation of microCT fODFs

Voxel-wise fiber orientations were estimated throughout the microCT data using an image processing technique called structure tensor analysis[75] that has been used in previous histological validation studies[40–44]. The structure tensor $\mathrm{ST}(f;\sigma_N)(\boldsymbol{r})$ of image f at each position $\boldsymbol{r}$ is constructed by taking the outer product of the image intensity gradient vector Δf with itself, followed by averaging over a local neighborhood using a 3D gaussian filter g_{σ_N} of width σ_N:

$$\mathrm{ST}(f;\sigma_N)(\boldsymbol{r}) = \left(\nabla f \nabla f^T\right) \circledast g_{\sigma_N} = \begin{bmatrix} f_x^2 & f_x f_y & f_x f_z \\ f_x f_y & f_y^2 & f_y f_z \\ f_x f_z & f_y f_z & f_z^2 \end{bmatrix} \circledast g_{\sigma_N}, \tag{2.1}$$

where $\circledast$ denotes a convolution. More information on implementation details and parameter selection is available in section 2.5. The result is a symmetric, 3×3, semi-positive definite

tensor at each voxel. The eigenvector of the tensor corresponding to the smallest eigenvalue indicates the direction of smallest intensity variation in the local neighborhood. For voxels representing nerve fibers, we make the assumption that this eigenvector is parallel to the local fiber orientation. Confidence in the orientation estimate can be represented by a scalar fractional anisotropy metric constructed from the eigenvalues of the tensor:

$$\mathrm{FA} = \sqrt{\frac{1}{2}\frac{(\lambda_1-\lambda_2)^2+(\lambda_1-\lambda_3)^2+(\lambda_2-\lambda_3)^2}{\lambda_1^2+\lambda_2^2+\lambda_3^2}}, \tag{2.2}$$

where λ_1, λ_2, and λ_3 represent the first, second, and third eigenvalues of the structure tensor at each voxel. This metric is bounded from 0 to 1, where a higher value represents more confidence in the orientation estimate.

The voxel-wise orientation estimates were used to directly construct fODFs within larger regions of interest (ROIs) across the whole brain. First, the data were divided into cubic ROIs matching the size of the corresponding dMRI voxels (150 μm). Of the $N \approx 2\times10^6$ total microCT voxels in each dMRI-voxel-sized region, N' voxels containing fibers were identified by thresholding the raw grayscale values to discard voxels representing microvasculature, as well as by thresholding the FA metric to discard voxels with low orientation confidence. Within each region, the fODF, ψ, can be directly expressed as the sum of N' fiber orientations represented as Dirac delta functions in spherical coordinates[76,77],

$$\psi(\theta,\phi) = \frac{1}{N}\sum_{j=1}^{N'}\delta(\cos\theta-\cos\theta_j)\delta(\phi-\phi_j), \tag{2.3}$$

where $\theta \in [0,\pi]$ and $\phi \in [0,2\pi]$ are the polar and azimuth angles, respectively, and j indexes the N' fiber orientations.

ψ represents a band-unlimited distribution of voxel-wise fiber orientations in a specified region of microCT data. It is convenient to expand ψ onto a finite (i.e., band-limited) number of spherical harmonic functions for computational ease and direct comparison with dMRI-

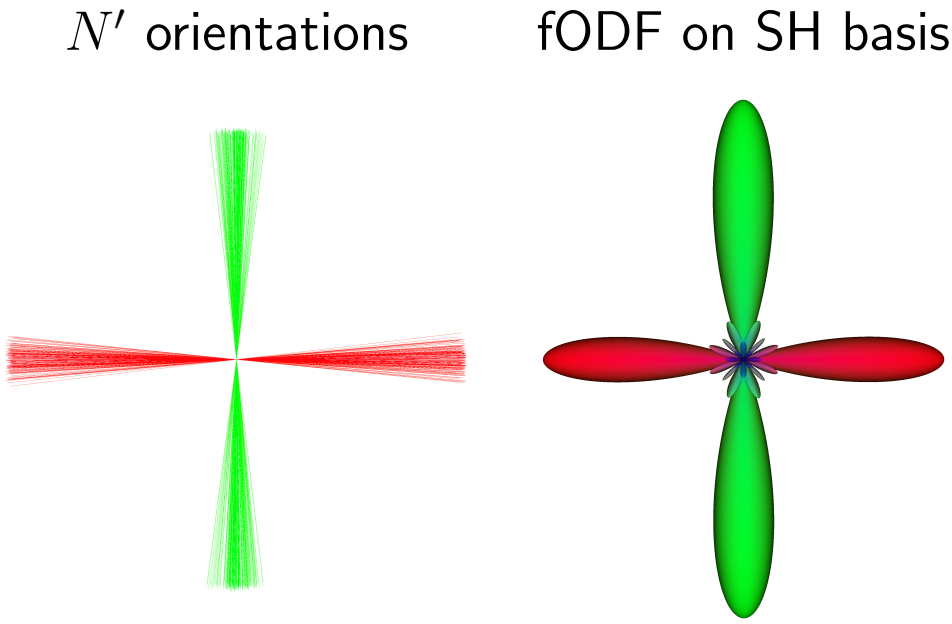

Figure 2.2: Demonstration of the expansion of simulated orientations onto SH functions. (Left) Structure tensor analysis within each dMRI-voxel-sized region results in a list of N' fiber orientations. (Right) These fiber orientations can be used to create an fODF by expansion onto a basis of real, even spherical harmonic functions. In this demonstration, the individual orientations cluster around two distinct fiber populations, with 60% of the orientations belonging to the up–down population (green) and 40% of the orientations belonging to the left–right population (red). The population differences are visualized by the density of unit-length "sticks" on the left, and the height of the lobes on the right.

derived fODF representations. It can be shown[78] that the spherical harmonic coefficients, Ψ_ℓ^m, of a sum of N' discrete orientations are given by

$$\Psi_\ell^m = \frac{1}{N} \sum_{j=1}^{N'} \bar{Y}_\ell^m(\theta_j, \phi_j), \tag{2.4}$$

where Y_ℓ^m is the spherical harmonic function of degree ℓ and order m and the overbar denotes a complex conjugate. As with dMRI, we assume that these fODFs have even symmetry, so coefficients were calculated for even harmonic degrees. For this study, we chose to expand the fODF to $\ell_{\max} = 8$, in accordance with recommendations for the highest $\ell_{\max}$ typically used in dMRI studies[72]. A visual demonstration of the expansion of simulated orientations

onto spherical harmonic functions is shown in Figure 2.2, and a demonstration of the entire structure tensor analysis pipeline is shown on an ROI of microCT data from a mouse hippocampus in Figure 2.3.

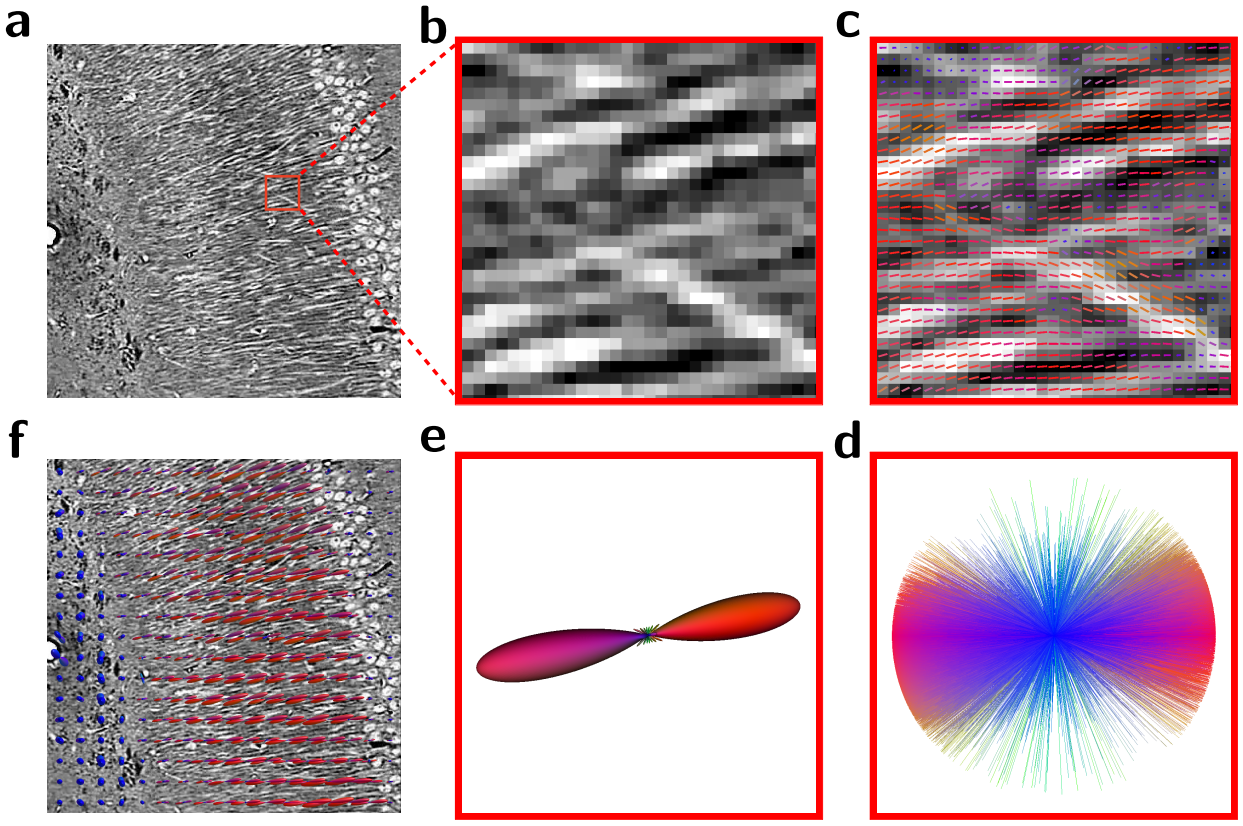

Figure 2.3: Demonstration of the entire structure tensor analysis pipeline on real microCT data. (a) Intensity data displaying oriented dendritic fibers in the hippocampus. (b) Zoom-in display of a dMRI-voxel-sized region. (c) Orientation vectors over each voxel showing the 3D direction of the lowest intensity change within a local neighborhood. Orientation is encoded by vector direction as well as vector color: here red is left–right, green is up–down, and blue is in–out of the page. (d) Orientation vectors from the entire ROI in (c) expressed as a spherical histogram ($\psi(\theta, \phi)$ in equation 2.3). (e) The fODF from (d) expressed in terms of even spherical harmonic functions (Ψ_ℓ^m in equation 2.4). (f) The full ROI from (a) with fODFs calculated at dMRI resolution.

2.2.5 Spatial registration

Compared to optical techniques, spatial registration of the microCT and dMRI datasets was simplified by the fact that unsectioned, volumetric, ground-truth data and fODFs were avail-

able across the whole brain, meaning that existing whole-brain dMRI registration routines could be applied directly. An overview of the registration pipeline is shown in Figure 2.4.

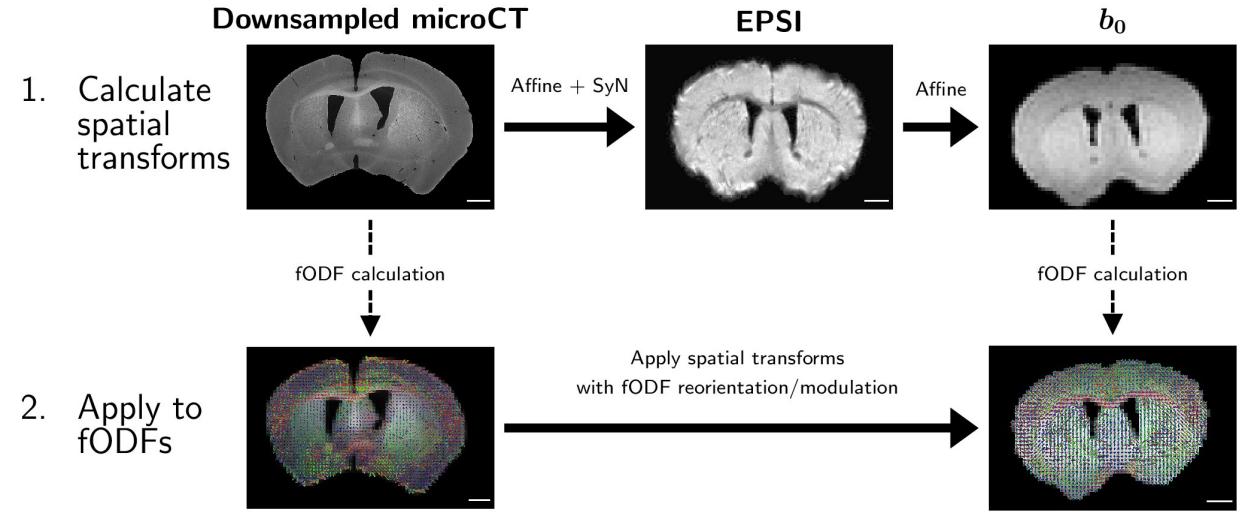

Figure 2.4: Multi-modal spatial registration pipeline. Downsampled microCT data were registered to EPSI peak-height data using affine and symmetric diffeomorphic (SyN) transforms. EPSI data were registered to the b_0 template using affine transforms. The concatenated transforms were then applied to the microCT fODFs calculated at dMRI resolution. Scale bars are 1 mm.

The strategy was to calculate the spatial transformation from microCT space to dMRI space by leveraging the higher anatomical detail of the EPSI peak-height image, then to apply this transformation to the structure tensor-derived microCT fODFs. First, the ten b_0 images of the dMRI dataset were averaged to form an anatomical template in dMRI space. The EPSI peak-height image was registered to the b_0 template using an affine transformation calculated with the ANTS registration package[79,80]. The microCT data were directly downsampled to dMRI resolution using the same binning ROIs used for fODF construction. Downsampled microCT data were then registered to the EPSI peak-height image using affine and symmetric diffeomorphic transformations calculated using the SyN algorithm[81] in ANTs. The concatenated transforms from microCT to EPSI to b_0 were then applied to the microCT fODFs using the `mrtransform` command in MRtrix3, which reorients[82] and modulates[18] of the fODFs to preserve the apparent fiber densities across fiber bundles before and after the

transformation. All spatial registrations were calculated using a five-level, multi-resolution scheme with mutual information as the similarity metric and a convergence value of 10^{-7}.

2.2.6 Multi-modal fODF comparisons

Several scalar metrics were used to analyze agreement in the fiber orientation representations from dMRI and microCT. The `peaks_from_model` peak-finding routine in Dipy was performed to identify the orientations and magnitudes of distinct fiber populations in every fODF from both modalities. In this algorithm, the fODFs were mapped from a spherical harmonic basis to a dense basis of 7500 discrete points on the sphere. Peak candidates were defined as points on the discrete-basis fODF that are greater than at least one neighbor or equal to all neighbors. A number of thresholding heuristics used commonly in the literature[44,83] were then implemented to determine the final peaks. To avoid the inclusion of spurious peaks introduced by noise, peaks were discarded if their magnitudes were smaller than 20% of the largest fODF value found for each modality. Peaks were also discarded if they fell within 20° of a larger peak. The angular distance between corresponding primary peaks from both modalities was calculated to assess agreement in the identification of fiber population orientations.

The angular correlation coefficient (ACC)[84] between the fODF SH coefficients from each modality was also calculated to assess agreement in their overall shape.

The angular distance between peaks and ACC across all voxels were further categorized by tissue type. Tissue masks for white matter, gray matter, and cerebrospinal fluid were generated through voxel-wise classification of the EPSI peak-height data using the Atropos[85] algorithm in ANTs. Finally, the comparison metrics were evaluated as a function of the dMRI tensor-derived FA metric to assess fODF agreement as a function of fiber coherence.

2.2.7 Tractography

While voxel-wise comparisons of individual fODFs demonstrate the potential use of microCT for validation of local dMRI metrics, a final study was conducted to demonstrate the utility of microCT for multi-modality, long-range connectivity studies. Tractography was performed with both the dMRI and microCT fODFs using the probabilistic iFOD2 algorithm[86] in MRTrix3 to map and segment two fiber pathways of interest: the anterior commissure tract and the corticospinal tract. Delineation of the fiber tracts was achieved with the manual placement of three ROIs within the pathway of each tract. Since both tracts of interest display a similar posterior–anterior branching pattern, one ROI was placed near the central, posterior terminal and the remaining two were placed on the left and right anterior branches of each tract. The ROIs were used as inclusion gates for tractography, such that accepted streamlines had to pass through both the posterior gate and at least one of the anterior gates in order to be accepted. The step size was set to 37.5 μm (0.25 × voxel size) and the maximum angle between successive steps was set to 35°. The number of streamlines was selected separately for each tract in order to ensure adequate coverage of the pathway volume, with 300 for the anterior commissure tract and 6000 for the corticospinal tract. Finally, tract segmentations were further refined and spurious streamlines were removed using additional manual ROIs that functioned as exclusion gates.

Whole-brain deterministic tractography was also performed with the SD_STREAM algorithm[67] in MRTrix3 using registered fODFs for each dataset to demonstrate the utility of microCT for long-range connectivity studies. A total of 200,000 streamlines were generated from each modality, with a step size of 37.5 μm (1/4 of a dMRI voxel) and a maximum angle between successive steps of 35°.

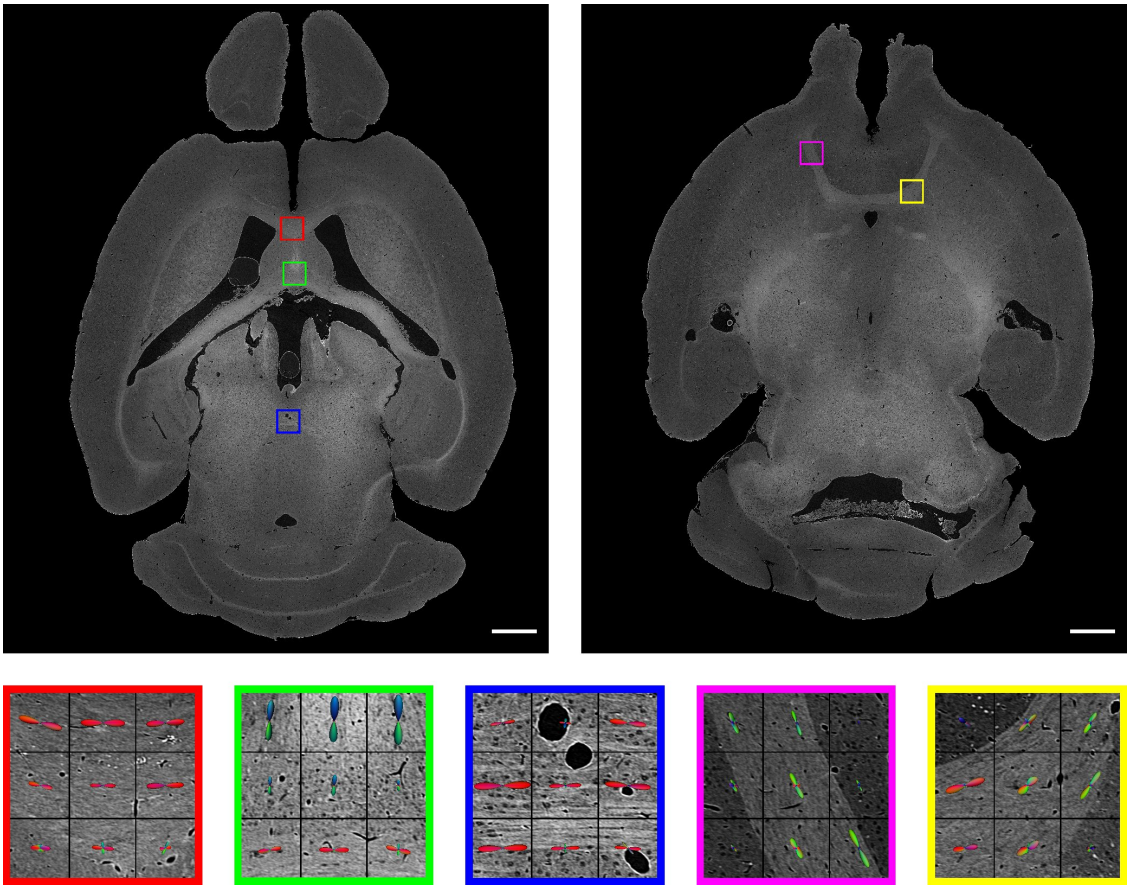

Figure 2.5: Visualization of microCT data and fODFs across two axial slices. Structure tensor-derived fODFs are visualized as 3D glyphs overlaying ROIs of raw microCT data. Each fODF was calculated from microCT data contained in a 150 μm^3 volume indicated by the black lines. RGB color in the fODFs represents orientation, with red encoding left–right, green encoding anterior–posterior, and blue encoding the superior–inferior direction. Color borders around the ROIs indicate the position of each inset within the whole slices. Scale bars are 1 mm.

2.3 Results

2.3.1 MicroCT fODFs

Structure tensor analysis was used to calculate a total of n=151,094 fODFs from the microCT data, covering the whole brain at an isotropic resolution of 150 µm. Background regions were avoided by directly downsampling the microCT data to the target isotropic

voxel size of 150 μm and generating a brain mask using segmentation routines in Dipy. Full computation of the voxel-wise fiber orientations and expansion onto spherical harmonic coefficients required a total of around 120 hours using 128 cores of a local computing cluster.

Figure 2.5 shows representative, full-resolution axial slices of the microCT data, with insets displaying structure tensor-derived fODFs visualized as 3D glyphs. Each square in the 3×3 grid within the inset images represents a cube of microCT data the size of a single dMRI voxel. The fODFs agree qualitatively very well with the fiber orientations observed in the microCT data, closely following the arc in the curved region of the anterior commissure (yellow) and corpus callosum (red), capturing the parallel fibers of the posterior (blue) and anterior (pink) commissures, and capturing the change in fiber orientation at the intersection of the lateral septal complex of the striatum with the fornix system (green).

Because each fODF was generated from N' separate orientation estimates but normalized by $N \approx 2 \times 10^6$, where $N' < N$ (Eq. 2.4), the relative size of the fODFs reflects the fraction of microCT voxels within each ROI that were identified as representing valid fibers. This is clearly seen along the limb of the anterior commissure (Figure 2.5, pink): the fODFs calculated within fiber-dense, in-tract ROIs are much larger than those outside the main tract. The fraction of identified fiber voxels can be considered a proxy for the fiber density (FD) within each ROI, and can be calculated directly from the c_{00} coefficient of the SH representation of the fODFs:

$$\mathrm{FD} = \frac{N'}{N} = \frac{c_{00}}{Y_0^0}, \tag{2.5}$$

where $Y_0^0 = \sqrt{1/4\pi}$ is the constant $\ell = 0$ SH function. Representative slices from a map of FD values are shown in Figure 2.6a–c. The FD metric shows good contrast between gray and white matter, indicating that the structure-tensor pipeline was successful in correctly identifying white matter fibers. Full-resolution data corresponding to ROIs calculated as having high, medium, and low values of FD are shown in Figures 2.6d–f . Notably, Figure 2.6f

contains an example of a partial volume effect, where a small region with high fiber density (lower right) is present with a larger region with low fiber density (upper left), resulting in an overall low FD value.

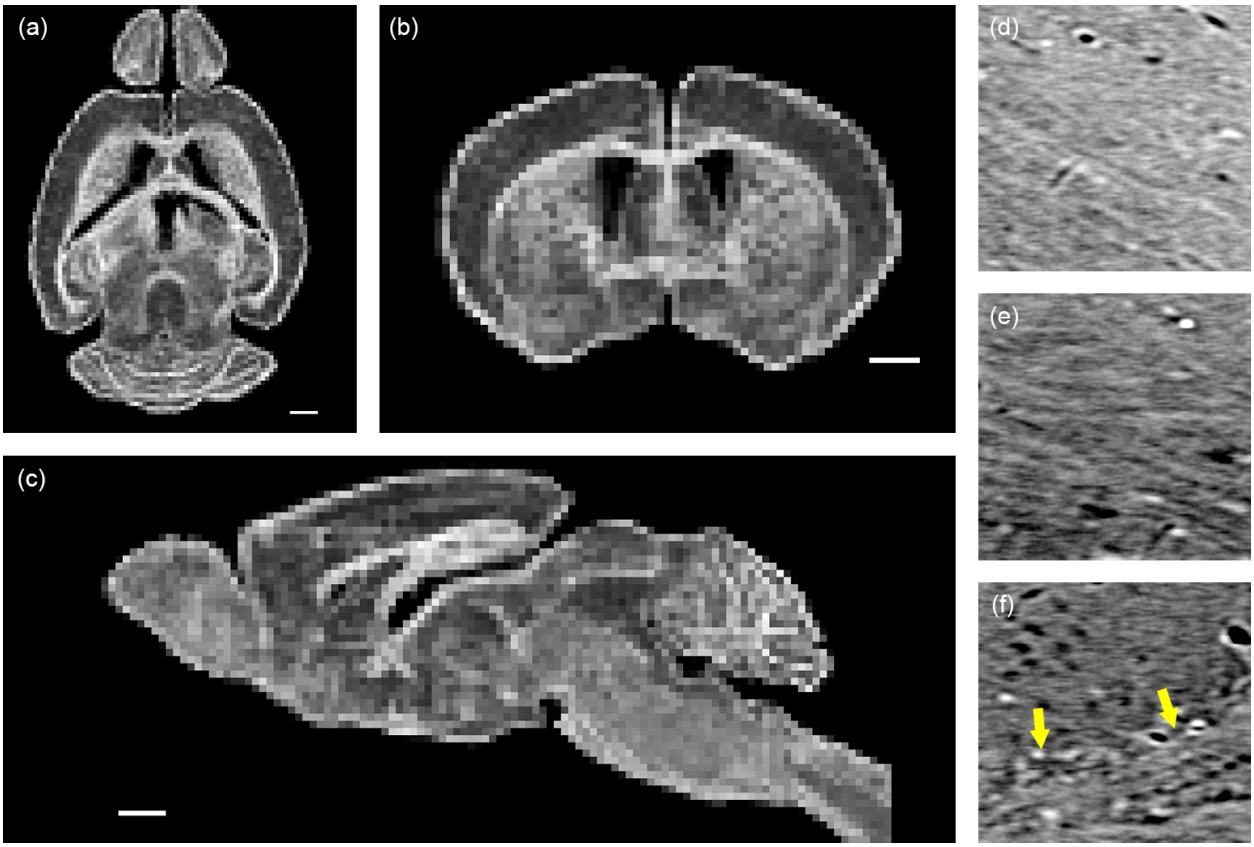

Figure 2.6: Fiber density measure derived from microCT fODFS. (a-c) Representative FD slices showing contrast between gray and white matter. Scale bars are 1 mm. (d-f) Examples of microCT data from 150 μm^3 cubic regions calculated as having (d) high (FD = 0.41), (e) medium (FD = 0.32), and (f) low (FD = 0.20) fiber density. Arrows in (f) indicate an example of a partial volume effect, where a small region with high fiber density (lower right) is present with a larger region with low fiber density (upper left), resulting in an overall low FD value.

2.3.2 Spatial correspondence of fODFs

An example of registered and reoriented microCT fODFs is shown across a representative axial slice of downsampled microCT data in Figure 2.7 alongside the corresponding dMRI fODFs. Individual fODFs have been normalized for clear visualization. Overall, the two

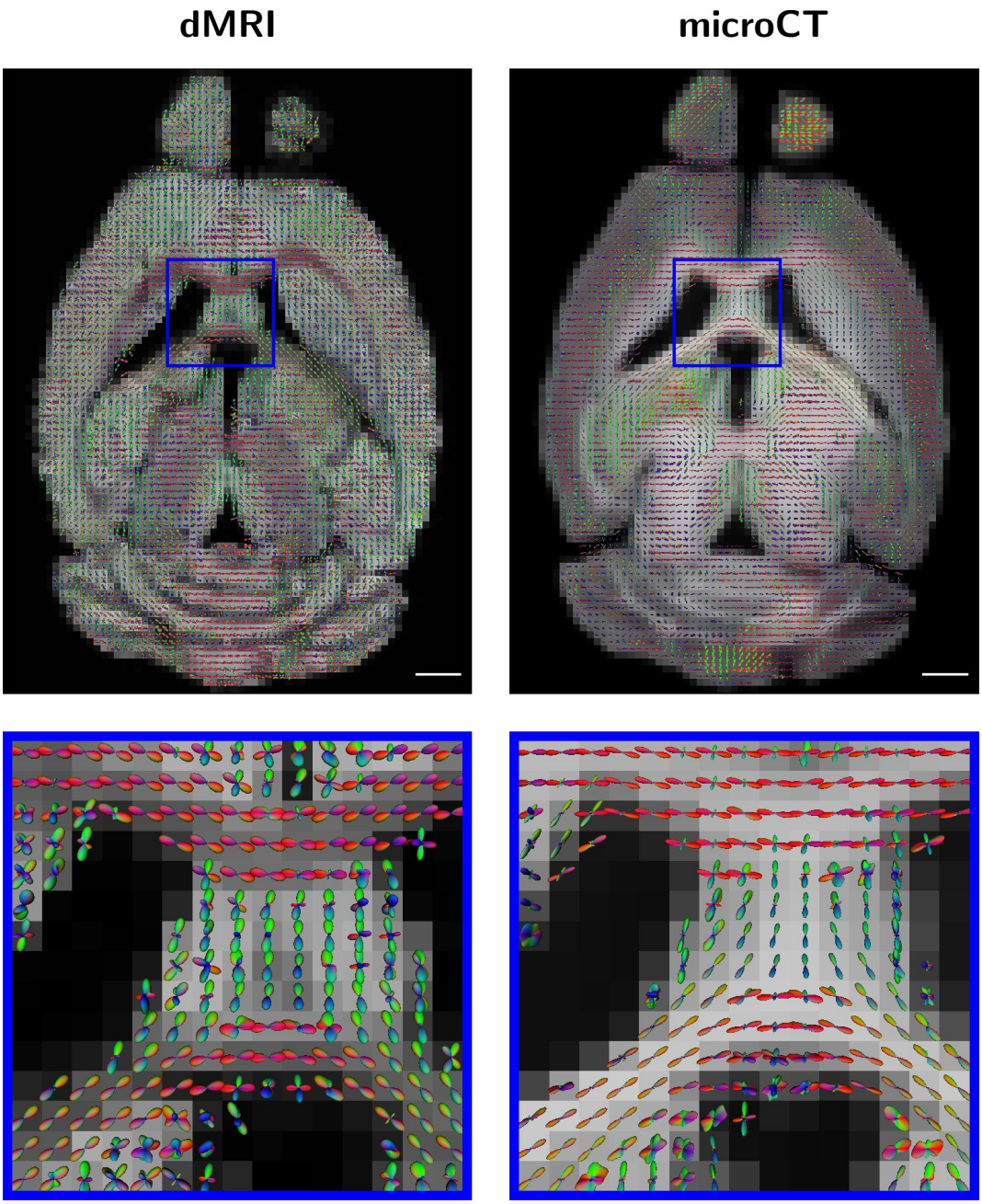

Figure 2.7: Multi-modal spatial registration results. fODFs from both modalities are represented as 3D glyphs overlaying EPSI peak-height data and downsampled microCT data, both spatially aligned to the b_0 of the dMRI dataset. The inset shows the correspondence in fODF shapes along visible fiber tracts. fODFs have been normalized to a maximum value of 1 for visualization. Note that the sharpness of the angular profile of the fODFs differs between the two modalities, resulting from the fact that they have different angular bandlimits ($\ell_{\max} = 4$ and $\ell_{\max} = 8$ for dMRI and microCT, respectively). Scale bars are 1 mm.

modalities show good qualitative correspondence in anatomical structures and fODF shapes, particularly along the coherent fiber pathways shown in the inset. Note that the sharpness of the angular profile of the fODFs differs between the two modalities, resulting from the fact that they have different angular bandlimits ($\ell_{\max} = 4$ and $\ell_{\max} = 8$ for dMRI and microCT, respectively).

Validation of local microstructure

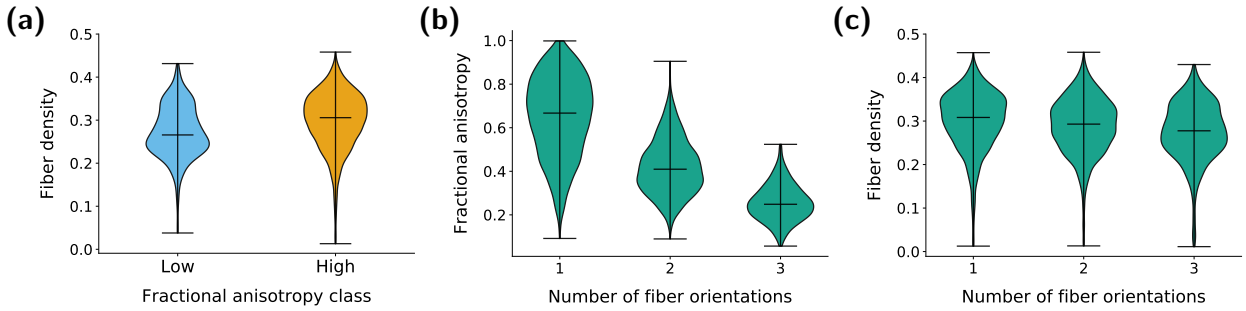

Figure 2.8: Comparison of microCT-derived FD and dMRI-derived FA metrics. (a) Violin plots showing the distribution of FD values for the low (<25th percentile) and high (>75th percentile) FA classes. (b) Violin plots showing the distributions of FA values for increasing number of distinct fiber populations as identified with the peak-finding algorithm. (c) Violin plots showing the distributions of FD values for increasing number of distinct fiber populations. As expected, FA values tend to decrease for higher number of fiber populations, while the FD values stay relatively constant.

The relationship between the dMRI-derived FA metric and the microCT-derived FD metric was analyzed to demonstrate the utility of microCT for use in the validation of dMRI-derived microstructural features. White-matter voxels were grouped into classes of "low-FA" (<25th percentile) and "high-FA" (>75th percentile). Figure 2.8a shows that there is good separation between the distribution of FD values in these two groups, indicating loose correlation between the two metrics and suggesting that FA is successfully reporting some measure of fiber density, as expected. However, it is known that FA values are heavily biased in the presence of multiple, non-parallel fiber populations. This effect is demonstrated in the data: the distribution of FA values decreases with an increasing number of distinct fiber

populations (Figure 2.8b), while the fiber density derived from microCT remains more stable (Figure 2.8c), indicating that the drop in FA for voxels with multiple fiber populations is a result of modeling bias rather than a reflection of true change in the density or organization of fiber populations in these voxels.

Validation of fODF shape

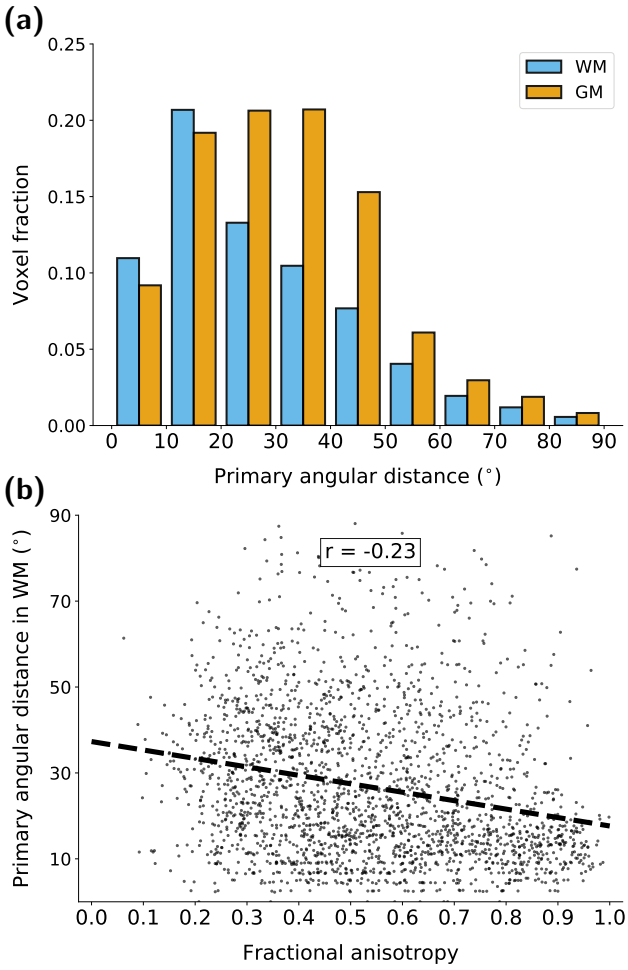

Figure 2.9: Identification of primary fiber orientations. (a) Histogram of angular distance between primary fiber orientations from microCT and dMRI fODFs, grouped by tissue class. (b) Scatter plot of angular distance of primary fiber orientations in white matter vs. fractional anisotropy.

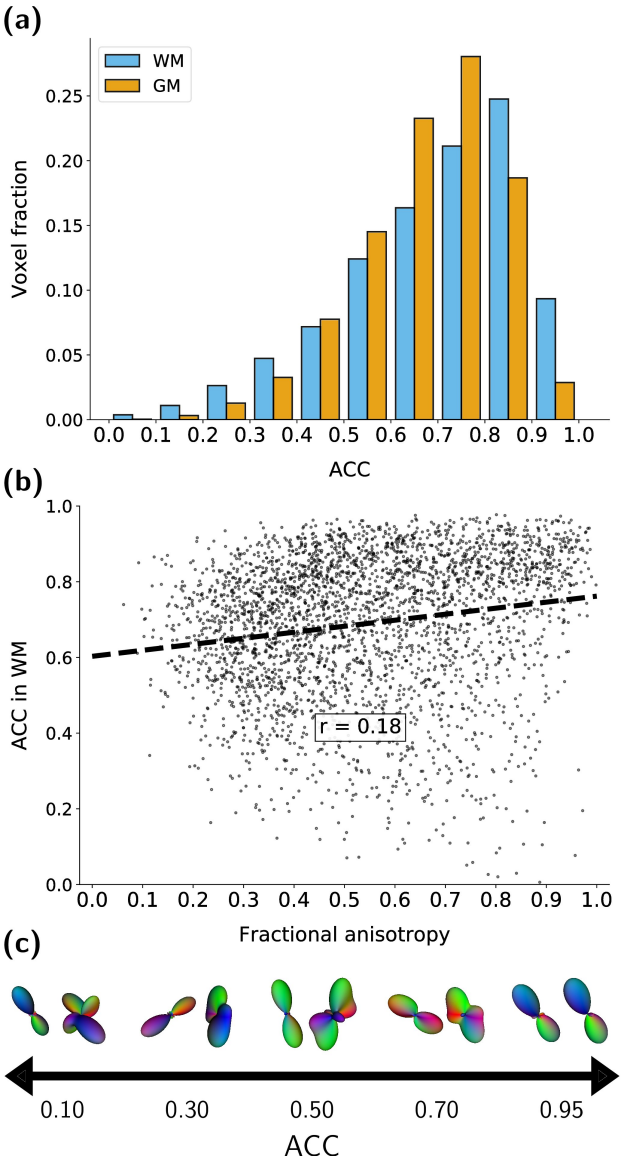

Figure 2.10: Angular correlation coefficient of cross-modality fODFs. (a) Histogram of ACC between microCT and dMRI fODFs, grouped by tissue class. (b) Scatter plot of white-matter ACC values vs. fractional anisotropy. (c) Visualization of sample fODF pairs with increasing ACC values for reference.

The multi-modal correspondence between fODF shapes was assessed quantitatively through measurement of the angular distance between primary fiber orientations and the ACC of corresponding SH coefficients. The angular distances in primary fiber orientations between the two modalities are shown categorized by tissue type in Figure 2.9a. White matter fODFS had a lower mean angular error (peaking in the 10°–20° bin) than gray matter

fODFs (peaking in the 30°–40° bin). Primary angular distance is shown plotted against FA for white matter voxels in Figure 2.9b. A weak linear relationship is shown (r= −0.23), indicating that the modalities show stronger agreement in the orientation of the primary fiber orientation for voxels with a high degree of fiber coherence.

The ACC metric evaluates the overall agreement in shape between two fODFs. Distributions of ACC values are shown in Figure 2.10a, grouped by tissue type, with white matter fODFs having a higher mean ACC (peaking in the 0.8–0.9 bin) than gray matter fODFs (peaking in the 0.7–0.8 bin). ACC also shows a weak linear relationship (r= 0.18) with FA in white matter voxels (Figure 2.10b), indicating that the modalities show more similar representations of the fODFs in voxels with single, coherent fiber orientations. Representative pairs of fODFs with different ACC values are demonstrated in Figure 2.10c.

Tractography

Probabilistic tractography was used to segment two major white matter tracts in both datasets in order to further demonstrate the correspondence in fiber orientation information between modalities and to show the potential for the use of microCT in long-range connectivity studies. Figure 2.11 shows tractography results for the anterior commissure and corticospinal tracts, generated using fODFs from both modalities. Overall, tracts from the two modalities show good visual agreement with each other and with the known trajectories of these fiber pathways. The Spearman rank correlation coefficient between the FD metric and the streamline count density for voxels containing at least one streamline was 0.18 and 0.19 for the dMRI and microCT anterior commisure tracts, respectively, and 0.20 and 0.23 for the dMRI and microCT corticospinal tracts, respectively, indicating a comparable relationship between streamline count and fiber density in these tract segmentations for both modalities.

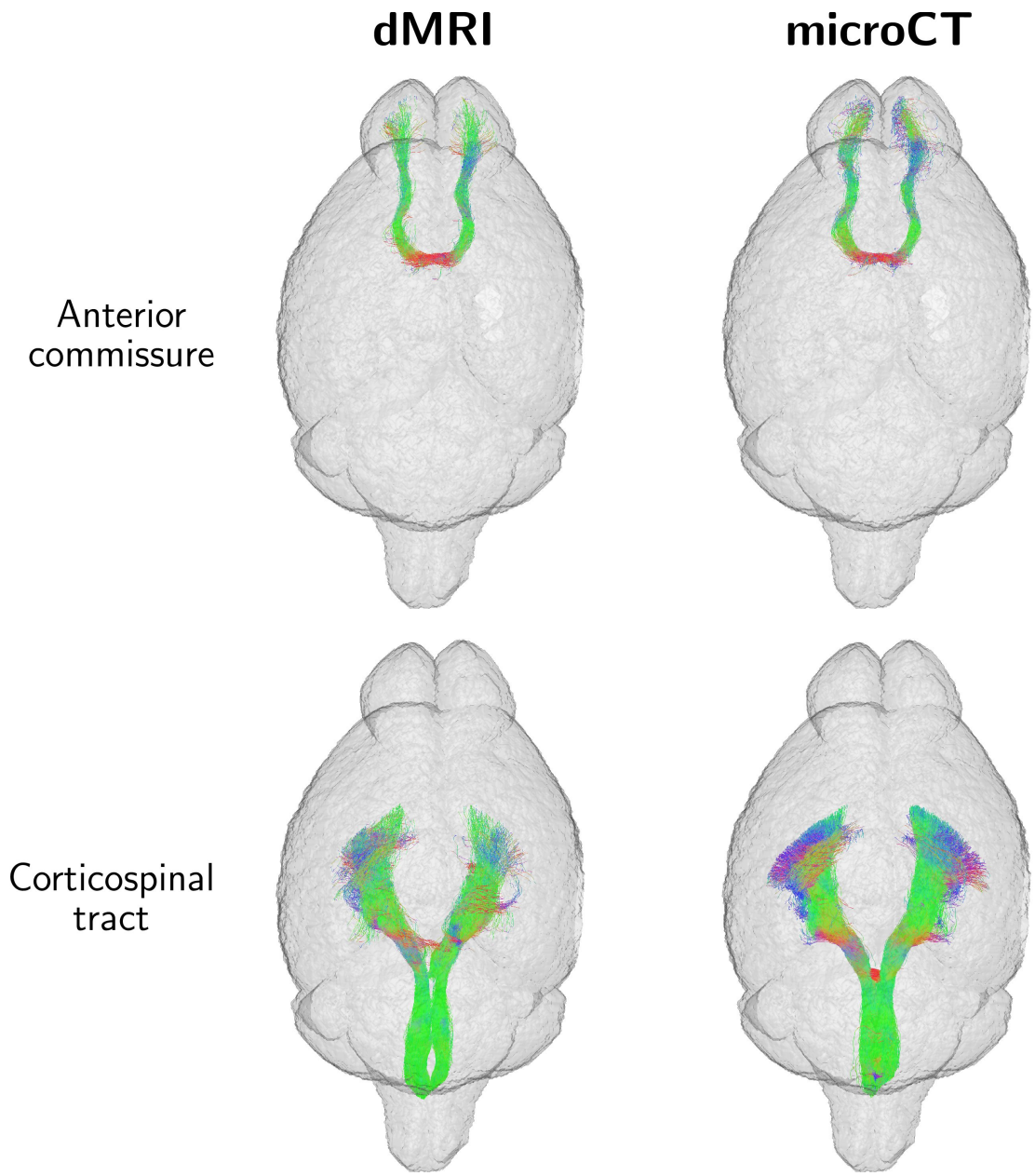

Figure 2.11: Tractography results. Both modalities were able to recover the general shape and orientation of the anterior commissure and corticospinal tracts.

Deterministic tractography was also used to map long-range white matter pathways across both datasets. Whole-brain tractography results are shown in Figure 2.12. Overall, tracts from the two modalities show good visual agreement in the mapping of major tracts, indicating the success of dMRI tractography algorithms on structure tensor-derived

fODFs, further demonstrating the multi-modal correspondence in fiber orientation information and motivating the use of microCT in future connectivity and tractography validation studies.

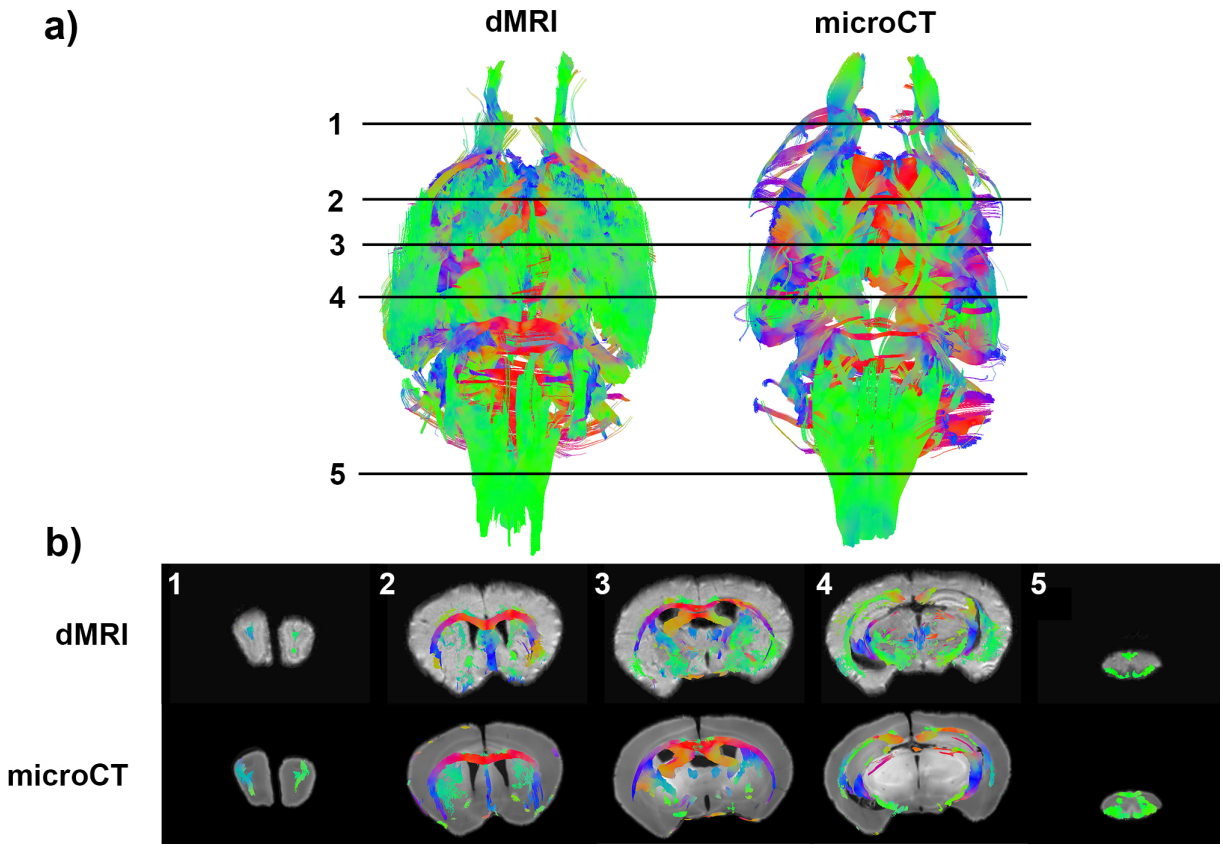

Figure 2.12: Deterministic tractography results, visualized as streamlines (a) across the whole brain and (b) overlaying five coronal slices of registered dMRI and microCT data, on the top and bottom rows, respectively. Slice numbers in (b) correspond to numbered lines crossing whole-brain results in (a)

2.4 Discussion

Full characterization of the strengths and weaknesses of various dMRI methods will require the application of several complementary ground-truth imaging approaches. This study set out to introduce and qualitatively probe the capabilities of whole-brain synchrotron x-ray microCT as a new approach that specifically addresses some limitations in optical-based

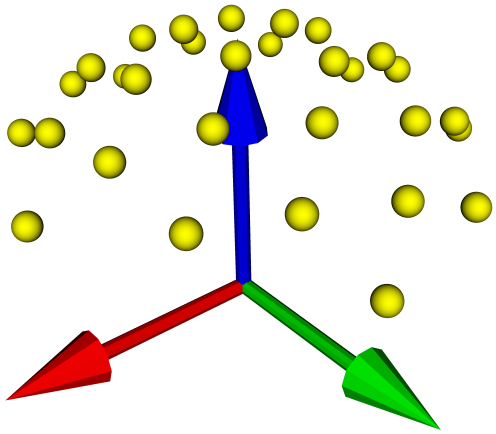

Figure 2.13: dMRI diffusion direction sampling. Yellow points represent the direction of each of the 30 noncolinear diffusion gradients used for the dMRI data. Axis orientations are encoded with color, with red encoding left–right, green anterior–posterior, and blue encoding the superior–inferior direction. As can be seen here, a software error led to nonuniform sampling of the diffusion gradients, with oversampling along the super–inferior axis and undersampling of the orthogonal plane.

techniques.

We note that while quantitative evaluation of the distributions of angular distance in primary fiber orientations (Figure 2.9) and the ACC (Figure 2.10) between fODFs from both modalities are similar to values reported in histological studies[44,47], our results show slightly worse performance from dMRI than expected. We believe this effect is due to the relatively poor angular resolution of the dMRI data collected for this study, which is also why we chose to forego additional efforts to quantitatively evaluate dMRI performance across different reconstruction approaches. Our data were acquired with only 30 diffusion directions which were found after acquisition to be non-uniformly spaced across the sphere (Figure 2.13) due to a software malfunction. Accordingly, we chose to limit reconstructions to $\ell_{\max} = 4$ (15 coefficients) to provide robustness to noise. For this reason, our goal was to introduce microCT and show meaningful, qualitative correspondence between reconstructions from

the two modalities, rather than draw conclusions on the performance of any specific dMRI method. To that end, we are encouraged by the level of multi-modal correlation seen in the fODFs (Figures 2.7–2.12) and believe it demonstrates the utility of synchrotron microCT for future validation studies.

2.4.1 Interpretation of fODFs

The results presented in this study primarily analyze the correspondence of fODFs between the two modalities. It is important to note the differences in interpretation between fODFs derived from microCT and dMRI. Raw dMRI data provide a measure of the restricted diffusion of water in tissue; each measurement is influenced by the local orientation, shape, dispersion, and density of fibers, the free diffusion in extra-axonal water components, and other facets of the local cellular architecture. Structure tensor-derived fODFs from microCT directly estimate the orientation of contrast structures in the data, with nerve fiber orientations selected specifically through thresholding of intensity values and the tensor-derived confidence metric. Accordingly, in microCT, dispersion around the peak value of an individual lobe in the fODF comes from geometric undulation of the corresponding nerve fibers as well as from finite expansion onto SH functions (infinite angular resolution would require $\ell_{\max} = \infty$). In other words, microCT fODFs are representations of fiber geometries, not of water diffusion. Use of these fODFs as ground-truth for dMRI is justified to the extent that they are compared to dMRI reconstructions that also seek to provide representations of fiber geometries. The spherical deconvolution method used in this work estimates a single "fiber response" function from the data that describes how individual point-like fiber orientation distributions map to a dMRI signal, then uses this response to reconstruct fiber orientations from the data. Like microCT, dispersion around fODF peaks derived in this manner comes from geometric undulation of nerve fibers and finite expansion onto SH functions, but also from sub-cellular diffusion effects and error associated with the response function estimation

and deconvolution process. In effect, comparison with ground-truth fODFs can provide evaluation of the conditions and fiber geometries under which the assumptions underlying this and other dMRI reconstruction methods hold.

2.4.2 Comparison of microCT with optical methods

This study set out to probe the ability of whole-brain synchrotron x-ray microCT to function as a ground-truth modality for the validation of dMRI while specifically addressing some limitations in optical-based validation techniques. Optical imaging techniques achieve in-plane resolutions on the order of hundreds of nanometers. For volumetric acquisitions, however, the through-plane resolution is significantly higher, dictated by slice thicknesses on the order of tens of microns and the limits of deconvolution methods for volumetric acquisitions. Accordingly, while in-plane optical images are sufficient for resolving individual myelinated axons and other details of neural tissue microstructure, the limited through-plane resolution and geometric corrections required after tissue sectioning complicate the 3D reconstruction of large volumes and might bias the estimation of microstructural features relevant to dMRI validation, such as 3D fiber orientations. The microCT data used in this study has a nominal resolution of 1.17 μm. While this is lower than the in-plane resolution achievable through optical methods, our results show that it is sufficient for resolving the orientation and structure of local fiber bundles, microvasculature, and cell bodies. Importantly, the data are natively volumetric upon acquisition, with isotropic resolution across the whole brain, avoiding the need for extensive post-processing to estimate the true architecture of the neural tissue.

Limitations on feasible data acquisition times and storage have required previous optical-based dMRI validation studies to preselect a fixed number of specific ROIs for high-resolution 3D imaging, based either on prior anatomical knowledge[44] or through automated, data-driven approaches[48]. Alternatively, synchrotrons provide enough x-ray flux to image the entire mouse brain at full resolution with sufficient a signal-to-noise ratio in a single day

of data acquisition. This provides much more high-resolution, volumetric data for each specimen and removes potential user bias in the selection of individual regions for validation.

Optical imaging methods rely on neural tracer injections to map long-range fiber pathways for validation of dMRI tractography and connectivity studies. These methods provide unparalleled specificity at the cost of only allowing one injection per dataset, which prohibits multi-modal comparisons of whole connectomes in individual specimens. We have shown in previous work[63] the potential for direct tracing of individual axons in synchrotron microCT datasets without the need for neural tracers. This direct approach is not feasible with standard optical methods, as slice cutting and mounting are associated with tissue distortions[56] that make it prohibitively challenging to reliably trace individual axons across slice boundaries after digital alignment. The tractography results presented in this study suggest an additional benefit of the whole-brain information available with microCT. With fODFs available across the whole brain, tractography can be applied to fiber orientations derived directly from the ground-truth dataset and correlated with axon tracings and dMRI tractography all in the same specimen. This rich validation dataset can be used to better understand the upper bounds of tractography performance in dMRI data and to explore new approaches and priors to better condition the tractography problem.

This work also demonstrates that volumetric imaging of whole samples with microCT greatly eases the spatial registration challenge for multi-modal comparison studies (Figures 2.4 and 2.7). Optical-based dMRI validation studies have typically depended on complicated, multi-step registration pipelines involving multiple histological acquisitions at different scales to map individual histological ROIs to the corresponding dMRI voxels[44,48]. With high-resolution, isotropic voxels across the whole brain, microCT data can be registered directly to MRI using existing registration pipelines after appropriate downsampling.

2.4.3 Future work and limitations

While this study was limited to data from a single specimen, we believe our qualitative results are promising and motivate the collection of additional data for future quantitative dMRI validation studies. Various fODF reconstruction methods will be benchmarked against microCT at different spatial scales, evaluating agreement in fODF shape, peak identification, and fiber dispersion metrics. Furthermore, we have demonstrated in additional work[63] the

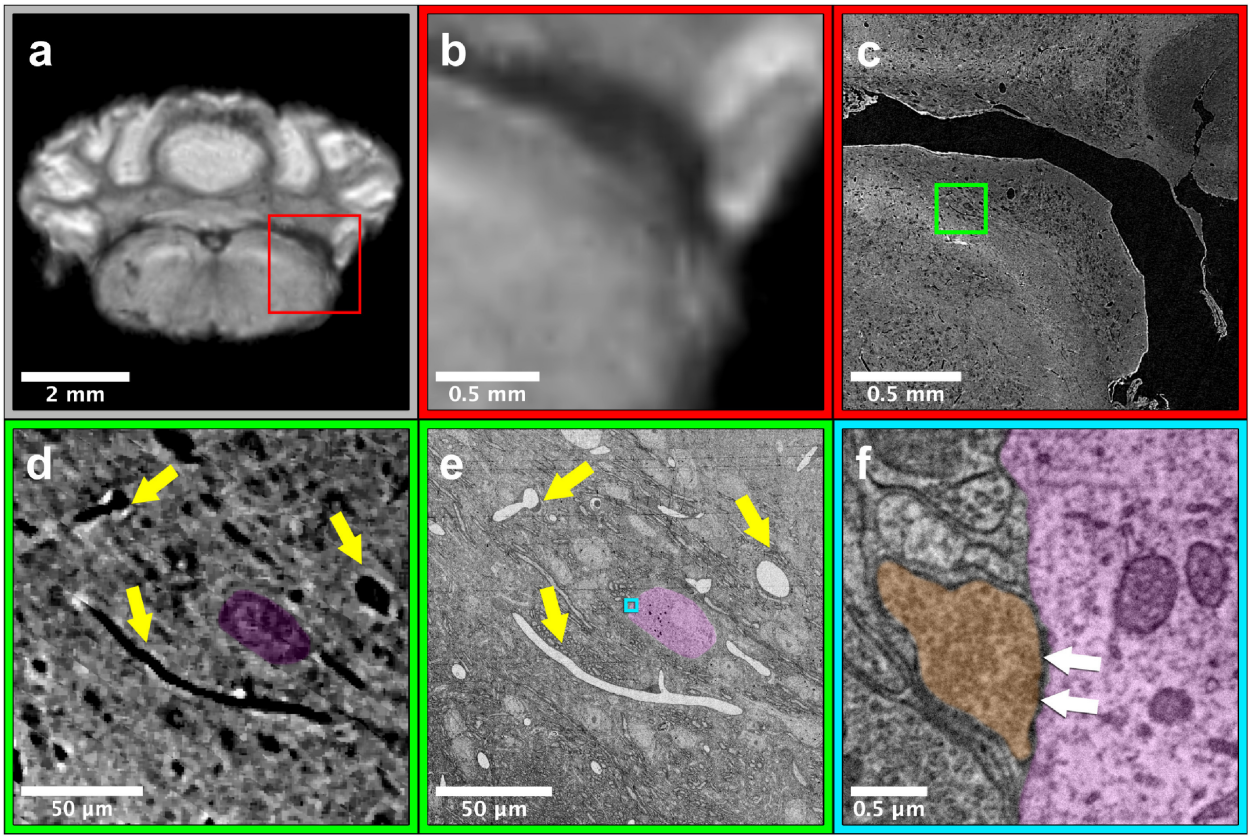

Figure 2.14: A multi-scale, multimodal pipeline for imaging the same brain from MRI to EM. The same brain was imaged using (a–b) diffusion MRI, (c–d) microCT, and (e–f) large volume serial electron microscopy (EM, ~3 nm/voxel resolution). (b–c) show the same field of view from the whole brain MRI and microCT imaging, corresponding to the red ROI in (a). (d–e) show a smaller field of view in both the microCT and EM data, corresponding to the green ROI in (c). Yellow arrows indicate corresponding blood vessels, and a single neuron is labeled purple. Panel (f) highlights an individual somatic synapse (white arrows) on that soma, colored orange. The field of view of (f) is indicated by the blue ROI in (e). This pipeline demonstrates the ability to identify corresponding structures in a single brain imaged across four orders of magnitude of spatial resolution.

potential for subsequent imaging with serial EM on the same sample. Our full imaging pipeline is demonstrated in Figure 2.14. The ability to colocalize structures across multiple orders of magnitude of spatial resolution will allow unprecedented insight into the nanostructural drivers of the diffusion MRI signal.

The tractography results presented in this study (Figures 2.11–2.12) suggest an additional benefit of large-volume microCT. With fODFs available across the whole brain, ground-truth tractography can be correlated with axon tracings and dMRI tractography at different scales in the same specimen. Such a rich dataset could be used in future studies to better understand the upper bounds of tractography performance and to explore new priors to better condition the tractography problem.

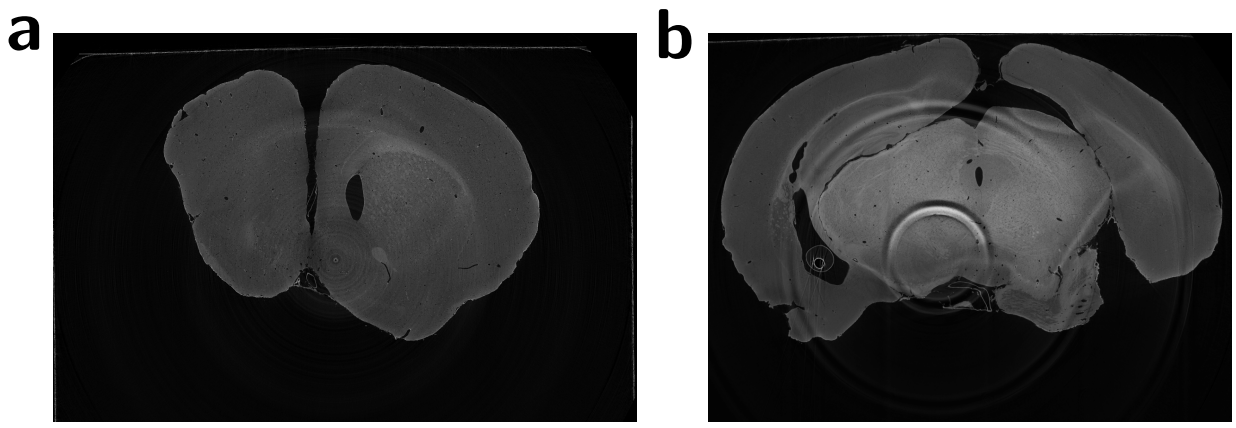

Figure 2.15: Example microCT ring artifacts across coronal slices. (a) Mild artifact. (b) Severe artifact.

While we believe synchrotron x-ray microCT is a valuable tool for dMRI validation, it also presents some limitations. Raw x-ray data are log-normalized by the incident beam intensity profile to account for spatial variation in the synchrotron output. These spatial variations can fluctuate and drift during the data acquisition time due to natural thermal fluctuations at various points in the synchrotron–detector chain, leading to inaccurate normalization that results in the appearance of ring artifacts in the data following tomographic reconstruction. These artifacts vary in severity across the dataset and can particularly bias fiber orientations

in the structure tensor algorithm. Example ring artifacts are shown across coronal slices in Figures 2.15a (mild) and 2.15b (severe). There are a number of successful processing algorithms designed to mitigate this artifact, based on filtering of the sinogram data[87,88] or the reconstructed image[89]. Full correction of this artifact was outside the scope of this work but will be important for future dMRI validation studies.

MicroCT is also limited by the achievable field of view and resolution. The narrow beam width necessitates the use of mosaic tomography for imaging large volumes. The computational challenge of precise sinogram registration currently limits achievable voxel sizes to around one micron, biasing orientation estimates towards fibers of this length scale. With limitations on feasible stain penetration depth, whole mouse brains represent an upper limit of volumes that can be imaged with this method. This prohibits the use of microCT for whole-brain studies of larger species, though smaller brain volumes from these species can still deliver valuable information.

2.5 Appendix: Structure tensor parameter selection

For the structure tensor implementation in this chapter, the image gradient $f(\boldsymbol{r})$ was calculated by convolving the image $f(\boldsymbol{r})$ with the partial derivatives of a gaussian of width σ_D. As discussed in section 2.2.4, the structure tensor is also convolved with a separate gaussian of width σ_N in order to average results across a local neighborhood.

To explore the role of the σ_D and σ_N parameters, a series of phantoms was created consisting of groups of cylindrical fiber bundles crossing at angles from 25–85° in 10° increments. A sample phantom with fiber bundles crossing at 45° is shown in Figure 2.16a–b along with the resulting true fODF in Figure 2.16c. Phantoms were defined to be 150 μm along each dimension in order to match the resolution of the dMRI data. Underlying vasculature patterns were segmented with a simple k-means clustering approach from real data, and the fiber bundles were manually defined as cylinders with a radius of 9.6 μm (8 microCT voxels).

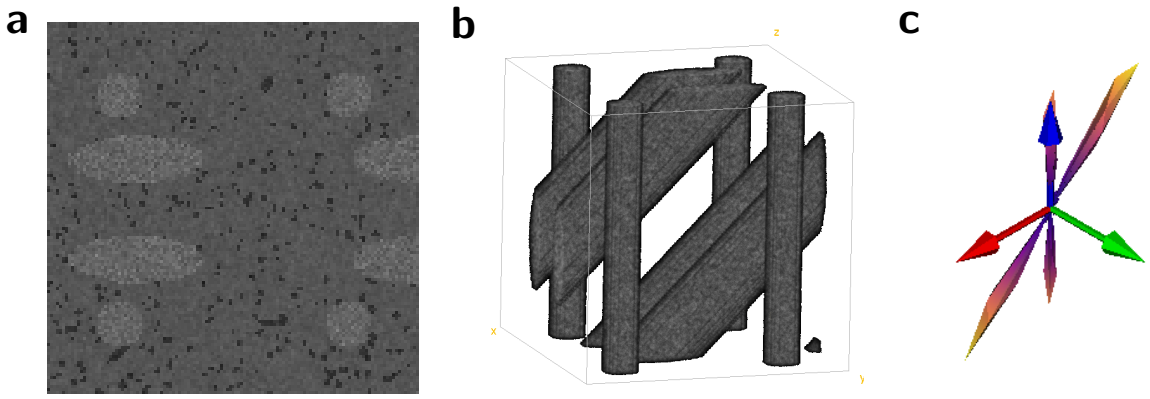

Figure 2.16: Sample structure tensor parameter phantom consisting of two populations of fiber bundles crossing at 45°. (a) 2D cross section. (b) 3D rendering of the fiber masks. (c) True fODF.

fODFs were calculated for each crossing-fiber phantom along a grid of parameter values for both σ_D and σ_N from 1–10 µm in 0.5 µm increments. For each pair of values, the structure-tensor fODF was compared to the true phantom fODF using the ACC. The resulting ACC heatmaps are shown in Figure 2.17.

In general, across all crossing angles, performance was more dependent on σ_D than σ_N, with low values of σ_D leading to a misestimation of the true number of fiber populations (gray pixels in Figure 2.17). Otherwise, the ACC was not found to be particularly sensitive to the choice of parameters, and final values were selected as the average of the optimal values at each crossing angle: $\sigma_D = 7.5$ µm and $\sigma_N = 6.5$ µm. These choices were manually confirmed through visual examination of resulting fODFs using real data, as in Figures 2.5 and 2.7.

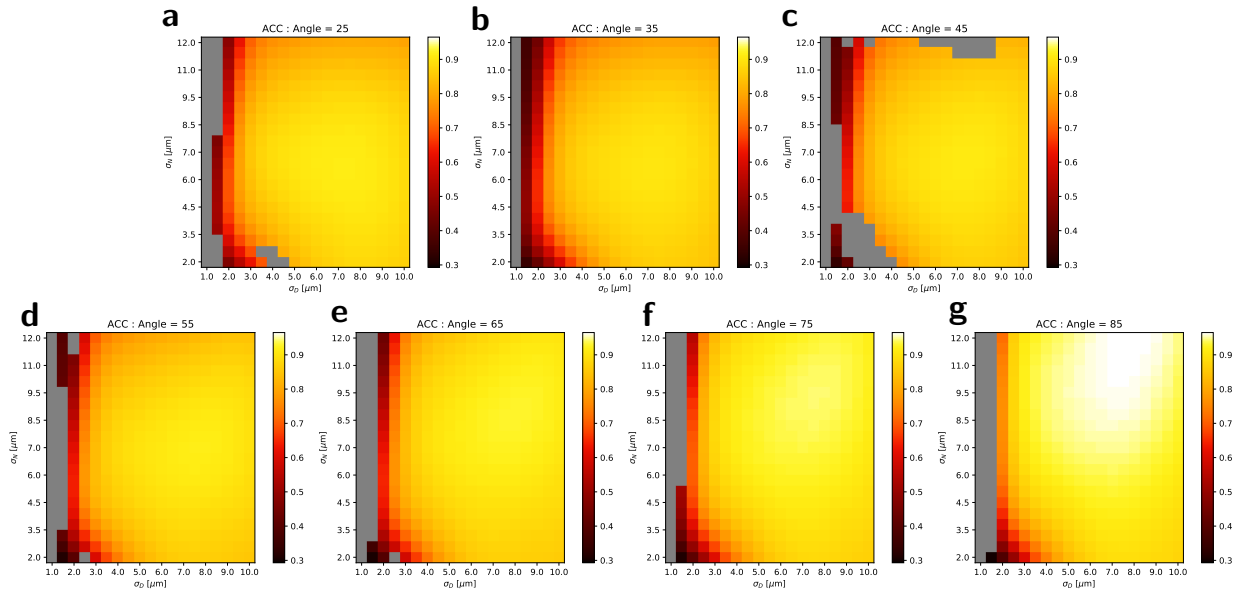

Figure 2.17: ACC heatmaps between the true phantom fODF and the structure-tensor fODF using different combinations of σ_D and σ_N for fiber bundle populations crossing at (a) 25°, (b) 35°, (c) 45°, (d) 55°, (e) 65°, (f) 75°, and (g) 85°. Gray pixels correspond to parameter combinations in which the resulting fODF miscalculated the number of peaks in the true fODF.

CHAPTER 3

VALIDATION OF DMRI BRAIN NETWORKS USING NEURAL TRACER IMAGING

3.1 Introduction

The structural connectome[20] is the comprehensive map of connections among all neurons in the brain. Constructing such a map represents a major frontier in neuroscience that relies on the development of novel imaging techniques across a range of spatial scales and model organisms and will provide insight into the basic function and development of the brain[90] and its pathologies[91]. Diffusion MRI tractography is currently the only noninvasive method for mapping the human structural connectome[92] and forms the basis of research initiatives such as the Human Connectome Project[93]. Together with mathematical tools from graph theory[92,94–96] (see section 3.5), tractography studies have helped reveal a number of important network properties in the human brain such as efficiency[97], modularity[98], and the organization of network hubs[99].

Despite these advances, diffusion MRI also suffers from relatively poor spatial resolution and fundamental ambiguities in the mapping between the underlying white matter fiber orientations and the resulting diffusion signal[100]. Recent efforts to validate tractography have uncovered several limitations, and even modern approaches still produce high numbers of both false positive and false negative tracts[101–104]. A specific limitation inherent to probabilistic streamline tractography is the fiber-length bias: local uncertainties in the fiber orientation distribution at each step in the tracking process accumulate to produce global errors for longer streamlines, leading to an underestimation of connectivity weights at greater distances. Characterizing this sort of geometric bias is complicated by the fact that the brain is itself a spatially embedded network with properties partially inherited from geometry: there is a metabolic wiring cost in the establishment of long-range connections, and true

falloff of both structural and functional connectivity with distance has been shown with high-resolution invasive imaging as well as tractography in a number of mammalian species[105–110]. With tractography alone, it is challenging to distinguish the role spatial embedding plays in the true network properties of the brain from the potentially exaggerated representation of that geometric effect resulting from biases inherent to the imaging process.

To characterize methodological biases and improve tractography approaches, tractography experiments need to be validated with additional high-resolution imaging. Neural tracer data is the gold standard for mesoscale connectivity studies in a number of model organisms[106,111–115]. Data from the Allen Institute Mouse Brain Connectivity Atlas[112] (AMBCA) form the most comprehensive whole-brain mesoscale brain network in a mammalian species. The AMBCA dataset was constructed using enhanced green fluorescent protein-expressing adeno-associated viral vectors to trace axonal projection pathways from cell bodies located within a given tracer injection region to corresponding axon terminals located throughout the brain. After infection, the animal is sacrificed and its whole brain imaged using serial two-photon tomography[116]. For the AMBCA database, hundreds of such experiments were performed with injection regions spanning an entire hemisphere of the brain. For each experiment, fluorescent signals were segmented to generate projection density images which were then registered to the Allen Reference Atlas[117] to create a single mesoscale structural mouse brain connectome. This database has been used in multiple previous tractography validation studies, primarily to characterize agreement in voxel-wise streamline density maps with consideration for the role of specific algorithm parameters[53,104,118].

In this chapter, we expand the use of the Allen Institute tracer data as a validation tool for tractography connectomics in the mouse brain. Specifically, we use a graph-theoretical approach previously developed for human tractography data[108] of benchmarking empirical brain graphs against an ensemble of random geometric surrogates. The random geometric surrogate graphs are constructed from each empirical graph in such a way that the node

strength distribution and low-order relationships between connectivity and fiber distance are preserved, but the topology is otherwise destroyed, allowing for determination of the extent to which certain properties of the mouse structural brain network can be explained through spatial embedding alone.

Previous studies have also explored the influence of spatial embedding and geometry on the topology of the structural brain network in different mammalian species[105–108,119]. While many of these studies explored the results in an evolutionary context in terms of pressures of wiring cost and efficiency[120], our aim is instead to use the same tools across the two imaging modalities to specifically assess methodological geometric bias in tractography, taking the tracer-derived network as a significantly higher-fidelity representation of the true mesoscale connectome of the mouse brain. Furthermore, we explore the performance of different tractography approaches by assessing the use of two different streamline node assignment strategies. Accordingly, our analysis aims to do two things: (1) explore and compare the role spatial embedding plays in the topology of graphs derived from tractography and neural tracer imaging and (2) explore the extent to which graphs constructed from different tractography methods reflect the topological properties observed in the empirical tracer model.

3.1.1 Author contributions

This chapter was originally published in *NeuroImage* under the title "The role of spatial embedding in mouse brain networks constructed from diffusion tractography and tracer injections"[121] with co-authors Sean Foxley, Gregg Wildenberg, Narayanan Kasthuri and Patrick La Rivière. The author was responsible for the conception of the project and all analysis, figures, and text in the chapter, while the co-authors were responsible for sample preparation, data acquisition, and manuscript review.

3.2 Methods

3.2.1 Construction of the primary tracer graph

Our work uses a high-resolution model of the Allen Institute mouse brain structural brain network published by Knox et al.[122] The Knox et al. model provides estimates of connectivity at the scale of 100 µm isotropic voxels in the Allen Mouse Brain Common Coordinate Framework (CCF v3), and is derived from 428 whole-brain anterograde fluorescent viral tracer experiments in wild-type C57BL/6J mice collected for the AMBCA[112]. Underlying tracer data are available at http://connectivity.brain-map.org. The Knox et al. model can be accessed publicly through the repository available at https://github.com/AllenInstitute/mouse_connectivity_models. While derived from tracer experiments with injection locations that may span multiple distinct regions, the model allows for the efficient creation of regionalized connectivity models using custom brain parcellations based on labeled structures in the Common Coordinate Framework. For this study, we chose to define graph nodes as 286 of the 291 gray matter regions used to construct the regionalized voxel model analyzed in Knox et al[122]. Five small regions were excluded due to being located almost exactly along the sagittal midline. A full list of gray matter structures used for the parcellation is available in section 3.7. The model allows for four different connectivity metrics. Our tracer graph was constructed using the normalized connection density metric, which takes raw projection volume fractions and normalizes them by the volume of the source and target regions for each edge. The anterograde tracers used to produce the Knox et al. model provide a directed graph, whereas tractography graphs are derived from symmetric diffusion data and inherently produce undirected graphs. For fair comparison, the tracer graph was manually made to be undirected by summing all bidirectional connectivity between every pair of nodes. The AMBCA also assumes hemispheric symmetry, as all underlying tracer images were formed from injections into the right hemisphere. Hemispheric

symmetry was manually enforced in the final graph in order to yield square connectivity matrices for subsequent analysis.

3.2.2 Additional tracer data

The Knox et al. model has been shown to outperform the homogeneous model originally published in Oh et al.[112] and produces a graph that is nearly 100% fully connected at the scale of the parcellation used in this study. The true density of the whole mouse brain network is an ongoing subject of research. Initial modeling of the Allen Institute data estimated cortical density to vary from 32–52%[112] to 59-73%[123]. A recent study by Gămănuţ, et al.[124] observed a much higher cortical density in the mouse brain of 97% using tract-tracing measurements from independent retrograde tracer data. While only available for select ipsilateral intra-cortical edges, the Gămănuţ, et al. data have the benefit of representing empirical neuron counts that do not rely on the fixed parcellation template and downstream computational modeling required for the Knox et al. model. Accordingly, our cortical tractography connectivity weights were further benchmarked against these additional weighted connectivity data provided by the authors. These edge-weight values correspond to neuron count fractions within manually defined gray-matter region boundaries corresponding to the parcellation from the Allen Institute (Figure S6B in Gămănuţ, et al.[124]). As with the Knox et al. model, the Gămănuţ, et al. cortical subgraph was manually made to be undirected by summing bidirectional connectivity weights between every pair of nodes.

3.2.3 Animal procedures

Procedures for the collection of the diffusion MRI data used for this study have been published in a previous study[125] and are repeated here for completeness. All procedures performed on animals followed protocols approved by the Institutional Animal Care and Use Committee and were in compliance with the Animal Welfare Act and the National Insti-

tutes of Health Guide for the Care and Use of Laboratory Animals. Five adult mice were deeply anesthetized with 60 mg/kg pentobarbital and sacrificed by intercardial perfusion with a solution (pH 7.4) of 0.1 M sodium cacodylate and heparin (15 units/ml). This was immediately followed by a solution of 2% paraformaldehyde, 2.5% glutaraldehyde, and 0.1 M sodium cacodylate (pH 7.4). Brains were carefully removed from the skulls and post-fixed in the same fixative overnight at 4°C. Brains were soaked in phosphate buffered saline (PBS) prior to imaging for at least 72 hours to remove fixative from the tissue.

3.2.4 Diffusion MRI acquisition

Resected mouse brains were dried of excess PBS and placed in 10 ml Falcon tubes. Tubes were filled with Fluorinert (FC-3283, 3M Electronics) for susceptibility matching and to improve shimming. Data were acquired at 9.4 T (20 cm internal diameter, horizontal bore, Bruker BioSpec Small Animal MR System, Bruker Biospin, Billerica, MA) using a 6 cm high performance gradient insert (maximum gradient strength: 1000 mT/m, Bruker Biospin) and a 35 mm internal diameter quadrature volume coil (Rapid MR International, Columbus, Ohio). Third-order shimming was iteratively performed over an ellipse that encompassed the entire brain, but did not extend beyond the boundaries of the Falcon tube/Fluorinert interface, using the Paravision mapshim protocol. Diffusion MRI was performed using a standard diffusion-weighted 3D spin-echo sequence (TR = 600 ms, TE = 11.389 ms, b-value = 3000 s/mm^2, δ = 3.09 ms, Δ = 6 ms, spatial resolution = 125 µm isotropic, number of b0s = 8, number of directions = 30, receiver bandwidth = 150 kHz, duration = 36h 28min 48s).

3.2.5 Diffusion MRI processing

Data and diffusion gradient vectors were manually reoriented to the standard RAS neurological display convention. Subsequent processing was performed with the MRtrix3 software package[126]. Data were denoised using the dwidenoise protocol[68,69]. Binary brain masks

were generated for subsequent processing using the dwi2mask routine. The data were first fit to a diffusion tensor model[10] to calculate the fractional anisotropy metric[30]. The data were then fit to fiber orientation distribution functions (fODFs) using constrained spherical deconvolution[16,17] up to a maximum spherical harmonic order of $\ell_{\max} = 6$ (28 coefficients). The fractional anisotropy image from each dataset was spatially registered to the Allen reference mouse brain template at an isotropic voxel size of 100 µm using affine and diffeomorphic transformations calculated with the ANTS registration package[80,81]. The Allen template and structure-level annotations in the Common Coordinate Framework were accessed using the allensdk software tool (https://allensdk.readthedocs.io). The spatial transforms calculated in ANTS were then applied to the fODFs using the mrtransform protocol in MRTrix3, which applies appropriate reorientation[82] and modulation[18] of the fODFs in order to preserve fiber densities across each lobe after transformation.

3.2.6 Construction of tractography graphs

Probabilistic tractography was performed in MRTrix3 using the iFOD2 algorithm[86] (step size = 12.5 µm, maximum curvature = 30 µm, minimum length = 0.5 mm, maximum length = 30 mm, fODF cutoff = 0.055). Streamlines were seeded uniformly throughout each of the 286 gray matter regions in the right hemisphere used in the regionalized tracer model, with 2000 seeds per voxel, amounting to around 400 million total streamlines per dataset. Edge weights were determined from each tractography dataset using two different streamline node assignment strategies in order to compare their effects on downstream network structure. For "endpoint" connectivity, streamlines were assigned to the two nodes corresponding to the gray matter regions closest to their endpoints, within a maximum radius of 125 µm, corresponding to the size of the underlying diffusion data voxels. For "dense" connectivity, streamlines were assigned to all node-pairs corresponding to pairs of gray matter regions they traverse, not just those corresponding to their endpoints. Edge-weight values between two

nodes were then taken to be the number of streamlines assigned to the two nodes under both endpoint and dense assignment strategies, resulting in two different graphs per tractography dataset. To match the normalized connection density metric used for the tracer graph, the weights for each node pair were then divided by the product of the two node volumes. As with the tracer graph, hemispheric symmetry was manually enforced to create square connectivity matrices. Also similar to the tracer graph, the probabilistic tractography seeding used in this work led to nearly fully connected graphs.

3.2.7 Construction of surrogate graphs

The goal for the construction of geometric surrogate graphs was to create an ensemble of graphs that preserve both the distribution of node strengths (the sum of weights at each node) and the low-order weight-distance relationships of a given empirical graph but are otherwise random. Geometric surrogate graphs were constructed from all empirical tracer and tractography graphs by directly following the methodology described in Roberts et al.[108], repeated here for completeness. First, the fiber distance between each pair of nodes was quantified based on tractography results. The distance f_{ij} between nodes i and j was defined as the length of the shortest streamline connecting them, averaged across all datasets. To estimate first-order weight-distance effects, we follow Roberts et al. in fitting the logarithm of the edge-weights w_{ij} to a curve given by $\log w_{ij} \approx g(f_{ij})$, where g is a cubic polynomial. This relationship was subtracted from the raw weights, and an additional parabolic curve was then fit to the residuals. After normalizing by this second curve, low-order distance-dependent effects were effectively removed from the weight values and they were randomly shuffled. After randomization, the transformations were applied in reverse order to reimpose low-order weight-distance effects. The original weight values were then reordered to match the random rank order of the surrogate weights. Finally, the node-strength distribution was restored using an iterative procedure that updates the sums of the rows and columns of the

surrogate weight matrix towards the empirical values.

This procedure resulted in an ensemble of geometric surrogate graphs W_{geo} for each network construction method that preserve the low-order distance-dependent characteristics and node-strength distribution of the underlying empirical graph W_{emp}, but have all other topological properties destroyed. We make the assumption that network properties that are preserved in the geometric surrogate graphs represent those that have been inherited from the spatial embedding of the brain. Likewise, we assume that differences in network properties between empirical and geometric surrogate graphs represent the extent to which those properties arise from other, non-geometric factors.

A similar procedure without the use of distance transformations was used to construct an ensemble of random surrogate graphs W_{rand}, which preserve the exact strength-sequence of the underlying empirical graphs, but are otherwise completely random. The geometric surrogates W_{geo} represent the null hypothesis that topological properties of brain networks arise from the falloff of edge weights with distance for a given node-strength distribution, while the random surrogates W_{rand} represent the null hypothesis that topological properties of brain networks arise solely from the particular distribution of node strengths and locations.

3.3 Results

Here we report analysis of brain networks constructed using tracer imaging data and two tractography approaches: "endpoints" and "dense" corresponding to two methods of streamline node assignment. For each metric, our goal is to explore how graphs from each tractography approach compare to the tracer graph, specifically with respect to the relationship between empirical and geometric surrogate graphs. Unless otherwise noted, all results labeled "tracer" correspond to the whole-brain graph derived from the Knox et al. connectivity model. All analysis was performed in Python, with graph theoretical measures calculated using the networkx package[127].

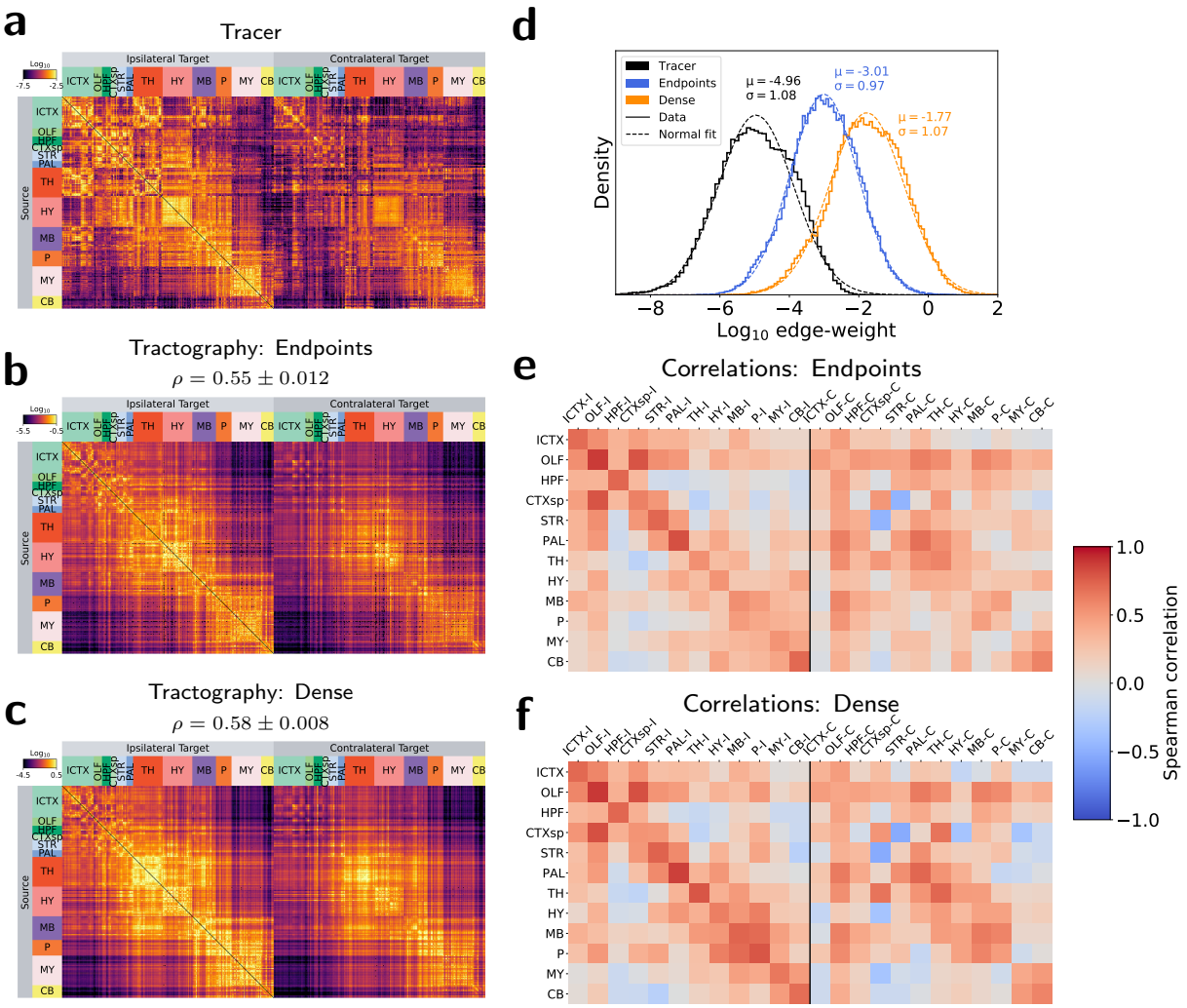

Figure 3.1: Edge-weight values. (a–c) Connectivity matrices for (a) tracer, (b) endpoint tractography, and (c) dense tractography. Rows represent nodes comprised of 286 gray matter regions across 12 major brain divisions. Columns represent the same nodes for ipsilateral (left) and contralateral (right) connections. Values are shown on a log-color scale spanning five orders of magnitude centered on the mean edge-weight value for each matrix. ρ values represent Spearman rank correlation coefficients between tractography and tracer weights across the whole brain. (d) Edge-weight distributions. Empirical weight histograms (solid lines) with corresponding normal fits (dashed lines). (e–f) Spearman correlations between tracer and (e) endpoint and (f) dense tractography edge-weights across 12 major brain divisions: Isocortex (ICTX), Olfactory areas (OLF), Hippocampal formation (HPF), Cortical subplate (CTXsp), Striatum (STR), Pallidum (PAL), Thalamus (TH), Hypothalamus (HY), Midbrain (MB), Pons (P), Medulla (MY), Cerebellum (CB). "-I" and "-C" in (e–f) refer to ipsilateral and contralateral correlations, respectively. All tractography values represent averages across 5 datasets.

3.3.1 Comparison of edge-weight values

Structural connectivity matrices and edge-weight distributions are shown for all empirical graphs in Figures 3.1a–c. Differences in the mean weight values across tractography approaches in Figure 3.1d follow predictable trends: dense node assignment resulted in higher weights than endpoint node assignment. Note that the physical interpretation of edge weights differs between modalities, so direct comparison of the edge-weight means between modalities is not meaningful. Tracer weights reflect normalized projection volumes and tractography weights reflect normalized streamline counts under different node assignment strategies. Regardless, edge-weight distributions had a comparable and approximately log-normal shape for all empirical graphs.

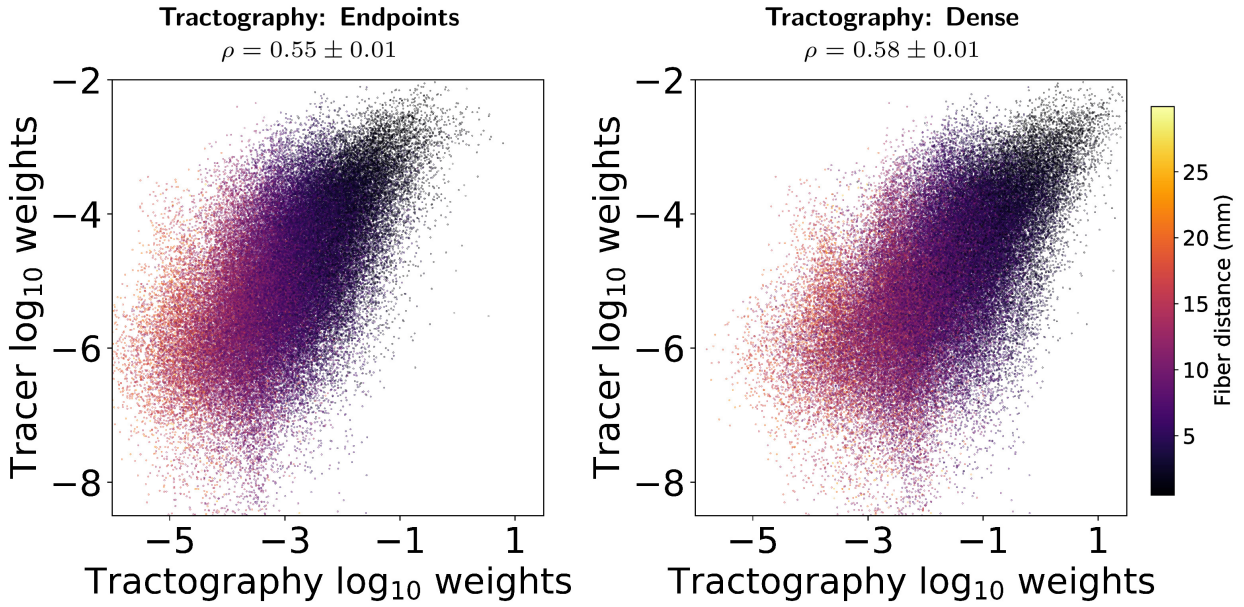

Figure 3.2: Scatterplots of the log-weights for tracer vs. tractography connectivity matrices. Color indicates fiber distance. Tractography weight values represent averages across 5 datasets. ρ values indicate Spearman rank correlation coefficients, with standard deviations across 5 tractography datasets.

Overall agreement in edge-weight values was assessed using the Spearman rank correlation coefficient, a nonparametric correlation metric used in previous studies[53,128] to assess nonlinear agreement between connectivity values. Spearman correlation values between tracer

and tractography weights across all edges are shown above each tractography matrix in Figures 3.1b–c. Edge weights constructed with dense node assignment had a slightly higher Spearman correlation with the tracer weights than those constructed with endpoint node assignment. The difference in correlations was statistically significant ($p < 0.01$) using a t-test. Scatterplots of edge weights between the tracer and tractography graphs are available in Figure 3.2.

Spearman correlations between tractography and tracer weights assessed at the level of major brain divisions are shown in Figures 3.1e–f. All tractography methods showed relatively high correlations in ipsilateral intra-division connectivity (diagonals in Figures 3.1e–f), and weaker contralateral connectivity to homologous regions, reflecting not only a falloff in weight for longer-distance connections, but a falloff in agreement with tracer values. Dense node assignment led to higher Spearman correlations than endpoints for nearly all connections to the pons, and for connections between the hypothalamus, midbrain, and medulla.

3.3.2 Comparison of weight-distance relationships

The raw weight-distance distributions and polynomial fits used to construct the geometric surrogate graphs are available in Figure 3.3a–b. Transformed weights (Figure 3.3c) show effectively zero correlation with fiber distance using both Pearson and Spearman correlation coefficients, indicating that low-order distance relationships have been effectively removed prior to randomization for the construction of the geometric surrogate graphs. Sample connectivity matrices from empirical and geometric surrogate tracer graphs are shown in Figure 3.4. The visible structure that persists from the empirical matrix to the geometric surrogate matrix corresponds to connectivity patterns that can be explained in part through the weight-distance relationship.

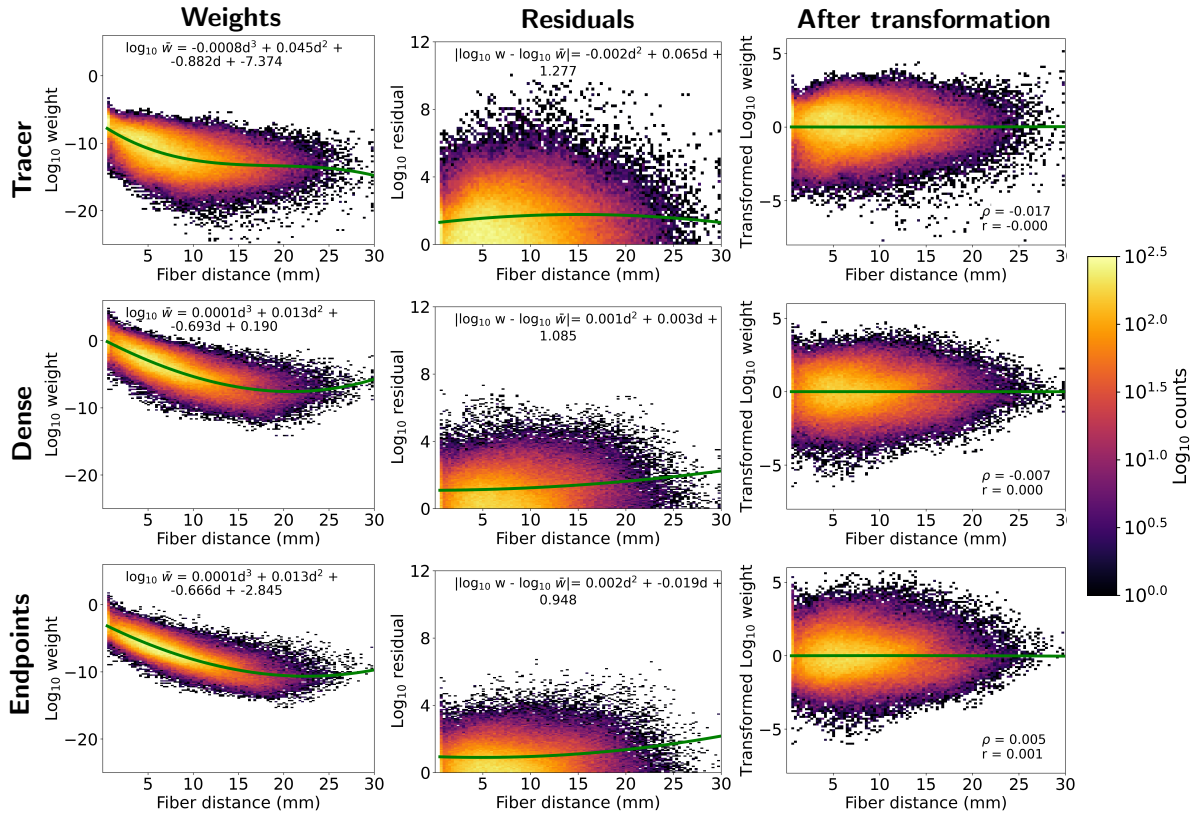

Figure 3.3: Distance curves for weights (left) and residuals (center) for all network construction methods. The resulting weight-distance relationships after transformation are shown on the right with corresponding linear fits (green line). r and ρ values indicate Pearson and Spearman correlation coefficients, respectively. Counts of individual edges within weight-distance bins are represented as a heatmap on a log color scale. Polynomial fits are shown as green curves. Tractography values represent averages across 5 datasets.

Because the weight values have different physical interpretations for each network construction method, the weight-distance relationships cannot be directly compared. Instead, Figure 3.5 visualizes the relative relationships between methods after the log-weights were first standardized to zero mean and unit variance. Figure 3.5a shows the relative falloff of mean normalized log-weights with fiber distance, and Figure 3.5b shows the change in the standard deviation of normalized log-weights with fiber distance for each method.

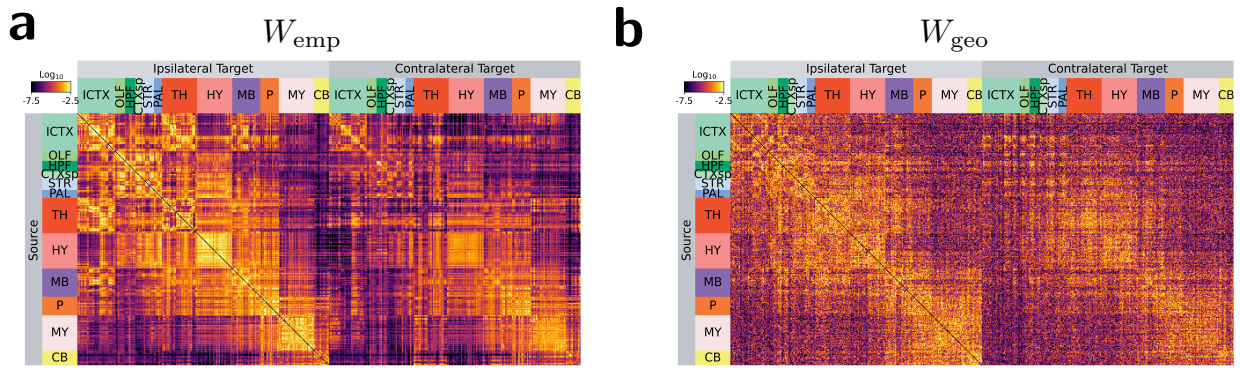

Figure 3.4: Sample connectivity matrices for (a) W_{emp} and (b) W_{geo} graphs from the tracer model data.

The mean normalized weight-distance curves from both tractography graphs in Figure 3.5a fall below the corresponding tracer curve for distances above around 10 mm, with both tractography methods showing statistically significant differences from tracers for fiber

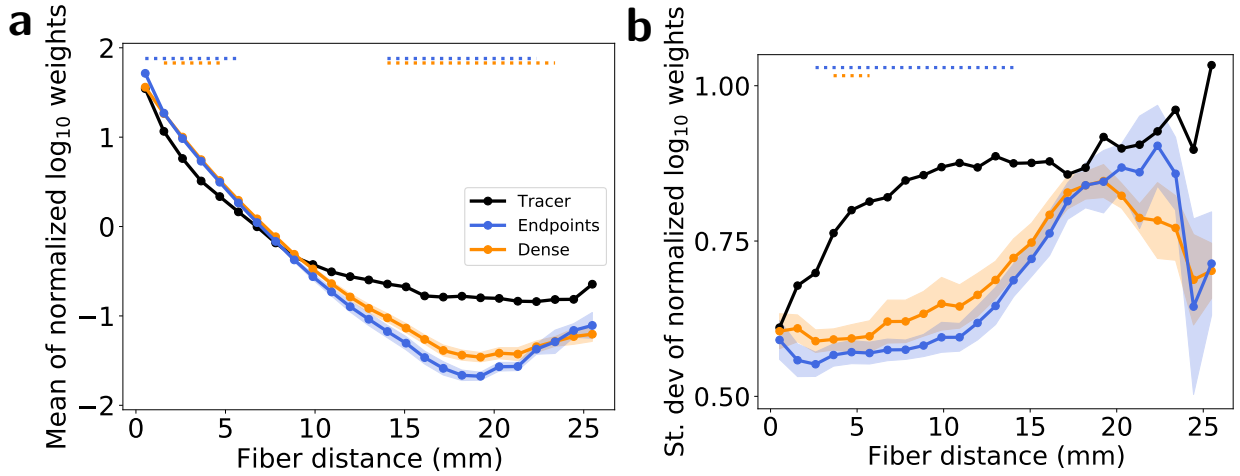

Figure 3.5: Normalized weight-distance relationships. (a) Circles represent the average log-weight z-scores for each method within 1 mm fiber distance bins. (b) Circles represent the standard deviation of the log-weight z-scores for each method within 1 mm fiber distance bins. Shaded regions represent 1 standard deviation across 5 tractography datasets. The widths of the horizontal lines at the top of each subfigure indicate the range of fiber distance bins with statistically significant differences ($p < 0.01$) between tracer and tractography values for each tractography method, calculated using a one-sample t-test after correcting for multiple comparisons.

distance between around 17-22 mm. These results suggest that the tractography methods

explored in this work underestimate relative long-range connectivity by as much as two orders of magnitude. For most fiber distances, both tractography methods also underestimate the standard deviation of normalized weights compared to tracers. A smaller relative standard deviation around the mean weight-distance relationship is consistent with tractography weights being more strictly determined by fiber distance than tracer weights are, though these differences were only statistically significant between around 3–15 mm for endpoint node assignment and for a smaller range around 4–6 mm for dense node assignment.

3.3.3 Comparison of network organization

Modular structure

The modular structure of each brain graph was determined by optimizing the modularity (Q) using the Louvain algorithm[129]. Modularity expresses the extent to which a graph can be subdivided into distinct modules such that intra-modular connectivity is maximized and inter-modular connectivity is minimized[130]. The confusion matrices for consensus node-module assignments are shown in Figure 3.6 for comparisons between empirical tractography and tracer modules as well as between empirical and geometric surrogate modules for all methods. Consensus node-module assignments represent the module ID label most frequently assigned to each node across 5 tractography datasets and ensembles of 100 geometric surrogates. ID labels were first standardized across tractography and geometric surrogate graphs by assigning labels to identified modules such that the overall agreement with the identified modules in the empirical tracer graph was maximized.

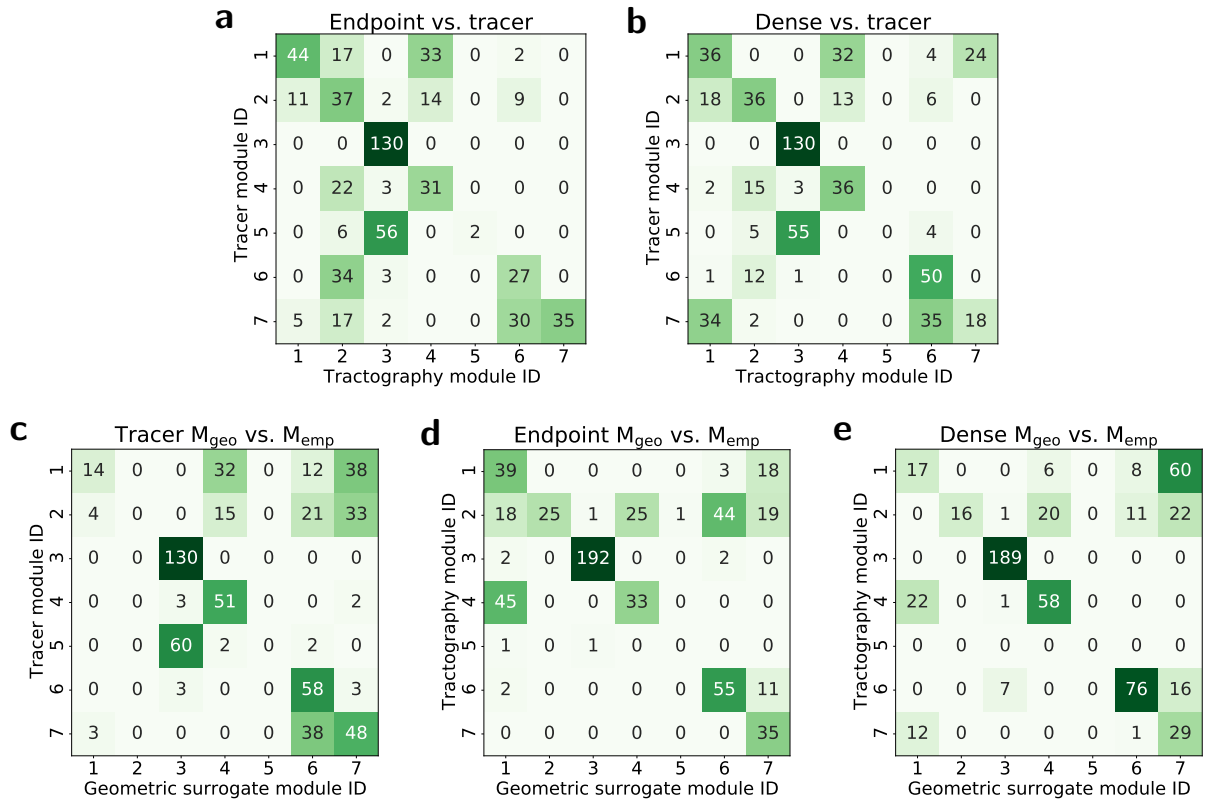

Figure 3.6: Confusion matrices for module assignment. Module IDs correspond to those identified with the colorbar in Figure 3.7. (a–b) Module assignments between empirical tracer and empirical (a) endpoints and (b) dense tractography graphs. (c–e) Assignments between empirical (c) tracer, (d) endpoint, and (e) dense graphs and those from their corresponding geometric surrogate graphs. Values represent consensus assignments across 5 tractography datasets and an ensemble of 100 geometric surrogate graphs.

The resulting consensus modular decompositions are visualized in physical coordinates for the empirical and geometric surrogate graphs derived with all network construction methods in Figure 3.7. Spheres represent the physical location of distinct gray-matter nodes, which are colored according to their identified module. Intra-module edges are also visualized as colored lines. Overall, modules identified in the tractography networks are much more spatially clustered together than those in the tracer network. Intra-module edges are more likely to be shorter range for both tractography methods than for tracers, consistent with tractography modular structure being partially determined by geometric bias against long-

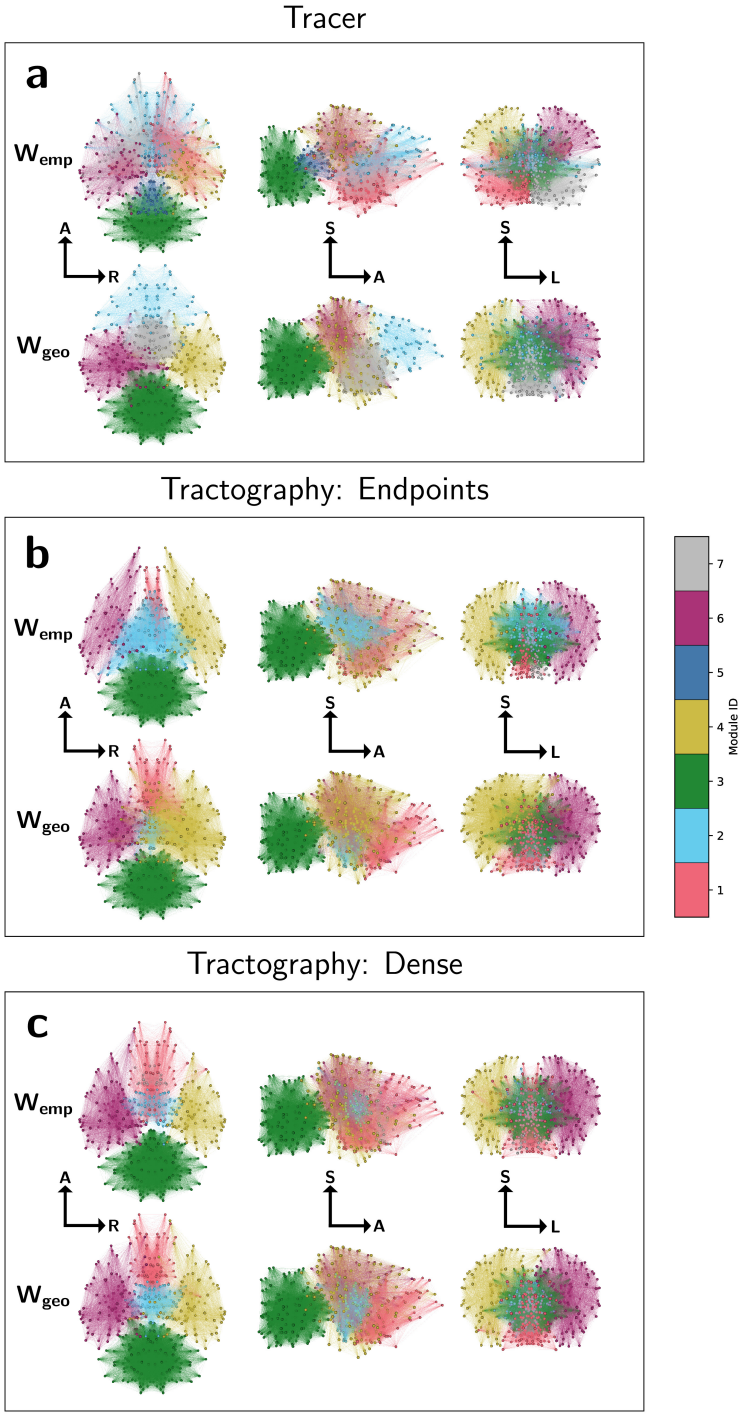

Figure 3.7: Module diagrams for (a) tracer, (b) endpoint, and (c) dense graphs in physical coordinates. Spheres represent the center of mass of each node, colored by module assignment. Intra-module edges are shown as colored lines. Graphs are visualized along the axial (left), sagittal (middle), and coronal (right) planes with labeled orientations: A=anterior, S=superior, R=right, L=left. Module assignments represent consensus values across 5 empirical tractography graphs and an ensemble of 100 geometric surrogate graphs.

range connections. This result

	Tracer	Endpoints	Dense
Tractography vs. tracer	—	54	54
Empirical vs. geometric surrogates	53	66	67

Table 3.1: Percent agreement in consensus node-module assignment.

is further quantified in Table 3.1, which shows the percent agreement in node-module assignment for pairs of graph construction methods. Graphs from both tractography methods show only modest agreement in module assignment with the tracer graph. The tracer graph also shows only modest agreement in module assignment with its geometric surrogates, suggesting that modules in the true mouse brain network are less spatially clustered than they would be if determined by geometry alone, while both tractography methods show much higher overlap in module assignment between their empirical and geometric surrogates.

The optimized Q value itself is a metric of network segregation, indicating a capacity for specialized processing to occur in different regions of the brain. Raw Q values are shown for all graphs in Figure 3.8a. Figure 3.8b shows the empirical Q values normalized by the Q values from their corresponding random surrogate graphs, W_{rand}, constructed by randomly shuffling weights within each empirical graph such that the node strength sequence is preserved. While raw Q values are comparable between the tracer and two tractography graphs, the tracer graph shows a substantially higher W_{rand}-normalized modularity relative to all tractography methods, suggesting that tractography graphs underrepresent the modularity of the mouse structural brain network beyond what would be expected from a random graph with the same strength sequence. In Figure 3.8c, empirical Q values have been normalized

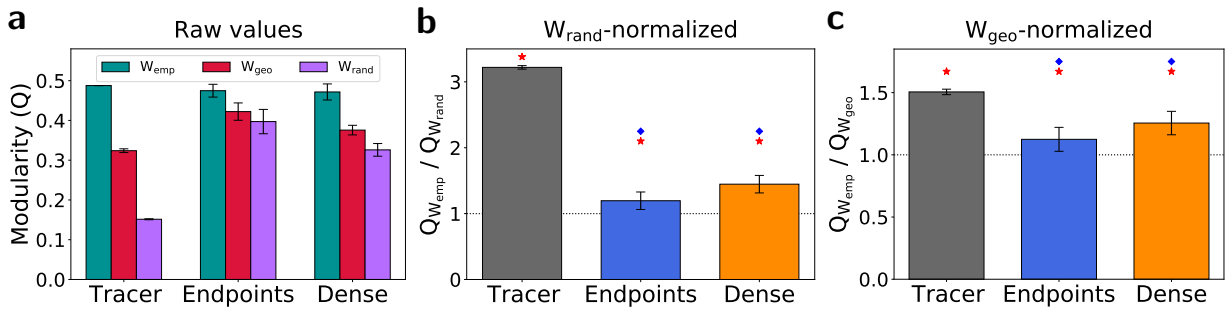

Figure 3.8: Modularity. (a) Raw Q values for empirical (W_{emp}), geometric surrogate (W_{geo}), and random (W_{rand}) surrogate graphs. Error bars represent 1 standard deviation across 5 tractography datasets for empirical graphs, and 1 standard deviation across ensembles of 100 geometric and random surrogate graphs per method. (b) Empirical Q values normalized by their corresponding mean random surrogate Q value. (c) Empirical Q values normalized by their corresponding mean geometric surrogate Q value. Red stars indicate statistical significance ($p < 0.01$) in the difference between W_{emp} and W_{geo} data calculated with Tukey's range test, and blue diamonds indicate statistical significance ($p < 0.01$) in the difference between W_{rand}- and W_{geo}-normalized tracer and tractography data, calculated with a permutation test.

by the Q values from their corresponding geometric surrogate graphs. This ratio represents the additional modular structure present in the empirical graphs beyond what would be predicted by spatial embedding alone, with a ratio of 1 indicating complete geometric determination. Both tractography methods show values significantly closer to 1 than the tracer graph does. Overall, these results suggest that modular structure in the mouse structural brain network is both underestimated overall and more geometrically determined in tractography relative to neural tracer imaging.

Hub node organization

The arrangement of the subnetwork of central "hub" nodes is key to understanding overall brain network structure. Hub nodes can be identified using a number of complementary centrality measures. The participation coefficient P is based on a particular modular decomposition and expresses the diversity of intermodular connections for a given node, with a value of 1 indicating a node is connected uniformly to all modules and a value of 0 indicat-

ing a node is connected exclusively to its own module[130,131]. Figure 3.9 shows scatterplots of participation coefficients for empirical tractography and tracer graphs (Figure 3.9a–b) and for each empirical graph method and its geometric surrogates (Figure 3.9c–e). Both tractography methods show only weak correlation with the values from the corresponding tracer graph, but significantly stronger correlations with the values from their own geometric surrogates.

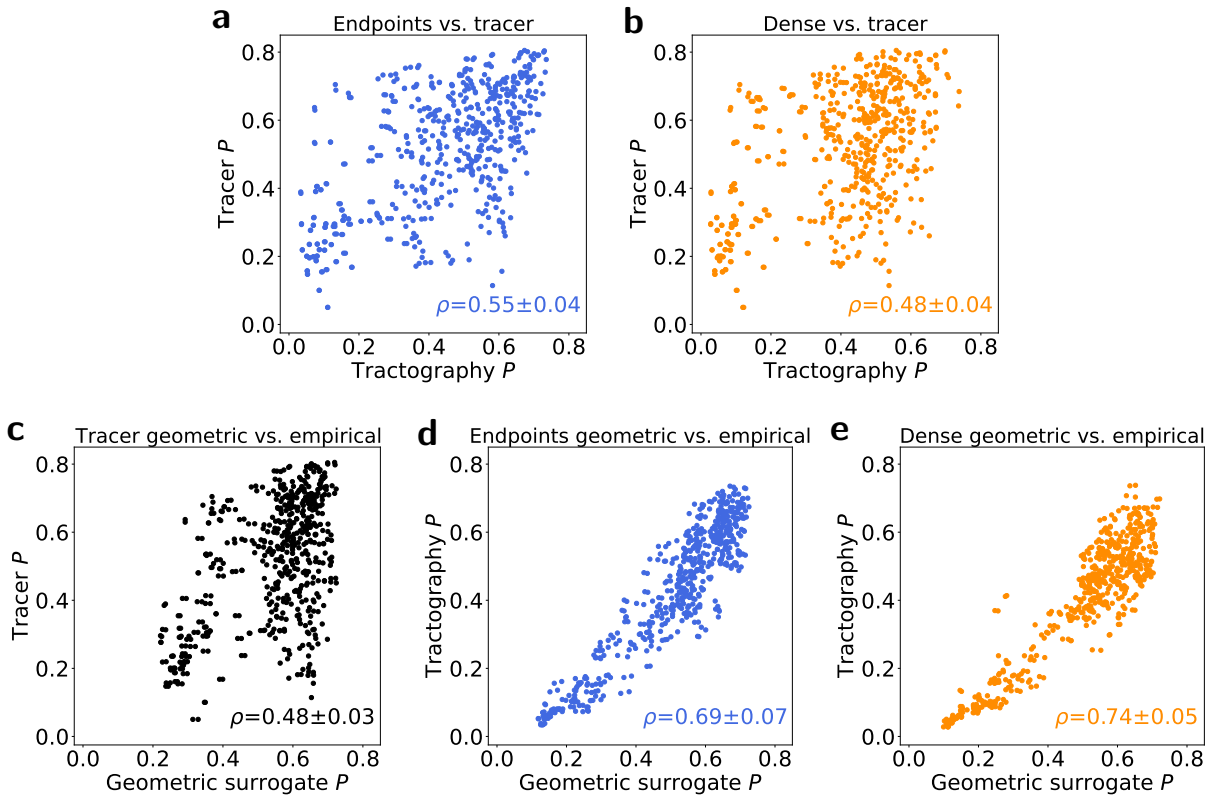

Figure 3.9: Scatterplots showing the relationship between participation coefficients assigned to each node by different network construction methods. (a–b) Correlations between empirical tracer and empirical (a) endpoints and (b) dense tractography participation coefficients. (c–e) Correlations between empirical (c) tracer, (d) endpoint, and (e) dense participation coefficients and those from their corresponding geometric surrogate graphs. Values represent averages across 5 tractography datasets and an ensemble of 100 geometric surrogate graphs.

Previous work with human tractography datasets[108] has revealed that the human brain places its strongest nodes further into geometrically peripheral regions than would be ex-

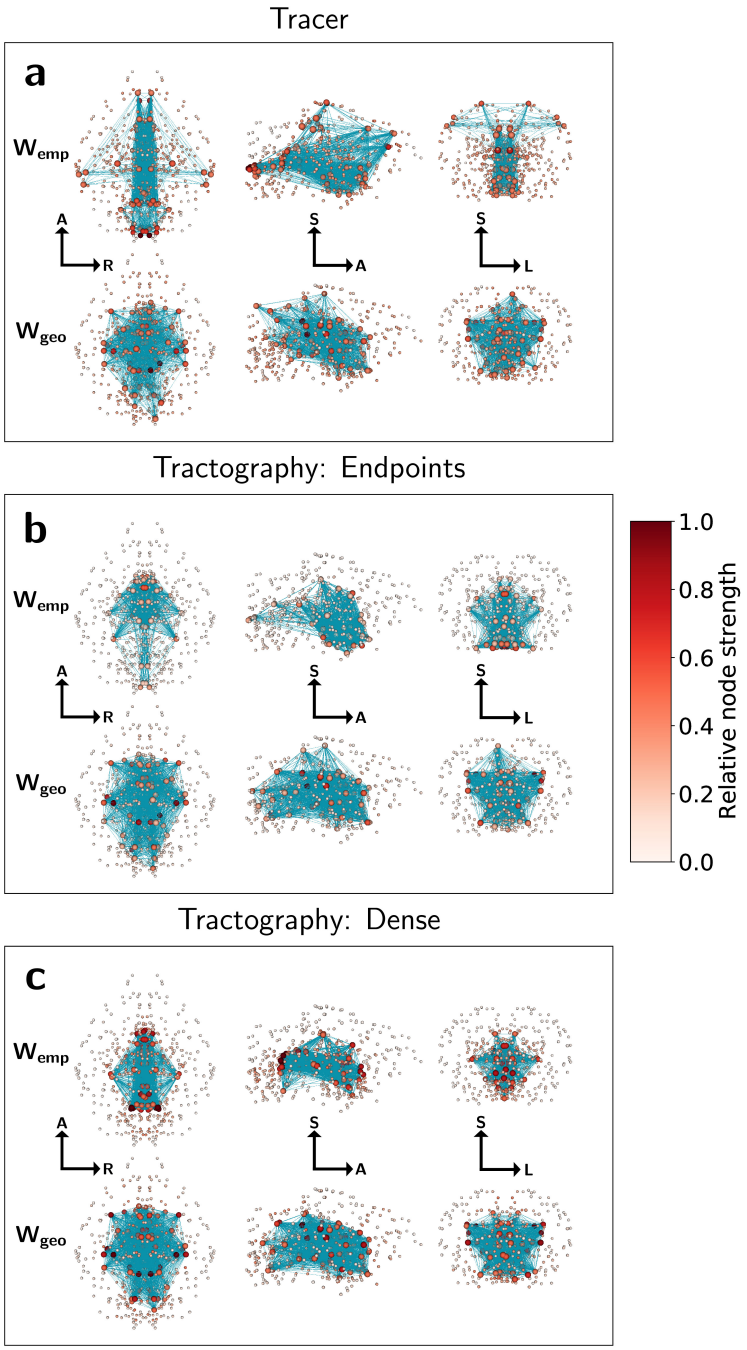

Figure 3.10: Visualization of network structure for (a) tracer, (b) endpoint, and (c) dense graphs in physical coordinates. Spheres represent the center of mass of each node, colored by relative strength. Edges between the top 15% strongest "hub" nodes (larger spheres) are shown as teal lines. Graphs are visualized along the axial (left), sagittal (middle), and coronal (right) planes with labeled orientations: A=anterior, S=superior, R=right, L=left. Tractography node strengths are calculated as averages across 5 datasets. Geometric surrogate graphs are single representative samples.

pected by weight-distance effects alone. In Figure 3.10, we extend this analysis into the mouse brain and compare physical hub organization using node strength as a centrality measure. Hub node locations are visualized in physical coordinates for all empirical and geometric surrogate graphs. Hub nodes are identified as the top 15% of nodes for each graph by node strength and are visualized as large spheres. The remaining bottom 85% of nodes by strength are identified with smaller spheres. Edges between hub nodes are colored teal. For visual clarity, the remaining edges have been omitted.

Region	Tracer	Endpoints	Dense
Hypothalamus	29	57	22
Medulla	19	9	7
Isocortex	17	0	0
Midbrain	10	12	22
Thalamus	9	9	31

Table 3.2: Percent of total hub node strength contained in select major brain divisions.

Through visual comparison of empirical and geometric surrogate tracer graphs, we find the expected result that the mouse brain network as measured with tracer data places its hub nodes further towards the periphery of the brain than would be predicted by geometry alone, with the strongest nodes located across the isocortex, medulla, and inferior hypothalamus. Empirical tractography graphs, however, place the strongest nodes deeper towards the center of the brain compared to the tracer graph, with hubs organized into a ball-like structure comparable to their corresponding geometric surrogates. Table 3.2 shows the percent of total hub node strength located within select major brain divisions for each network construction method. 17% of the total tracer hub strength was located along the isocortex,

while no isocortex nodes in either of the tractography graphs were identified as hubs. Tractography graphs likewise underestimated hub strength in the medulla and overestimated hub strength in the midbrain and thalamus, particularly for the dense node assignment strategy. Overall, only 11 individual structures were co-identified as hubs between the tracer and both tractography methods.

In the case of dense node assignment, the tendency to cluster hub nodes near the center of the brain appears even more pronounced than would be predicted by geometric surrogate graphs with the same weight-distance relationship. These results suggest a strong geometric determination in the organization of hub nodes in tractography above and beyond the geometric relationship expected from tracer data.

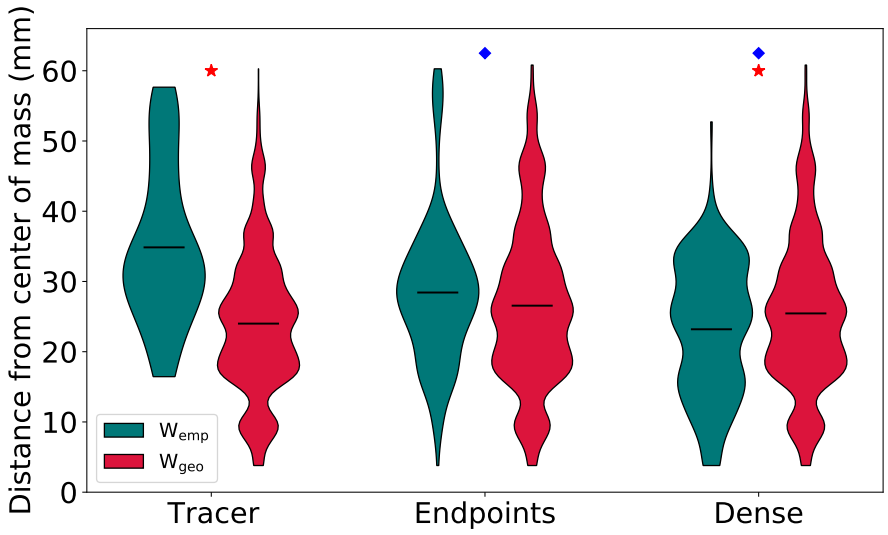

Figure 3.11: Violin plots showing the distribution of distances between the center of mass of individual hub nodes and the center of mass of the brain. Horizontal bars indicate the means of each distribution. Distributions represent per-node values across all datasets. W_{geo} data are taken from an ensemble of 100 random graphs per network construction method. Red stars indicate statistical significance ($p < 0.01$) in the difference between W_{emp} and W_{geo} data, and blue diamonds indicate statistical significance ($p < 0.01$) in the difference between empirical tracer and tractography data. p-values were calculated using Tukey's range test.

The geometric centrality of hub nodes is further quantified in Figure 3.11, which shows the mean distance between hub nodes and the center of mass of the brain for all empirical and

geometric surrogate graphs. As visualized in Figure 3.10, the tracer empirical graph places its hubs further from the center of mass than its corresponding geometric surrogates, while dense tractography not only places its hubs closer to the center of the brain than the tracer graph does, but also places its hubs slightly more central than its own geometric surrogates. Endpoint tractography graphs also place their hub nodes more geometrically central overall than the tracer graph, with distances from the center of mass comparable to their geometric surrogates. However, Figure 3.10 shows that the endpoint graphs are better able than dense graphs to capture some of the more peripheral hubs along the inferior hypothalamus.

In addition to the participation coefficient and node strength, hubs were identified and characterized using their eigenvector centrality (EC), a robust measure of relative node importance calculated by taking the elements of the leading eigenvector of the connectivity matrix[130]. Each node's EC is related to the weight of the connections to its neighbors, such that a node could acquire a high EC either by having a large number of very weak connections or by having a small number of very strong connections. Figure 3.12 shows distributions of the average fiber distance to each node's neighbors $\langle D_{\text{neighbors}} \rangle$ for all empirical and geometric surrogate graphs. Distributions are split into hub (top 15%) and "feeder" (bottom 85%) nodes defined using EC. Nodes with a low $\langle D_{\text{neighbors}} \rangle$ imply physical, geometric centrality with respect to their neighbors, and nodes with a high EC imply high topological centrality and node importance.

Geometric surrogate graphs from all network construction methods have much lower mean $\langle D_{\text{neighbors}} \rangle$ for hub nodes than for feeder nodes, meaning they predict the most topologically central hub nodes to also be the most geometrically central. The empirical tracer graph predicts the opposite relationship: not only are tracer hub nodes located further from their neighbors than predicted by geometry, they are also less geometrically central than the remaining feeder nodes, reflecting their peripheral placement seen in Figures 3.10 and 3.11.

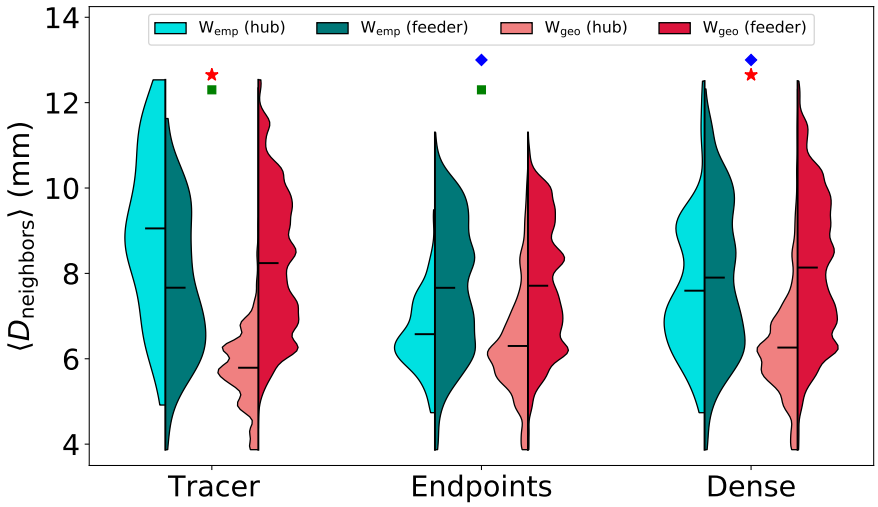

Figure 3.12: Violin plots showing distributions of the average fiber distance to each node's neighbors, split into hub (top 15%) and feeder (bottom 85%) nodes defined using eigenvector centrality. Distributions from empirical graphs are shown in blue colors, and distributions from geometric surrogate graphs are shown in red colors. Lighter shades of each color indicate hub nodes and darker shades indicate feeder nodes. Horizontal bars indicate the means of each distribution. Distributions represent per-node values across all datasets. Green squares indicate statistical significance ($p < 0.01$) in the difference between empirical hub and feeder distributions. Red stars indicate statistical significance ($p < 0.01$) in the difference between W_{emp} and W_{geo} hub values. Blue diamonds indicate statistical significance ($p < 0.01$) in the difference between empirical tracer and tractography hub values. p-values were calculated using Tukey's range test.

This effect is not observed in any of the empirical tractography graphs. The dense tractography graphs predict $\langle D_{\text{neighbors}} \rangle$ values for their hub nodes more similar to those from the tracer graph, but the distributions from both tractography approaches are much more similar to those from their corresponding geometric surrogates than the empirical tracer distributions are to theirs. Particularly, both empirical tractography graphs have lower mean $\langle D_{\text{neighbors}} \rangle$ values for hub nodes than for feeder nodes, the reverse of the relationship seen in the tracer graph. This once again indicates a strong geometric bias in the placement of topologically important nodes in tractography graphs.

3.3.4 Comparison of additional network properties

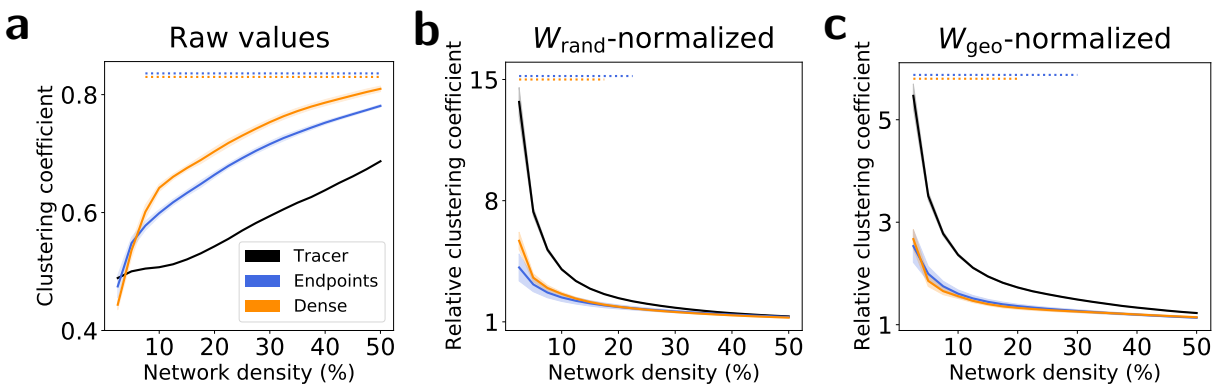

Figure 3.13: Mean binary clustering coefficients for each method as a function of network density. Shaded regions represent 1 standard deviation across 5 tractography datasets and ensembles of 100 geometric and random surrogate graphs. (a) Raw mean clustering coefficient values for all empirical graphs. (b) Mean clustering coefficients for all empirical graphs randomized against the mean value from their corresponding random surrogates. (c) Mean clustering coefficients for all empirical graphs randomized against the mean value from their corresponding geometric surrogates. The widths of the horizontal lines at the top of the figures indicate the range of network densities with statistical significance ($p < 0.01$) in the difference between tracer and tractography values for each tractography method, calculated with (a) Tukey's range test and (b–c) a permutation test.

Binary clustering coefficient

The binary clustering coefficient[94] is calculated as the ratio of all existing to all possible triangles around an individual node. The mean clustering coefficient $\langle C \rangle$ across the whole graph is thus an additional metric of network segregation similar to the modularity (Figure 3.8), indicating the prevalence of densely interconnected clusters around individual nodes. The tracer and tractography graphs used in this study are nearly fully connected. Accordingly, we thresholded the graphs by edge weight and show the $\langle C \rangle$ values as a function of resulting network density in Figure 3.13. Raw values are shown for tracer, endpoint, and dense empirical graphs in Figure 3.13a. While the raw clustering values are higher in tractography than in tracer graphs, the W_{rand}-normalized values in Figure 3.13b show the tracer graphs

with a higher normalized $\langle C \rangle$ at all densities, indicating that the tractography methods underestimate the true clustering of the mouse brain. In Figure 3.13c, empirical $\langle C \rangle$ values have been normalized by the values from their corresponding geometric surrogates. As with modularity, at all network densities, the W_{geo}-normalized values for tractography graphs are much closer to 1 than for the tracer graph, indicating a stronger geometric component of clustering in tractography than in tracer data for all tractography methods.

Comparison of network efficiency

While analysis of modular structure and related metrics describe aspects of network segregation, the global and local efficiencies are metrics of integration for unweighted networks. Local efficiency is calculated as the average inverse shortest path length between a node and all of its neighbors, while global efficiency is the average inverse shortest path length between all pairs of nodes in a network. Accordingly, networks with high global efficiencies are able to efficiently communicate information across different regions. Raw global efficiency values are shown in Figure 3.14a. As the underlying weighted graphs are nearly fully connected for all methods, binary efficiencies are characterized as a function of network density after thresholding low-weight edges. Global efficiencies normalized by the values from W_{rand}- and W_{geo}-surrogate graphs are shown in Figures 3.14b–c, respectively. Across all threshold levels and normalizations, global efficiencies from endpoint tractography provided a good match to those from the tracer model. Dense tractography significantly underestimated global efficiency at all densities, even after normalization with the values from its geometric surrogates, which suggests that dense tractography underestimates the role of geometry in network integration relative to the tracer model. Figure 3.14d–e shows scatterplots demonstrating the relationship of per-node local efficiencies between tractography- and tracer-derived networks across multiple densities. Pearson correlations were weak across both methods and all densities, indicating that while endpoint tractography performs well in estimating global

efficiency, neither tractography method is able to accurately predict the local efficiency of individual nodes.

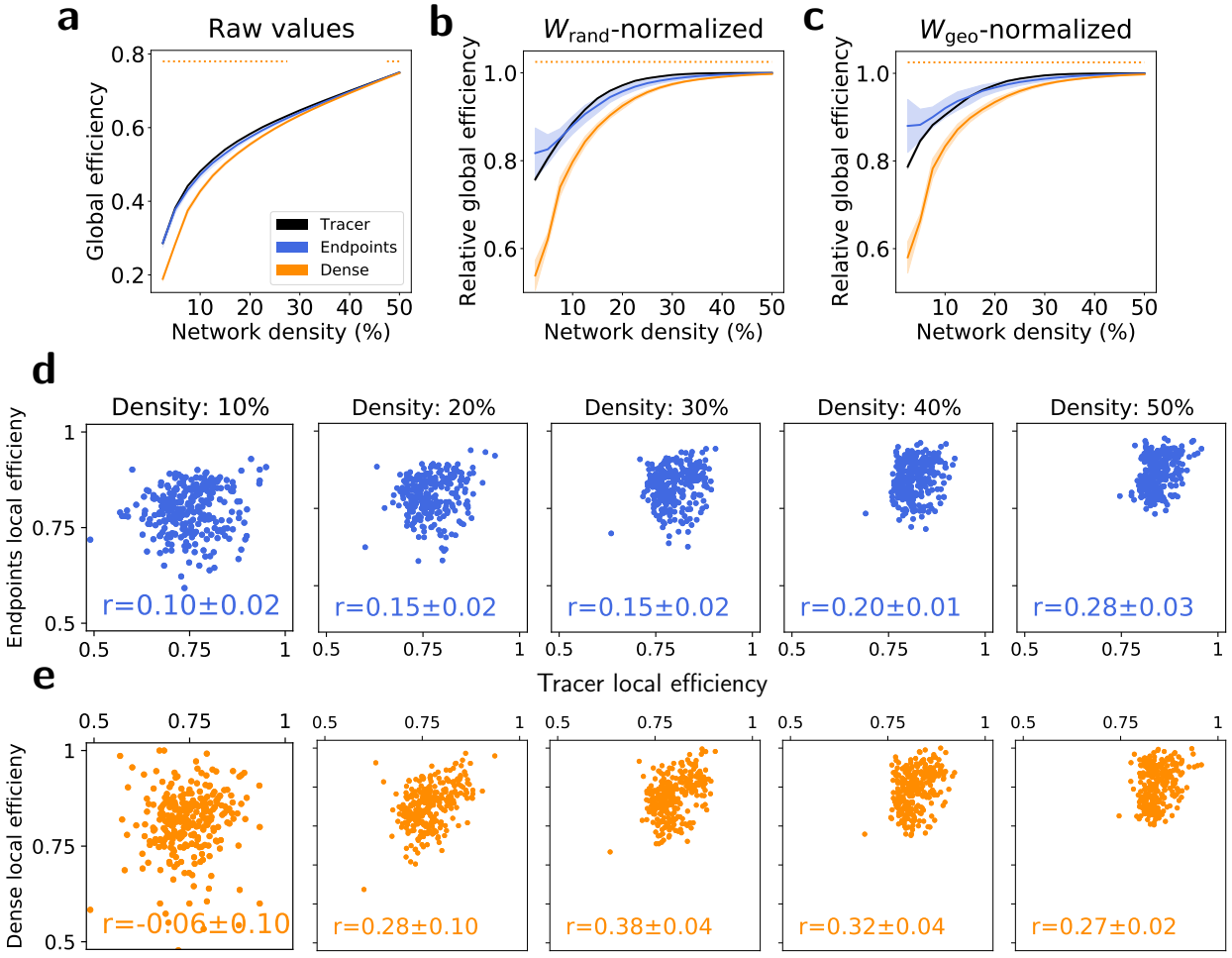

Figure 3.14: Efficiency. (a–c) Global efficiencies for each method as a function of network density. Shaded regions represent 1 standard deviation across 5 tractography datasets. (a) Raw global efficiency values for all empirical graphs. (b) Global efficiencies for all empirical graphs randomized against the mean value from their corresponding random surrogates. (c) Global efficiencies for all empirical graphs randomized against the mean value from their corresponding geometric surrogates. The widths of the horizontal lines at the top of (a–c) indicate the range of network densities with statistical significance ($p < 0.01$) in the difference between tracer and tractography values for each tractography method, calculated with (a) Tukey's range test and (b–c) a permutation test. (d–e) Scatterplots showing local efficiencies calculated with empirical tracer and (d) endpoint and (e) dense tractography graphs across a range of network densities. r values indicate Pearson correlations.

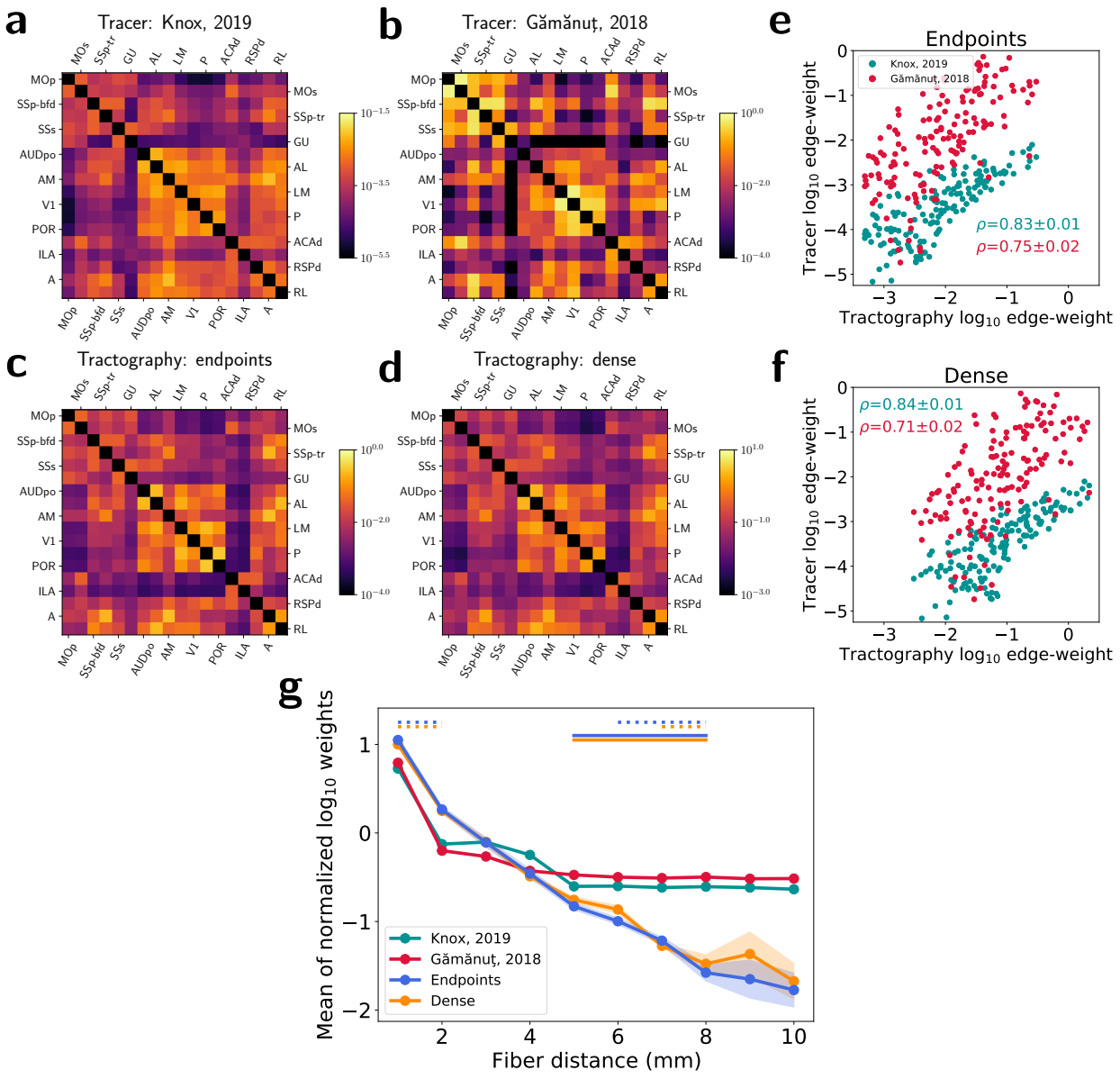

Figure 3.15: Comparison to empirical, retrograde tracer data in the cortex from Gămănuţ, 2018. (a–d) Cortical connectivity matrices for (a) the Knox, 2019 tracer model, (b) the Gămănuţ, 2018 empirical data, (c) endpoint tractography, and (d) dense tractography. (e–f) Scatterplots showing correlations between (e) endpoint and (f) dense tractography edge weights and values from the two tracer graphs. ρ values indicate Spearman correlation coefficients with standard deviations calculated across 5 tractography datasets. (g) Normalized weight-distance relationships. Circles represent the average log-weight z-scores for each method within 1 mm fiber distance bins. Shaded regions represent 1 standard deviation across 5 tractography datasets. The widths of the dotted and solid horizontal lines at the top of the figure indicate the range of fiber distance bins with statistically significant differences ($p < 0.01$) between Knox, 2019 (dotted) and Gămănuţ, 2018 (solid) tracer values and tractography values for each tractography method, calculated using a one-sample t-test after correcting for multiple comparisons.

3.3.5 Validation with independent tracer measurements

For independent validation of the whole-brain network analysis results from the computational tracer model from Knox et al., tractography edge-weights were also compared to ipsilateral cortical connectivity measurements published in Gămănuţ, et al. 2018[124]. Figures 3.15a–d show connectivity matrices of 18 cortical regions from both tracer datasets and tractography methods. Scatterplots between tractography and tracer edge-weights are shown for endpoints and dense tractography in Figures 3.15e–f, respectively. For both node assignment methods, Spearman correlations between tractography and tracer weights are significantly higher with the Knox et al. model than the Gămănuţ et al. data. Figure 3.15g shows the mean relationship between edge weights and fiber distance after the log-weight distributions were normalized to a mean of 0 and standard deviation of 1. Even though the overall range of distances is shorter between ipsilateral cortical nodes than across the whole brain, the tractography methods both still demonstrate a significant underestimation of long-range connectivity relative to empirical tract-tracing measurements in the cortex, which is consistent with the resulting geometric bias in network properties found through comparison to computational tracer-derived connectivity estimates in the whole brain.

3.4 Discussion

Across nearly all metrics explored in this study, we find that the topological properties of tractography-derived graphs are much more influenced by spatial embedding than would be predicted by the more accurate role of spatial embedding represented by the tracer model. Tractography graphs underestimate connectivity weights at long distances, leading to a conflation of topological and geometric centrality that biases the estimated modular structure and the architecture of hub subnetworks. These results serve as an important reminder for consideration in future tractography studies: given that many properties of the true brain network can be reasonably predicted strictly by spatial embedding, tractography methods

development and validation efforts should be targeted towards the ability to predict network properties *beyond* a geometric baseline. While we expect that methodological geometric bias plays a similar role in human tractography networks, some studies have shown encouraging results. For example, Roberts et al.[108] demonstrated that empirical human tractography graphs exhibit a more peripheral hub network structure than predicted by their corresponding geometric surrogate graphs, similar to our tracer results in Figure 3.10 and in contrast to what we observed with tractography networks. Nevertheless, conclusions from human tractography networks cannot be verified with additional ground-truth imaging, and caution should be taken when interpreting tractography-derived brain networks in all species, particularly for metrics which rely more on long-range connections.

One aim of this chapter was to explore differences in tractography network structure resulting from the streamline node-assignment strategy. Ultimately, we found our results were largely independent of the specific node-assignment approach. The geometric bias in tractography was not mitigated by either method; despite small differences, network characteristics of both tractography graphs were far more similar to each other than either of them were to characteristics of the tracer graph. While endpoint tractography might represent a more physically intuitive model of brain connectivity, the comparable performance of dense tractography reflects the ambiguous physical definition of tractography streamlines. Particularly at this spatial resolution and in the absence of stronger anatomical regularization, tractography streamlines strictly represent potential probabilistic pathways of white matter fibers that are consistent with symmetric diffusion data. When streamlines are made to terminate under reasonably enforced constraints such as on fODF magnitude or streamline curvature, this enforces a penalty on unrealistic fiber geometries or the use of lower-confidence diffusion data, but does not yield a physical sense of the actual origin or termination points of the underlying neuronal fibers. This compromises the intuitive appeal of "endpoint" streamline node assignment as used in this study. In fact, without additional constraints, we expect

the endpoint locations of any given streamline to be more noisy and erroneous as streamline length increases due to the fiber orientation errors accumulated at each step in the tracking process, an inherent tradeoff that exists even with more sophisticated forms of anatomic regularization. With dense tractography, the effective signal-to-noise ratio for connectivity similarly falls off for points further away from the seed location, but since a single streamline is allowed to contribute to the connectivity estimate between multiple node-pairs at varying distances, a greater proportion of points from each streamline contribute connectivity estimates that are less noisy than those from the endpoints. Dense tractography also serves as a potentially more physically meaningful match to the tracer data used in this study, as connectivity values in the Knox et al. model are derived from segmented projection volumes of a viral tracer that fluoresces along the entire length of any given neural projection.

For the data used in this study, we took the approach of seeding only from the gray matter to avoid known tract-length connectivity biases[19,132], and normalized the streamline counts by the volumes of each node-pair in order to better match the normalized connection density metric used in the Knox et al. model. Since our data were acquired with a single, relatively low b-value, we opted against the use of more advanced streamline quantitation algorithms such as SIFT2[26]. This also provides a more direct comparison between our results and those of similar studies that have used the Allen tracer data to benchmark tractography performance without reference to the role of spatial embedding[53,104,118]. Even with these relatively simple post-processing approaches, the results of this study serve to echo recent tractography validation reviews that suggest that the future of tractography connectomics hinges on the incorporation of more advanced anatomical and microstructural priors to tractography pipelines in order to address geometric and other biases and make streamlines more quantitative and physically meaningful[101,103]. Network analysis with geometric surrogate graphs can be an important tool to evaluate such quantitative tractography pipelines in the future. A recent study by Girard et al.[115] rigorously benchmarked 15 tractography algo-

rithms and a number of regularization approaches such as the "anatomically constrained tractography" framework[24] and the SIFT2 post-processing algorithm[26] against tracer data in the macaque cortex, though it did not present analysis of downstream network measures. Our future work will similarly explore the adoption of more advanced tractography and regularization approaches in the mouse brain, where whole-brain tracer data are more readily available. Benchmarking these approaches with the use of geometric surrogate graphs will allow for a deeper understanding of the value of existing quantitative strategies designed to mitigate tractography biases.

The results in this study rely on the assumption of the tracer data as a ground truth representation of the underlying mesoscale mouse brain network architecture. While tracer data is certainly ideal in many respects for the benchmarking of diffusion tractography, there are also limitations to this assumption. Both anterograde and retrograde tracer studies produce inherently directed graphs, whereas tractography is based on inherently symmetric diffusion measurements and produces undirected graphs. This requires the use of directional symmetry enforcement for fair comparison that may alter the underlying network properties represented by the tracer data. Besides any biases in the imaging and registration process itself, the Knox et al. model relies on computational estimates of connectivity based on segmented volume fractions of underlying tracer experiments that may span multiple different gray-matter regions. Accordingly, the Knox et al. model itself is only an estimate that may carry its own biases of the true underlying density of neurons connecting each region pair. For this reason, we are encouraged by the validation of our tractography results against the more empirical measurements of neuronal connectivity from the retrograde tract-tracing experiments published by Gămănuţ et al. (Figure 3.15). Correlations between tractography and tracer edge-weights are even lower for the Gămănuţ et al. data than for the Knox et al. model, while tractography shows a comparably dramatic falloff in weight with distance relative to both tracer datasets, suggesting that our overall conclusion that tractography

graphs are more determined by geometry than tracer graphs would persist if empirical measurements similar to those from the Gămănuţ et al. study were available across the whole brain.

3.5 Appendix: Graph theory

Graph theory is a powerful branch of mathematics concerned with modeling and quantifying topological characteristics of network systems[92]. Its core structure is the *graph* which is used to model pairwise relationships between objects. Graphs are comprised of *nodes* connected by *edges*. These edges represent connections between nodes and can be either *directed* or *undirected*. The cellular-level structural connectome as well as its mesoscale representation in the AMBCA tracer data are examples of directed graphs, where nodes are defined by individual neurons or structural brain regions, and edges represent the synapses connecting them. These connections are not necessarily symmetric due to the directed nature of neurons themselves. Brain graphs constructed from tractography are examples of undirected graphs. Since tractography is based on a fundamentally symmetric diffusion measurement, connections between nodes represent bidirectional probabilistic pathways. Edges between nodes can also be *binary* or *weighted*. Weights in the brain graphs in this chapter are defined for each modality such that higher weights correspond to a greater degree of connectivity between two nodes.

3.6 Appendix: Tractography parameter selection

Numerous studies have explored the variability of tractography performance with respect to parameters such as curvature, fODF cutoff, and step size[50,51,104,118]. Tractography parameters were chosen for this study based on a subset of the whole tracer connectivity matrix from the AMBCA. Eight tracer experiments were chosen such that projections from the

corresponding injection regions reached all target regions used in the full connectivity analysis. The injection masks were used to seed probabilistic tractography over a grid search of parameters given in Table 3.3. Tracking was done with dMRI data registered to the Allen reference space, as discussed in sections 3.2.5–3.2.6. With 5 datasets, 8 injection regions, 5 fODF cutoff values, 2 step sizes, and 2 curvature values, this resulted in a total of 800 tractography experiments. Connectivity matrices were then constructed from each group of tractography experiments using both "endpoint" and "dense" connectivity definitions, as discussed in section 3.2.6.

fODF cutoff	0.02	0.0375	0.055	0.0725	0.09
Step size [μm]	12.5	25			
Curvature [μm]	18	30			
Algorithm	iFOD2				
Number of streamlines	500,000				
Minimum streamline length	0.5 mm				
Maximum streamline length	30 mm				

Table 3.3: Tractography parameters.

Receiver operating characteristic (ROC) analysis was performed on the connectivity matrices constructed from all parameter combinations, using values from the Allen mesoscale connectome[112] as ground truth. To construct the curves, the streamline count threshold used to define a positive connection in the tractography matrices was swept at 150 logarithmically spaced values from the minimum to the maximum value in each matrix, and the true positive fraction and false positive fraction were calculated for each threshold. The area under the ROC curve (AUC) was then determined by numerically integrating under each ROC curve. Distributions of AUC values for each parameter combination are shown in Figure 3.16. From these results, remaining tractography was performed using an fODF

cutoff of 0.055, a step size of 12.5 µm, and a maximum curvature of 30 µm.

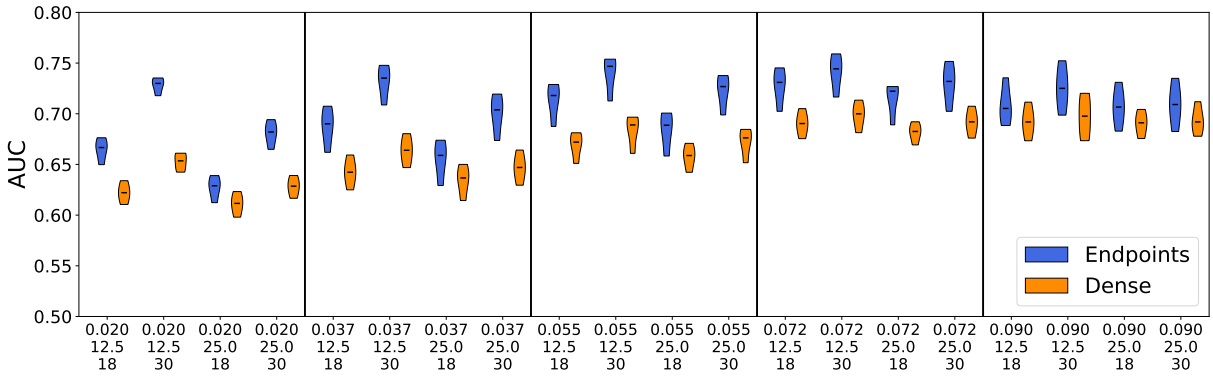

Figure 3.16: Tractography parameter selection distributions. Values along the x-axis correspond to fODF cutoff, step size [µm], and curvature [µm], respectively.

3.7 Appendix: Parcellation structure information

Table 3.4: Parcellation structure information from the Allen Mouse Brain Atlas.

Abbreviation	Allen structure ID	Major brain division
FRP	184	Isocortex
MOp	985	Isocortex
MOs	993	Isocortex
SSp-n	353	Isocortex
SSp-bfd	329	Isocortex
SSp-ll	337	Isocortex
SSp-m	345	Isocortex
SSp-ul	369	Isocortex
SSp-tr	361	Isocortex
SSp-un	182305689	Isocortex
SSs	378	Isocortex
GU	1057	Isocortex
VISC	677	Isocortex
AUDd	1011	Isocortex

Continued on next page

Table 3.4, continued

Abbreviation	Allen structure ID	Major brain division
AUDp	1002	Isocortex
AUDpo	1027	Isocortex
AUDv	1018	Isocortex
VISal	402	Isocortex
VISam	394	Isocortex
VISl	409	Isocortex
VISp	385	Isocortex
VISpl	425	Isocortex
VISpm	533	Isocortex
VISli	312782574	Isocortex
VISpor	312782628	Isocortex
ACAd	39	Isocortex
ACAv	48	Isocortex
PL	972	Isocortex
ILA	44	Isocortex
ORBl	723	Isocortex
ORBm	731	Isocortex
ORBvl	746	Isocortex
AId	104	Isocortex
AIp	111	Isocortex
AIv	119	Isocortex
RSPagl	894	Isocortex
RSPd	879	Isocortex
RSPv	886	Isocortex
VISa	312782546	Isocortex
VISrl	417	Isocortex
TEa	541	Isocortex
PERI	922	Isocortex
ECT	895	Isocortex

Continued on next page

Table 3.4, continued

Abbreviation	Allen structure ID	Major brain division
MOB	507	OLF
AOB	151	OLF
AON	159	OLF
TT	589	OLF
DP	814	OLF
PIR	961	OLF
NLOT	619	OLF
COAa	639	OLF
COAp	647	OLF
PAA	788	OLF
TR	566	OLF
CA1	382	HPF
CA2	423	HPF
CA3	463	HPF
DG	726	HPF
FC	982	HPF
IG	19	HPF
ENTl	918	HPF
ENTm	926	HPF
PAR	843	HPF
POST	1037	HPF
PRE	1084	HPF
SUB	502	HPF
CLA	583	CTXsp
EPd	952	CTXsp
EPv	966	CTXsp
LA	131	CTXsp
BLA	295	CTXsp
BMA	319	CTXsp

Continued on next page

Table 3.4, continued

Abbreviation	Allen structure ID	Major brain division
PA	780	CTXsp
CP	672	STR
ACB	56	STR
FS	998	STR
OT	754	STR
LSc	250	STR
LSr	258	STR
LSv	266	STR
SF	310	STR
SH	333	STR
AAA	23	STR
BA	292	STR
CEA	536	STR
IA	1105	STR
MEA	403	STR
GPe	1022	PAL
GPi	1031	PAL
SI	342	PAL
MA	298	PAL
MS	564	PAL
NDB	596	PAL
TRS	581	PAL
BST	351	PAL
BAC	287	PAL
VAL	629	TH
VM	685	TH
VPL	718	TH
VPLpc	725	TH
VPM	733	TH

Continued on next page

Table 3.4, continued

Abbreviation	Allen structure ID	Major brain division
VPMpc	741	TH
SPFm	414	TH
SPFp	422	TH
SPA	609	TH
PP	1044	TH
MG	475	TH
LGd	170	TH
LP	218	TH
PO	1020	TH
POL	1029	TH
SGN	325	TH
AV	255	TH
AM	127	TH
AD	64	TH
IAM	1120	TH
IAD	1113	TH
LD	155	TH
IMD	59	TH
MD	362	TH
SMT	366	TH
PR	1077	TH
PVT	149	TH
PT	15	TH
RE	181	TH
RH	189	TH
CM	599	TH
PCN	907	TH
CL	575	TH
PF	930	TH

Continued on next page

Table 3.4, continued

Abbreviation	Allen structure ID	Major brain division
RT	262	TH
IGL	27	TH
LGv	178	TH
SubG	321	TH
MH	483	TH
LH	186	TH
SO	390	HY
ASO	332	HY
PVH	38	HY
PVa	30	HY
PVi	118	HY
ARH	223	HY
ADP	72	HY
AVP	263	HY
AVPV	272	HY
DMH	830	HY
MEPO	452	HY
MPO	523	HY
PD	914	HY
PS	1109	HY
PVp	126	HY
PVpo	133	HY
SBPV	347	HY
SCH	286	HY
SFO	338	HY
VLPO	689	HY
AHN	88	HY
LM	210	HY
MM	491	HY

Continued on next page

Table 3.4, continued

Abbreviation	Allen structure ID	Major brain division
SUM	525	HY
TMd	1126	HY
TMv	1	HY
MPN	515	HY
PMd	980	HY
PMv	1004	HY
PVHd	63	HY
VMH	693	HY
PH	946	HY
LHA	194	HY
LPO	226	HY
PST	356	HY
PSTN	364	HY
RCH	173	HY
STN	470	HY
TU	614	HY
ZI	797	HY
SCs	302	MB
IC	4	MB
NB	580	MB
SAG	271	MB
PBG	874	MB
MEV	460	MB
SNr	381	MB
VTA	749	MB
RR	246	MB
MRN	128	MB
SCm	294	MB
PAG	795	MB

Continued on next page

Table 3.4, continued

Abbreviation	Allen structure ID	Major brain division
APN	215	MB
MPT	531	MB
NOT	628	MB
NPC	634	MB
OP	706	MB
PPT	1061	MB
CUN	616	MB
RN	214	MB
III	35	MB
IV	115	MB
VTN	757	MB
AT	231	MB
LT	66	MB
SNc	374	MB
PPN	1052	MB
IF	12	MB
IPN	100	MB
RL	197	MB
CLI	591	MB
DR	872	MB
NLL	612	P
PSV	7	P
PB	867	P
SOC	398	P
B	280	P
DTN	880	P
PCG	898	P
PG	931	P
PRNc	1093	P

Continued on next page

Table 3.4, continued

Abbreviation	Allen structure ID	Major brain division
SG	318	P
SUT	534	P
TRN	574	P
V	621	P
CS	679	P
LC	147	P
LDT	162	P
NI	604	P
PRNr	146	P
RPO	238	P
SLC	350	P
SLD	358	P
AP	207	MY
DCO	96	MY
VCO	101	MY
CU	711	MY
GR	1039	MY
ECU	903	MY
NTB	642	MY
NTS	651	MY
SPVC	429	MY
SPVI	437	MY
SPVO	445	MY
VI	653	MY
VII	661	MY
ACVII	576	MY
AMB	135	MY
DMX	839	MY
GRN	1048	MY

Continued on next page

Table 3.4, continued

Abbreviation	Allen structure ID	Major brain division
ICB	372	MY
IO	83	MY
IRN	136	MY
ISN	106	MY
LIN	203	MY
LRN	235	MY
MARN	307	MY
MDRNd	1098	MY
MDRNv	1107	MY
PARN	852	MY
PAS	859	MY
PGRNd	970	MY
PGRNl	978	MY
NR	177	MY
PRP	169	MY
PPY	1069	MY
LAV	209	MY
MV	202	MY
SPIV	225	MY
SUV	217	MY
x	765	MY
XII	773	MY
y	781	MY
LING	912	CB
CENT	920	CB
CUL	928	CB
DEC	936	CB
FOTU	944	CB
PYR	951	CB

Continued on next page

Table 3.4, continued

Abbreviation	Allen structure ID	Major brain division
UVU	957	CB
NOD	968	CB
SIM	1007	CB
AN	1017	CB
PRM	1025	CB
COPY	1033	CB
PFL	1041	CB
FL	1049	CB
FN	989	CB
IP	91	CB
DN	846	CB

CHAPTER 4

IDENTIFICATION OF SPECTRAL BIASES IN BIOPHYSICAL EPSI WHITE-MATTER MODELS WITH DMRI

4.1 Introduction

Myelin is a lipid-rich substance produced by oligodendrocytes in the central nervous system that physically surrounds axons in order to improve the transmission of action potentials[133]. Its importance to the normal function of the human brain has been demonstrated through the symptoms of demyelination disorders such as multiple sclerosis, as well as through additional disorders related to defective myelin structure such as hypomyelination, dysmyelination, and myelinolysis[134].

Conventional clinical MRI approaches to the diagnosis of myelin disorders use combinations of T_1-weighted, T_2-weighted, and FLAIR acquisitions and have been shown to have poor specificity to myelin[135–137], prompting the development of approaches such as myelin water imaging[138,139], which uses a multi-echo spin-echo sequence to estimate a myelin component within the T_2 distribution. Recently, the use of a multi-gradient echo (MGE) sequence, also referred to as echo-planar spectroscopic imaging (EPSI), has emerged as an alternative to myelin water imaging[65,66,125,140–144]. EPSI measures a portion of the voxel-wise T_2^* decay curve, and results in faster scan times, a larger volume coverage, and a lower specific absorption rate than the sequences used for myelin water imaging[145]. To estimate myelin content and integrity from the EPSI signal, the free induction decay (FID) curves are fit to a biophysical model that typically assumes the white matter is composed of three distinct, nonexchanging water components: myelin water, intra-axonal water, and extracellular water, each with distinct T_2^* values and potential magnetic susceptibility-dependent frequency shifts[140,143–146].

Previous work[66] has shown that a simple metric quantifying asymmetric broadening

of the water resonance line-shape from the fully-sampled FID is sensitive to the presence of white matter as well as to the angle between the principal orientation of the constituent fibers and the main magnetic field (B_0). An additional study performed further spectral asymmetry analysis through a comparison of data from both control and mutant "*shiverer*" (Mbp^{Shi}) postmortem, fixed mouse brains[125]. Shiverer mice serve as a dysmyelination model due to a mutation that leads to the production of abnormal, thin, loosely-packed myelin sheaths[147]. The study found measurable differences in spectral asymmetric broadening between control and shiverer mice, leading to the hypothesis that myelin is a likely contributing source of the sensitivity of the spectral asymmetry to white matter.

In this chapter, we extend the analysis of water spectra from control and shiverer mouse brains to explore the performance of two biophysical compartmental models published by Van Gelderen et al.[146] and Nam et al.[143]. We quantify the asymmetric broadening predicted after fitting the data to these models and compare it to the broadening measured directly in the data itself to show that both models fail to recover important spectral features in the data.

4.1.1 Author contributions

This chapter is currently under review as a manuscript in *Magnetic Resonance in Medicine* under the title "Model-free analysis in the spectral domain of postmortem mouse brain EPSI reveals inconsistencies with model-based analyses of the free induction decay" with co-authors Gregg Wildenberg, Narayanan Kasthuri, Patrick La Rivière, and Sean Foxley. The author was responsible for all analysis, figures, and text in the chapter, while the co-authors were responsible for the conception and supervision of the project, sample preparation, data acquisition, and manuscript review.

4.2 Methods

4.2.1 Sample preparation

Procedures for the collection of the EPSI and diffusion MRI data used for this study have been published in a previous study[125] and are repeated here for completeness. All procedures performed on animals followed protocols approved by the Institutional Animal Care and Use Committee and were in compliance with the Animal Welfare Act and the National Institutes of Health Guide for the Care and Use of Laboratory Animals. Adult mice were deeply anesthetized with 60 mg/kg pentobarbital and sacrificed by intercardial perfusion with a solution (pH 7.4) of 0.1 M sodium cacodylate and heparin (15 units/ml). This was immediately followed by a solution of 2% paraformaldehyde, 2.5% glutaraldehyde, and 0.1 M sodium cacodylate (pH 7.4). Brains were carefully removed from the skulls and post-fixed in the same fixative overnight at 4°C. Brains were soaked in phosphate buffered saline (PBS) prior to imaging for at least 72 hours to remove fixative from the tissue.

4.2.2 MR imaging

Resected control ($n = 5$) and shiverer ($n = 4$) mouse brains were dried of excess PBS and placed in 10 ml Falcon tubes. Tubes were filled with Fluorinert (FC-3283, 3M Electronics) for susceptibility matching and to improve shimming.

Data were acquired at 9.4 T (20 cm internal diameter, horizontal bore, Bruker BioSpec Small Animal MR System, Bruker Biospin, Billerica, MA) using a 6 cm high performance gradient insert (maximum gradient strength: 1000 mT/m, Bruker Biospin) and a 35 mm internal diameter quadrature volume coil (Rapid MR International, Columbus, Ohio). Brains were aligned such that the anterior/posterior portion of the olfactory limb of the anterior commissure was approximately parallel to B_0 and the hemispheric midline was parallel to the scanner YZ plane. This ensured consistency of position relative to B_0 across samples.

Third-order shimming was iteratively performed over an ellipse that encompassed the entire brain, but did not extend beyond the boundaries of the Falcon tube/Fluorinert interface, using the Paravision mapshim protocol. B_0 maps were produced by recording the voxel-wise frequency of the peak of the resonance, including additional sub-spectral resolution frequency produced by estimating the maximum peak amplitude of the resonance, described below. This was consistent with previously reported work[65,66] which described a high degree of field homogeneity across samples.

Diffusion MRI (dMRI) was performed using a conventional 3D spin-echo/Stejskal-Tanner diffusion-weighted sequence (TR = 600 ms, TE = 11.389 ms, b-value = 3000 s/mm^2, δ = 3.09 ms, Δ = 6 ms, spatial resolution = 125 µm isotropic, number of b0s = 8, number of directions = 30, receiver bandwidth = 150 kHz, duration = 36h 28min 48s).

3D-EPSI data were acquired using a MGE sequence with an oscillating readout gradient train. Note that while the terms MGE and EPSI are synonymous, in the context of this paper, we will refer to MGE for data analysis in the temporal domain and EPSI for data analysis in the frequency domain. Sequence parameters were chosen so that the entire voxel-wise free induction decay was sampled to the noise floor with sufficiently high temporal resolution to ensure a large spectral bandwidth of ± 360 Hz around the main water peak. This ensured that resultant spectra did not have FID truncation-related ringing artifacts, and that they had sufficient bandwidth, respectively (TR = 1000 ms, TE of first echo = 2.74 ms, echo spacing = 2.74 ms, number of echoes = 192, receiver bandwidth = 75 kHz, flip angle = 68°, 100 µm isotropic resolution, four averages, duration = 12 h). The average signal to noise ratio (SNR) is shown as a function of TE in Figure 4.1. It is worth noting that scan times using this approach can be made more clinically relevant by acquiring 2D data with more modest spatial resolution and covering more targeted slabs of tissue. Previous work has shown in vivo human brain imaging performed with acquisition times on the order of 90 s with 1.5 × 1.5 × 4 mm^3 voxels over five slices[148,149].

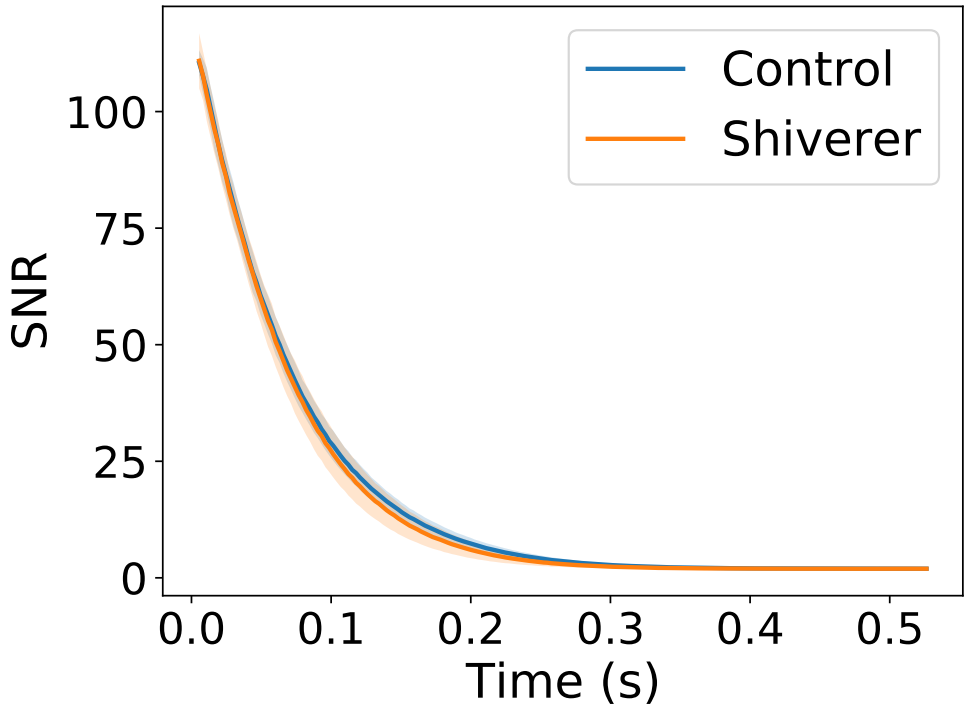

Figure 4.1: SNR as a function of echo time. SNR was measured by taking the ratio of the average in-brain signal volume and the standard deviation of a rectangular patch of background voxels at each TE. Lines represents averages across datasets and the shaded region represents ± 1 standard deviation.

4.2.3 EPSI data processing

The following EPSI data processing and data analysis steps have also been reported elsewhere[66,125] but are summarized here for completeness. Modifications reflecting differences in this work have been made.

EPSI data were processed and analyzed with IDL (ITT Visual Information Solutions, Boulder CO), Matlab (The MathWorks Inc., Natick, MA, 2012), and FSL (FMRIB Software Library, FMRIB, Oxford, UK). 3D multiple-gradient echo data were processed to produce voxel-wise water spectra. Each 4D complex array ($k_x \times k_y \times k_z \times t$) was Fourier transformed in all dimensions to produce three spatial dimensions and one spectral dimension ($x \times y \times z \times \nu$). For the complex spectrum, ν, spectral ghosting was corrected at each point in space (x, y,

z)[150]. The maximum peak magnitude was estimated in each voxel by applying the Fourier shift theorem to the complex data; the addition of a linear phase term in the temporal domain performs sub-spectral resolution shifts in the frequency domain allowing for the identification of the maximum signal magnitude for voxels in which the peak was located between Fourier components[151]. This process was alternately iterated with a zeroth-order phase correction to produce pure absorption spectra[152].

Water peak height (PH) images were constructed with image contrast produced by the maximum voxel-wise signal amplitude of the water spectrum[153]. This can be achieved by shifting the position of the maximum peak amplitude of the water resonance to the central Fourier component of the frequency axis. This step also serves to eliminate any relative background field information from each spectrum with little computational effort; this is analogous to implementing a background field removal technique, such as the PDF[154] or the SHARP[155] filter, to T_2^*-weighted gradient echo data processed in the temporal domain.

The EPSI datasets contained a number of regions with signal drop-out resulting from the magnetic susceptibility mismatch between the tissue and bubbles stuck to the surface of the brain or trapped in the ventricles. To exclude these regions from downstream analysis, artifact masks were constructed for each dataset using the `Atropos` tissue segmentation algorithm in the ANTs[85] software package on the water peak-height images. First, brain masks were automatically generated using the `bet` protocol in FSL[156]. The algorithm was then initialized with a three-class K-means classification of the water peak-height images, with the classes representing white matter, gray matter, and joint CSF/artifact. Voxels in the CSF/artifact class were excluded from all further analysis. A sample image showing tissue classification and artifact filtering is shown in Figure 4.2.

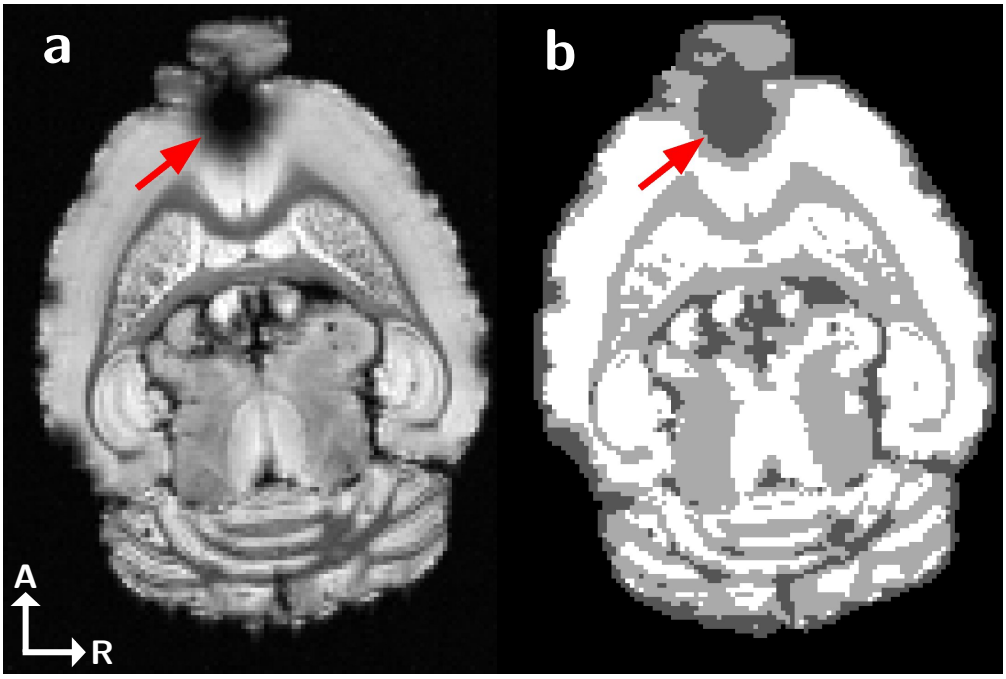

Figure 4.2: Demonstration of `Atropos` tissue segmentation results. Voxels in the CSF/susceptibility artifact class (dark gray, indicated by red arrow) were excluded from all analysis. A–R axis labels correspond to the Anterior and Right directions, respectively.

4.2.4 Model fitting

Myelin imaging with MGE data has typically relied on the use of a three-compartment model for white matter, with separate T_2^* and frequency shifts stemming from axonal water, extracellular water, and myelin water. At its simplest, the time-dependent magnitude $|S_i(t)|$ of the MGE signal at voxel i is modeled as a sum of exponentials for each compartment [140,145]:

$$|S_i(t)| = A_{\text{my}} e^{-t/T^*_{2,\text{my}}} + A_{\text{ax}} e^{-t/T^*_{2,\text{ax}}} + A_{\text{ex}} e^{-t/T^*_{2,\text{ex}}}, \tag{4.1}$$

where A_{my}, A_{ax}, and A_{ex} refer to the amplitudes of the myelin, axonal, and extracellular compartments in voxel i, respectively.

In Van Gelderen et al.[146], the model was modified to include two frequency offsets for myelin ($\Delta f_{\text{my}-\text{ex}}$) and axonal ($\Delta f_{\text{ax}-\text{ex}}$) water relative to extracellular water. This model

was also fit to magnitude data:

$$|S_i(t)| = \left| A_{\text{my}} e^{-(1/T^*_{2,\text{my}} + i2\pi\Delta f_{\text{my-ex}})t} + A_{\text{ax}} e^{-(1/T^*_{2,\text{ax}} + i2\pi\Delta f_{\text{ax-ex}})t} + A_{\text{ex}} e^{-(1/T^*_{2,\text{ex}})t} \right|. \tag{4.2}$$

In Nam et al.[143], the model was fit to the full complex data and further extended to include frequency offset terms for all three compartments with respect to the background as well as a background phase term ϕ_0:

$$\begin{aligned} S_i(t) = \Big[A_{\text{my}} e^{-(1/T^*_{2,\text{my}} + i2\pi\Delta f_{\text{my+bg}})t} &+ A_{\text{ax}} e^{-(1/T^*_{2,\text{ax}} + i2\pi\Delta f_{\text{ax+bg}})t} \\ &+ A_{\text{ex}} e^{-(1/T^*_{2,\text{ex}} + i2\pi\Delta f_{\text{ex+bg}})t} \Big] e^{-i\phi_0}. \end{aligned} \tag{4.3}$$

Our analysis focused on these final two models, which for simplicity we will refer to as the "magnitude fit" (Eqn. 4.2) and "complex fit" (Eqn. 4.3). Note that though Eqn. 4.2 is fit to magnitude data, it still represents a complex model with frequency shifts that produce asymmetric broadening of the water spectrum.

Table 4.1: Replicated from Table 1 in Nam et al.[143] Initial values and search ranges of the parameters for the magnitude-fit and complex-fit models. $S_1 = S(\text{TE}_1)$. $\Delta f_{\text{bg,init}} = \angle \frac{\left\{\sum_{n=1}^{N-1} S_n^* S_{n+1}\right\}}{2\pi\Delta\text{TE}}$: initial Δf_{bg} (N = number of echoes used in fitting).

	Both models					
	A_{my}	A_{ax}	A_{ex}	$T^*_{2,\text{my}}$ (ms)	$T^*_{2,\text{ax}}$ (ms)	$T^*_{2,\text{ex}}$ (ms)
Initial value	$0.1 \times \lvert S_1 \rvert$	$0.6 \times \lvert S_1 \rvert$	$0.3 \times \lvert S_1 \rvert$	10	64	48
Lower bound	0	0	0	3	25	25
Upper bound	$2 \times \lvert S_1 \rvert$	$2 \times \lvert S_1 \rvert$	$2 \times \lvert S_1 \rvert$	25	150	150
	Magnitude fit		Complex fit			
	$\Delta f_{\text{my-ex}}$ (Hz)	$\Delta f_{\text{ax-ex}}$ (Hz)	$\Delta f_{\text{my+bg}}$ (Hz)	$\Delta f_{\text{ax+bg}}$ (Hz)	$\Delta f_{\text{ex+bg}}$ (Hz)	ϕ_0 (rad)
Initial value	5	0	$\Delta f_{\text{bg,init}}$	$\Delta f_{\text{bg,init}}$	$\Delta f_{\text{bg,init}}$	$\angle S_1$
Lower bound	-75	-25	$\Delta f_{\text{bg,init}} - 75$	$\Delta f_{\text{bg,init}} - 25$	$\Delta f_{\text{bg,init}} - 25$	$-\pi$
Upper bound	75	25	$\Delta f_{\text{bg,init}} + 75$	$\Delta f_{\text{bg,init}} + 25$	$\Delta f_{\text{bg,init}} + 25$	π

Model fitting was performed by first converting the preprocessed EPSI spectral data into the temporal domain using an inverse fast Fourier transform. The two models were then fit to the resulting voxel-wise FIDs in Python using a non-linear least-squares approach implemented with the `curve_fit` function in the SciPy package. Optimization parameters for the fitting were identical to those presented in Table 1 of Nam et al.[143] and are available for reference in Table 4.1.

4.2.5 Asymmetry

To quantify asymmetric broadening of the water resonance, we use a unitless spectral asymmetry metric[66,125,157,158]. At each voxel, the high-field half of the spectrum is subtracted from the low-field half and normalized by the total integral of the spectrum.

$$\text{Asymmetry}(\text{x},\text{y},\text{z}) = \frac{\int_0^{\nu_{\max}} \text{f}(\text{x},\text{y},\text{z},\nu)\,\text{d}\nu - \int_{-\nu_{\max}}^{0} \text{f}(\text{x},\text{y},\text{z},\nu)\,\text{d}\nu}{\int_{-\nu_{\max}}^{\nu_{\max}} \text{f}(\text{x},\text{y},\text{z},\nu)\,\text{d}\nu}, \tag{4.4}$$

where $f(x, y, z, \nu)$ is the value of the water spectrum at a given position (x, y, z) and frequency ν. Integration was performed to $\nu_{\max} = \pm 38$ Hz from the main water peak (identified at 0 Hz for simplicity) to ensure that resonance details are captured while still reaching the spectral baseline. This cutoff value was shown in a previous study[125] to lead to asymmetry values sensitive to the differences between control and shiverer white matter. Overall, asymmetry results are robust to the specific choice of threshold (Figure 4.3). Integration was performed numerically in Python using the trapezoid rule. Before calculating asymmetry from the biophysical models, spectra were first computed by evaluating the analytic time-domain models at the echo points measured in the data using the parameters estimated for each voxel, then taking a fast Fourier transform.

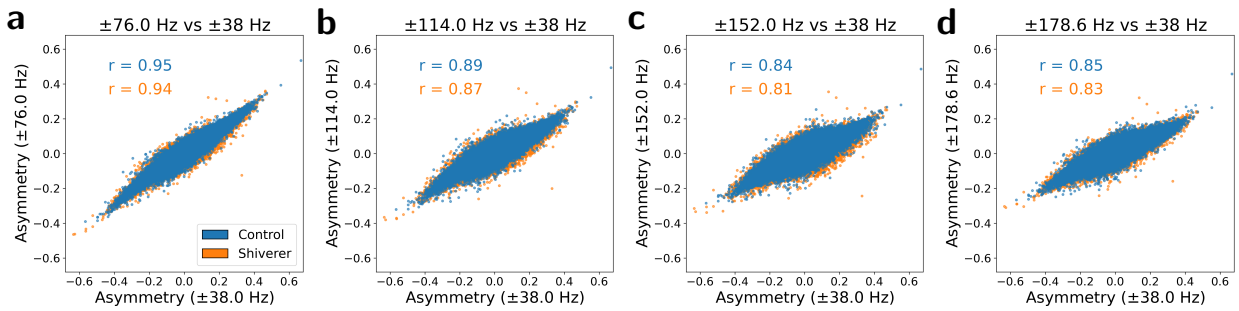

Figure 4.3: Scatterplots of data-derived asymmetry values calculated with a cutoff frequency of ±38 Hz vs. (a) ±76 Hz, (b) ±114 Hz, (c) ±152 Hz, and (d) ±178.6 Hz. r-values indicate Pearson's correlation coefficients, which remain above 0.8 for both control and shiverer datasets out to ±178.6 Hz.

4.2.6 Additional model-derived metrics

Three-compartment models are commonly fit to MGE data in order to calculate the myelin water fraction (MWF) metric, taken as the ratio of the myelin-compartment amplitude A_{my} to the total sum of amplitudes from each compartment:

$$\text{MWF} = \frac{A_{\text{my}}}{A_{\text{my}} + A_{\text{ex}} + A_{\text{ax}}}. \tag{4.5}$$

This metric was calculated at each voxel from the amplitude parameters estimated from both the magnitude- and complex-fit models in order to compare and evaluate the utility of the asymmetric metric. As an additional baseline, R_2^* values were estimated at each voxel by fitting the FID signal $S_i(t)$ at each voxel i to a simple monoexponential model:

$$S_i(t) = A_i \exp\left(-R_{2,i}^* t\right). \tag{4.6}$$

4.2.7 dMRI processing

fODF fitting and registration

dMRI processing was performed with the MRtrix3 software package[126]. Data were denoised using the `dwidenoise` routine[68,69]. Binary brain masks were generated with the `dwi2mask` routine to speed further processing. The datasets were fit to a tensor model[9] using `dwi2tensor` to calculate the fractional anisotropy (FA) metric used as a proxy for white matter content. The data were then fit to fiber orientation distribution functions (fODFs) using constrained spherical deconvolution[16,17] to estimate the orientation of the principal fiber populations and to evaluate the presence of additional crossing fiber populations within each voxel. Comparison of fODFs across datasets requires global intensity normalization of the diffusion data prior to reconstruction, since the data are not first log-normalized with the b_0 volume. First, the data were bias-corrected using the `N4BiasFieldCorrection` algorithm[159] in ANTs, then global intensity normalization was done with the `dwinormalise group` routine in MRTrix3. White matter response functions were then calculated for each dataset using the `tournier` algorithm[72], with $\ell_{\max} = 6$ (28 coefficients). The group-averaged response function was then used to fit the bias-corrected diffusion-weighted images to fODFs with the `dwi2fod` command.

The FA images were spatially registered to the corresponding EPSI peak-height images using affine transformations calculated in ANTs using a mutual information maximization approach. The FA images were chosen for registration because they exhibit greater white/gray matter contrast, particularly for the shiverer data. The resulting affine transformations were used to warp, reorient[82], and modulate[18] the fODFs using the `mrtransform` command in MRTrix3, which preserves apparent fiber densities across fODF lobes before and after spatial transformation.

Microstructural analysis

As in Foxley et al.[125], voxels across the entire dataset were binned according to FA value with thresholds of FA ≤ 0.3, $0.3 <$ FA ≤ 0.45, $0.45 <$ FA ≤ 0.6, and FA > 0.6. Visual inspection of the resulting voxel masks suggests that the lower FA ≤ 0.3 bin consists of predominately gray matter while the upper FA > 0.6 bin consists of predominately white matter, with the additional two bins composed of mixed populations. To account for known biases in FA in voxels with crossing fibers[160], voxels were further characterized by the number of distinct fiber populations. Individual lobes of each fODF were segmented in MRTrix3 using the `fod2fixel` and `fixel2peaks` commands. The number of populations (N_f) at each voxel was recorded as either "single" ($N_f = 1$) or "crossing" ($N_f > 1$). Voxel-wise changes in T_2^*[161,162] and spectral asymmetry[66,125] have been observed to change as a function of the angle between the orientation of the principal fiber populations and B_0, which has been described as evidence of the susceptibility anisotropy of myelin[162–165]. To explore this effect in the model-derived spectra, the angle between principal fiber orientations and B_0 was calculated as $\Gamma = \cos^{-1}(s_z)$, where $\hat{\boldsymbol{s}} = (s_x, s_y, s_z)$ is the fiber orientation unit vector at a given voxel and B_0 points along $\hat{s}_{B_0} = (0, 0, 1)$. Due to the symmetry of the fODFs, Γ values were manually constrained to be within $[0°, 90°]$. Voxels with both single and crossing fibers were pooled by angle into bins in 5° increments based on the orientation of the primary fiber population.

4.2.8 Statistical analysis

Direct relationships between model- and data-derived asymmetries were evaluated through comparison of overall distributions and assessment of linear correlations with respect to FA and the number of fiber populations. The relationship between the model fit and asymmetry accuracy was assessed by analyzing correlations between the adjusted R^2 of the model fits to the absolute difference between data- and model-derived asymmetries. We similarly

evaluated correlations between estimated compartmental frequency shifts and the resulting data-measured asymmetry.

We evaluated the sensitivity of the data- and model-derived to the white-matter differences between control and shiverer mice by considering asymmetry as a one-variable binary classifier for control or shiverer data and using the area (AUC) under the receiver operating curve (ROC) as a function of FA and the number of fiber populations. For this analysis, ROC curves were created by taking the distribution of voxel-wise control and shiverer asymmetries for each FA bin and fiber population number group, varying the asymmetry threshold value used to identify test voxels from the control datasets, and calculating the overall sensitivity and specificity at each threshold. The AUC was then calculated by numerical integration of the ROC curve. This procedure was repeated for the MWF and R_2^* metrics for comparison to asymmetry.

4.3 Results

Here we present analysis comparing spectral asymmetric broadening measured directly from the data to asymmetric broadening estimated with two biophysical models fit to the same data. Our goal is not to propose asymmetry as a novel imaging biomarker, but to demonstrate the utility of model-free spectral analysis towards revealing biases in current models and guiding future model development. Our assumption throughout is that the differences in white matter between control and shiverer mice reveal biologically meaningful sensitivities that allow for fair comparison of the performance of the data- and model-derived spectral asymmetry metrics as well as the MWF and R_2^*.

4.3.1 Comparison of asymmetry values

Figure 4.4 shows the distribution of asymmetry values calculated from the raw data and both models across all voxels from control and shiverer samples. At the whole-brain level there is

a small but clear separation between control and shiverer asymmetry values observed in the data, whereas both model-derived asymmetry distributions are virtually indistinguishable between control and shiverer. Spectra derived from each of the two biophysical models also dramatically underestimate the range of asymmetry magnitudes observed in the data. Across all voxels in both tissue types, data-derived asymmetry has a standard deviation of 0.0427, while the magnitude- and complex-fit asymmetries have standard deviations of 0.0140 and 0.0058, respectively.

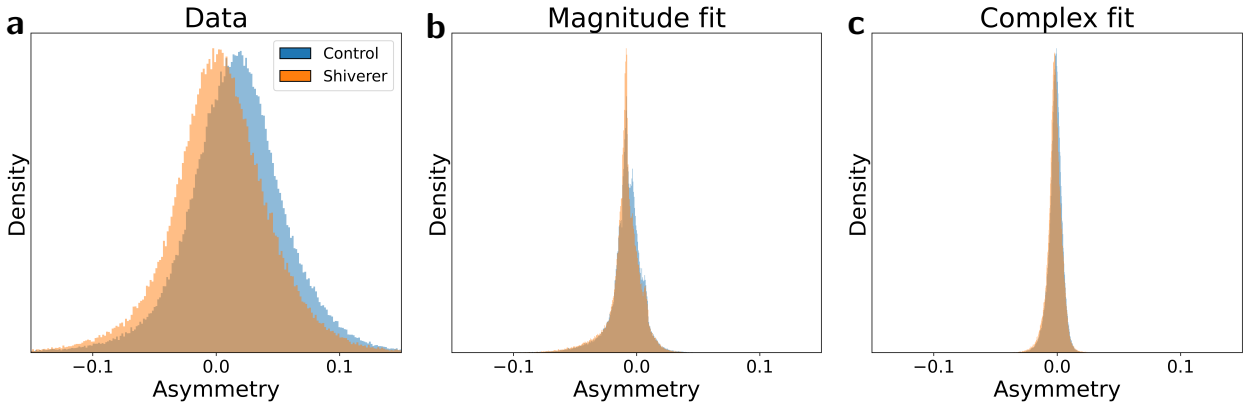

Figure 4.4: Histograms of asymmetries from spectra derived from (a) data, (b) the magnitude-fit model, and (c) the complex-fit model.

Voxel-wise comparisons between data- and model-derived asymmetries are shown as scatterplots across different FA bins in Figure 4.5. Asymmetries from the magnitude-fit model show negligible correlation ($R^2 \approx 0$) with data-derived asymmetries from both control and shiverer samples across all FA bins. The complex-fit model performs slightly better, with R^2 values that increase with increasing FA for control data, up to a maximum of $R^2 = 0.403$ for the highest FA bin. All R^2 values were found to be significant at the $\alpha = 0.1$ level using an F-test. Complex-fit correlations are lower in shiverer data than in control data and do not increase with FA.

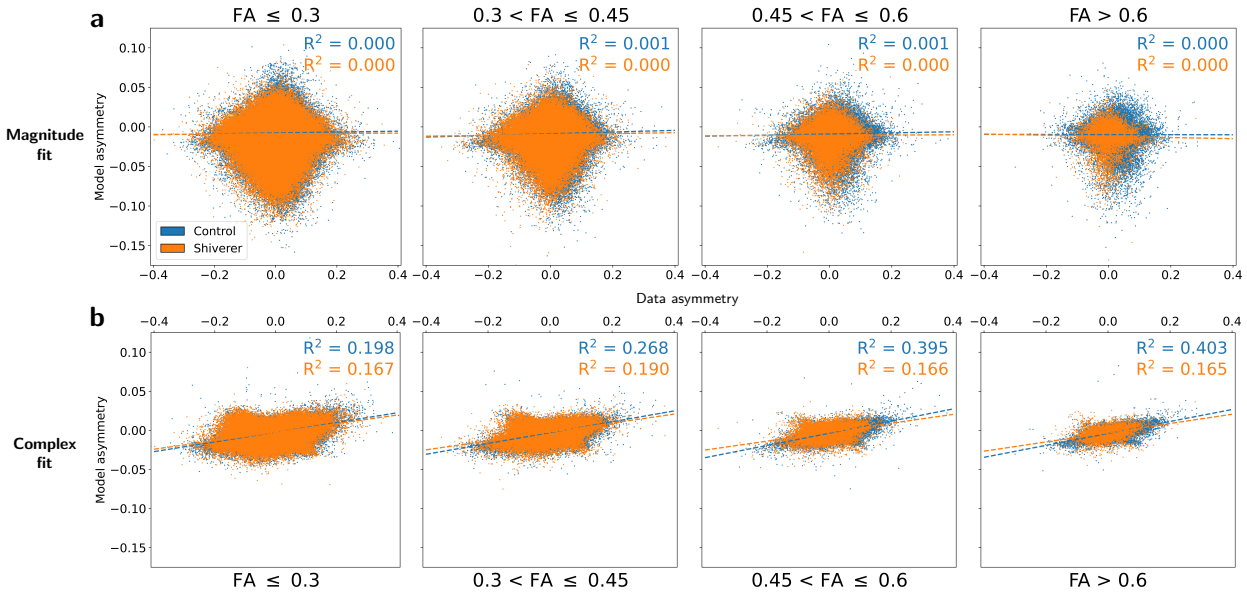

Figure 4.5: Scatterplots of data- and model-derived asymmetries for the (a) magnitude-fit and (b) complex-fit models. Dashed lines represent the results of linear regressions and the R^2 values are the square of the Pearson correlation coefficients.

Figures 4.6a–b show 2D histograms of the absolute asymmetry difference between the models and data vs. the adjusted R^2 assessing the goodness-of-fit of the models to the FID data for voxels with FA > 0.6. Both models generally fit the FID data very well overall, with the mean adjusted R^2 values across all voxels from both tissue types being 0.994 and 0.988 for the magnitude-fit and complex-fit models, respectively.

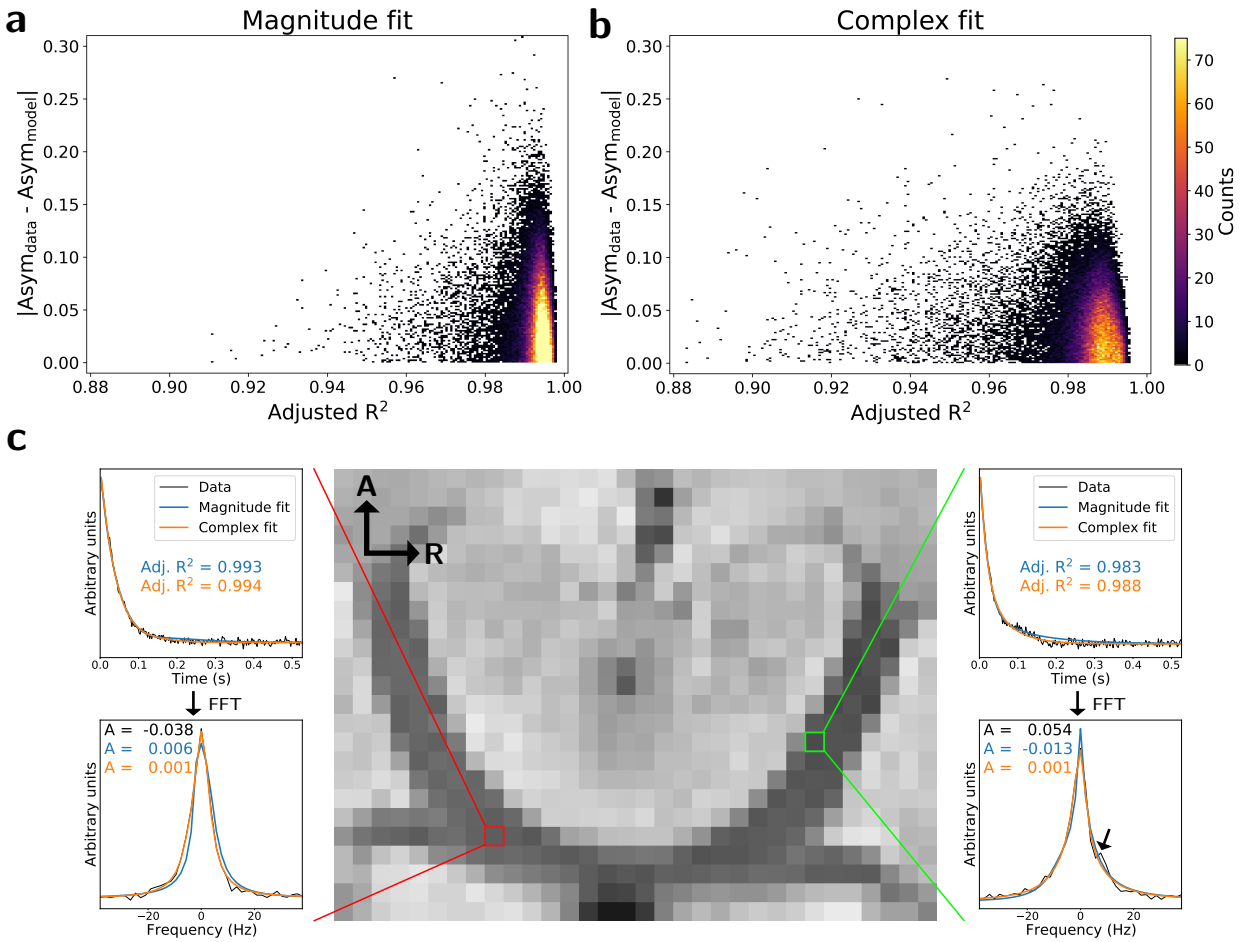

Figure 4.6: (a-b) 2D histograms of the absolute difference between measured and model-estimated asymmetries vs. the model goodness-of-fit in terms of adjusted R^2 for the (a) magnitude-fit and (b) complex-fit models for voxels with FA > 0.6. Green dashed lines show linear regressions with associated R^2 values indicating a negligible relationship. (c) Water peak-height image showing the anterior commissure tract of a control mouse with two representative voxels demonstrating the mismatch between the model goodness-of-fit and asymmetry difference. A–R axis labels correspond to the Anterior and Right directions, respectively.

However, the high adjusted R^2 of the models in the temporal domain does not correspond to accuracy in reproducing the asymmetric spectral broadening observed in the data — correlations between the adjusted R^2 and asymmetry difference are negligible for both models. This effect is visually demonstrated further in Figure 4.6c, which shows two representative white-matter voxels from the anterior commissure tract of a control mouse. In both

sample voxels, the two models fit very closely to the data in the temporal domain (adjusted $R^2 > 0.98$) but greatly underestimate asymmetry in the frequency domain. For example, in the case of the voxel highlighted in green, both models clearly miss a prominent secondary peak around 8 Hz (black arrow in Figure 4.6c, bottom right) corresponding to an oscillation in the FID around 0.05-0.18 seconds.

Model fits were further evaluated with the Bayesian information criterion (BIC). The distributions of the differences in BIC between the magnitude-fit model (8 free parameters) and the complex-fit model (10 free parameters) are shown in Figure 4.7. For all FA bins and both control and shiverer data, BICs were lower from the magnitude-fit model than the complex-fit model.

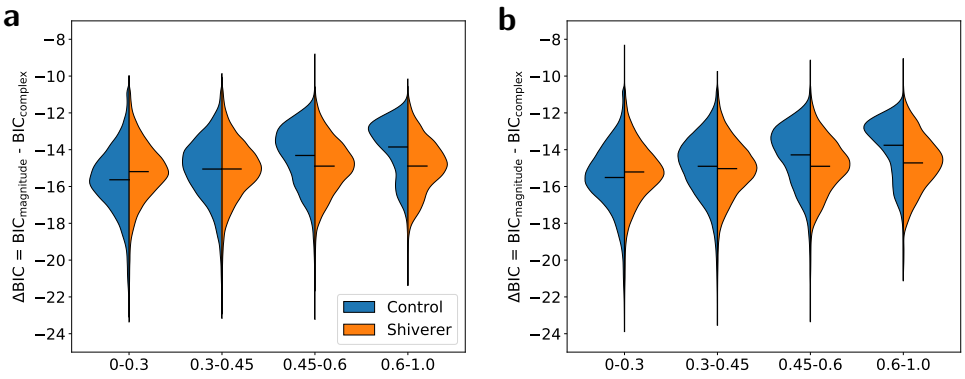

Figure 4.7: Distributions of absolute differences in BIC between the magnitude- and complex-fit models, separated by control/shiverer, FA bin, and (a) single and (b) crossing fiber voxels. The magnitude-fit model led to a consistently lower BIC than the complex-fit model.

Figure 4.8 shows additional 2D histograms for high FA (FA > 0.6) voxels demonstrating the relationship between the asymmetry directly measured in the spectral data and the compartmental frequency shifts predicted by the models. Note that the magnitude-fit model (Eqn. 4.2) includes frequency shift terms for two compartments: $\Delta f_{\mathrm{my-ex}}$ and $\Delta f_{\mathrm{ax-ex}}$, defined as the difference between the myelin and axonal water shift with the the extracellular water shift, respectively. The complex-fit model (Eqn. 4.3) includes frequency shift terms for all three components: $\Delta f_{\mathrm{my+bg}}$, $\Delta f_{\mathrm{ax+bg}}$, $\Delta f_{\mathrm{ex+bg}}$, defined as the additional shifts in

myelin, axonal, and extracellular water, respectively, above a background. For consistent comparison between the two models, the extracellular shifts have been subtracted from the complex-fit model frequencies reported in Figure 4.8. The magnitude-fit frequencies again show virtually no correlation with the measured asymmetry, while the complex-model frequencies show only weak correlation ($R^2 = 0.114$) in the axonal compartment.

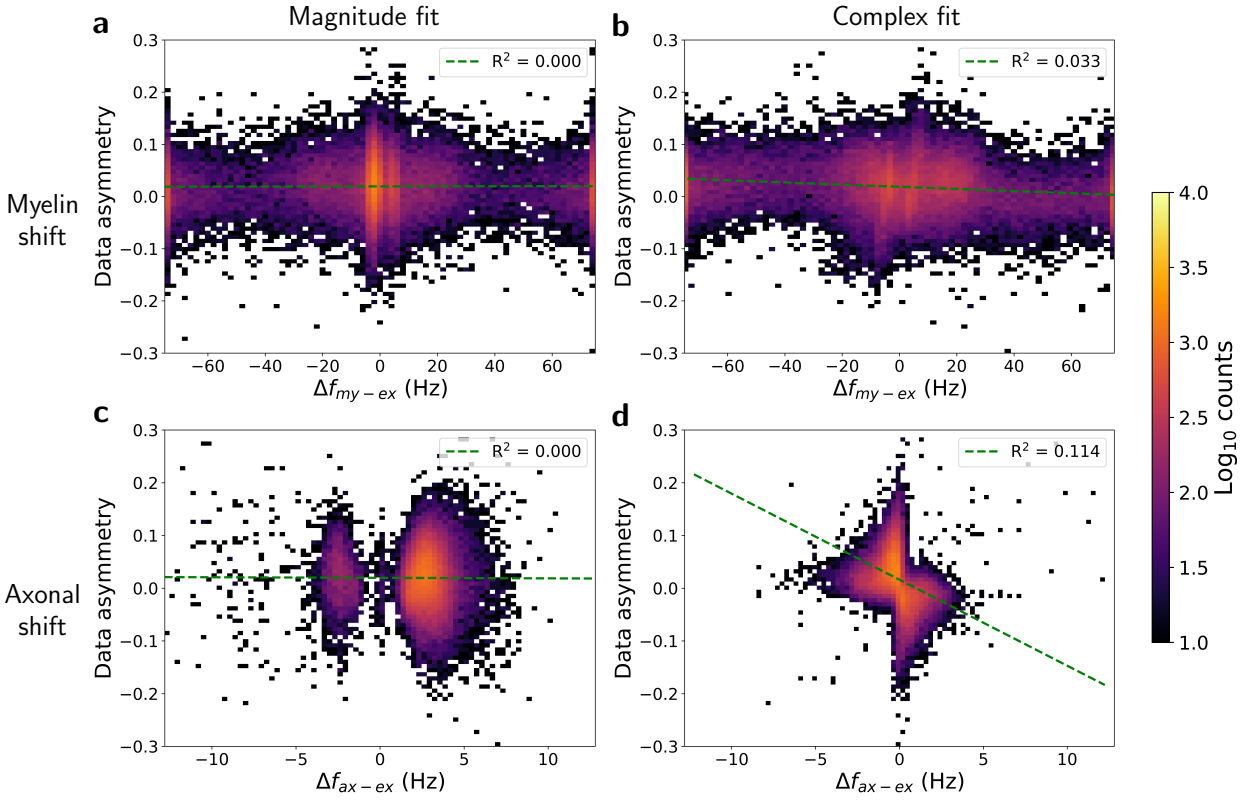

Figure 4.8: 2D histograms showing the relationship between data asymmetry and model-predicted frequency shifts for the myelin and axonal water compartments in voxels with FA > 0.6. Green dashed lines show linear regressions with associated R^2 values.

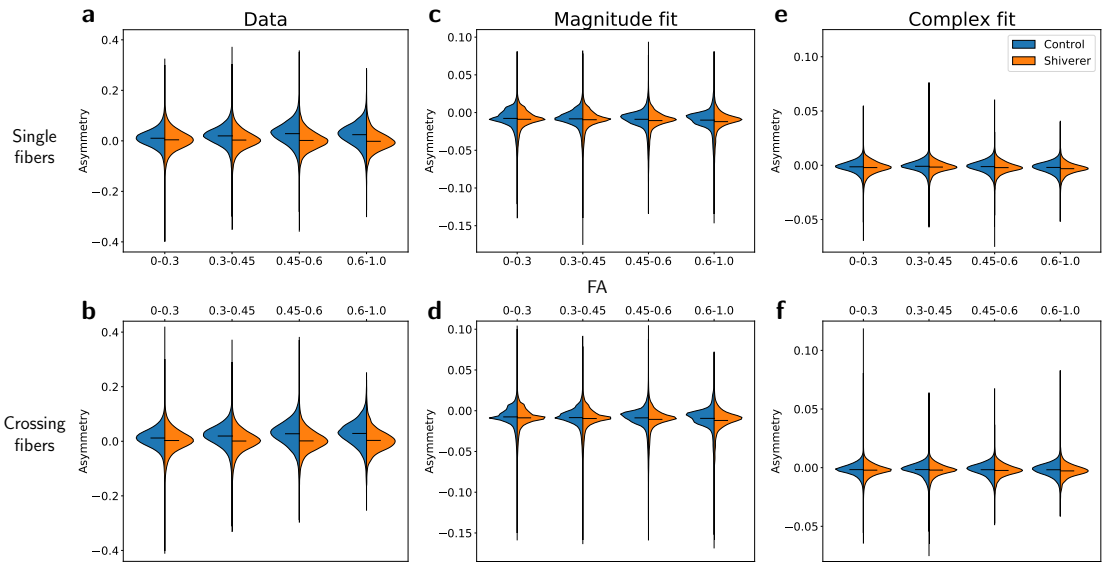

Figure 4.9: Violin plots illustrating distributions of control and shiverer asymmetries derived from (a–b) data, (c–d) the magnitude-fit model, and (e–f) the complex-fit model as a function of FA bin for voxels with single (a,c,e) and crossing (b,d,f) fibers. Distribution means are indicated by black lines. Note the difference in y-axis limits between (a–b), (c–d), and (e–f).

4.3.2 Sensitivity to shiverer white matter

While Figure 4.4 showed the range of asymmetry values across the entire dataset, Figure 4.9 shows data- and model-derived asymmetry distributions grouped by FA bin for single- and crossing-fiber voxels. Previous work has shown that data-derived spectral asymmetry is sensitive to white-matter differences between control and shiverer mice[125], with spectra exhibiting consistent upfield broadening along white-matter tracts in control mice that decreases in magnitude in shiverer mice. This is demonstrated in Figures 4.9a–b, which show an increasing separation between control and shiverer data-derived asymmetries as FA increases, independent of the number of fiber populations. This effect is not observed to the same extent after fitting the data to models, as shown in Figures 4.9c–f. The separation between the control and shiverer distributions is quantified in Figure 4.10 by treating spectral asymmetry as a one-variable classifier and reporting the resulting AUC as a function of FA for single- and crossing-fiber voxels. An AUC value of 0.5 is consistent with a "random

guessing" classifier (i.e. no separation), while a value of 1.0 indicates perfect classification (i.e. complete separation). While separation between the control and shiverer distributions did increase marginally with FA for both models, data-derived asymmetry led to a substantially higher AUC than either of the model-based approaches under all microstructural conditions. Notably, the performance of data-derived asymmetry in classifying control from shiverer tissue was robust to the number of fiber populations, with only slight decreases in AUC for higher FA voxels with crossing fibers (FA > 0.45) compared to single fibers and slight increases for lower FA voxels with crossing fibers (FA ≤ 0.45) compared to single fibers, potentially owing to the fact that voxels with tightly packed, coherent fibers are likely to lead to artificially low FA values

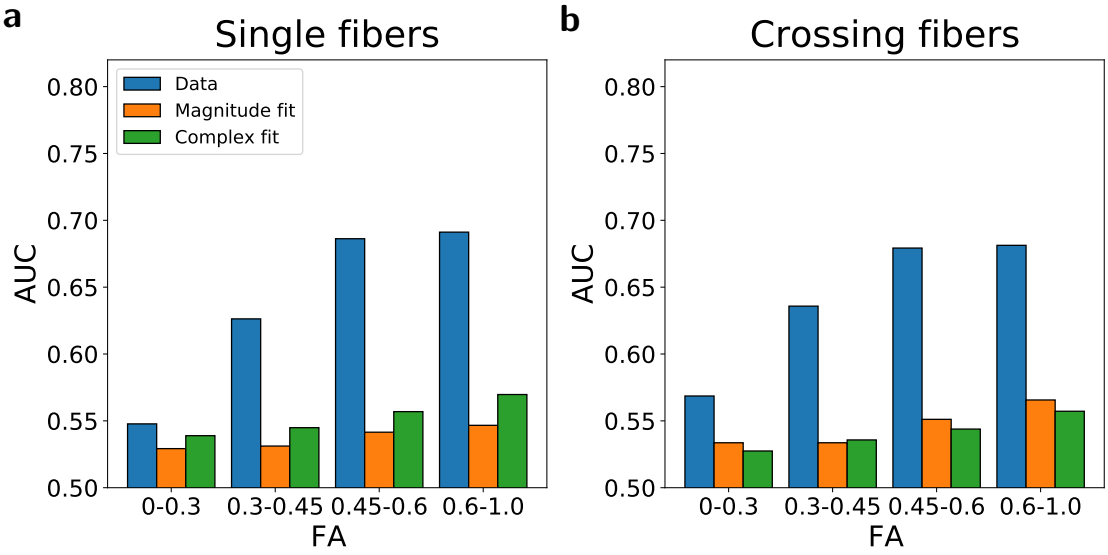

Figure 4.10: Values for the area under the ROC curve (AUC) using asymmetry as a one-variable classifier for control vs. shiverer data. Values represent AUCs for subsets of voxels in different FA bins containing either (a) single or (b) crossing fiber populations.

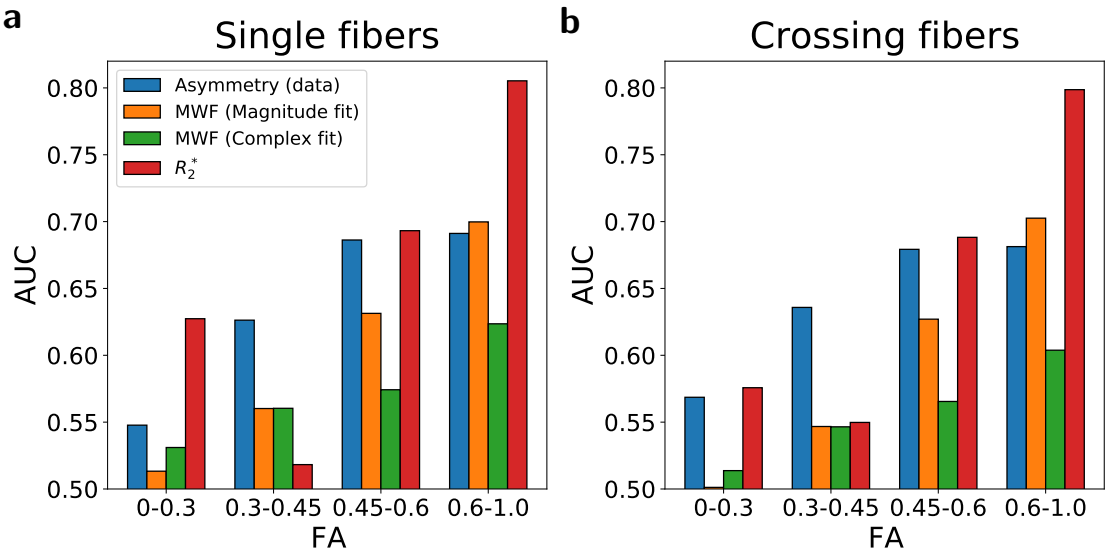

Figure 4.11: Values for the area under the ROC curve (AUC) using data asymmetry (blue), model-based MWF (orange and green), and R_2^* (red) as one-variable classifiers for control vs. shiverer data. Values represent AUCs for subsets of voxels in different FA bins containing either (a) single or (b) crossing fiber populations.

if they contain multiple distinct populations.

In Figure 4.11, data-derived asymmetry AUCs are compared to AUC results from a similar ROC analysis procedure performed using the MWF metric calculated with both models as well as the R_2^* calculated with a simple monoexponential fit. Data asymmetry led to a greater separation between control and shiverer data than both model-derived MWF values for low-FA voxels (FA ≤ 0.6), while asymmetry and magnitude-fit MWF AUCs were comparable for high-FA voxels (FA > 0.6). AUCs for the R_2^* were considerably higher in high-FA voxels (FA > 0.6) than AUCs for both asymmetry and MWF.

The white-matter sensitivity of the data-derived asymmetry is further demonstrated in the left column of Figure 4.12, which shows representative coronal slices of asymmetry images. While the data-derived asymmetry leads to observable gray/white-matter contrast in the control image comparable to the MWF images in Figures 4.12g–j, asymmetry images calculated from each of the models (Figures 4.12c–f) show markedly lower contrast, with virtually no distinguishable white matter tracts visible in the images derived from the

magnitude-fit model in particular.

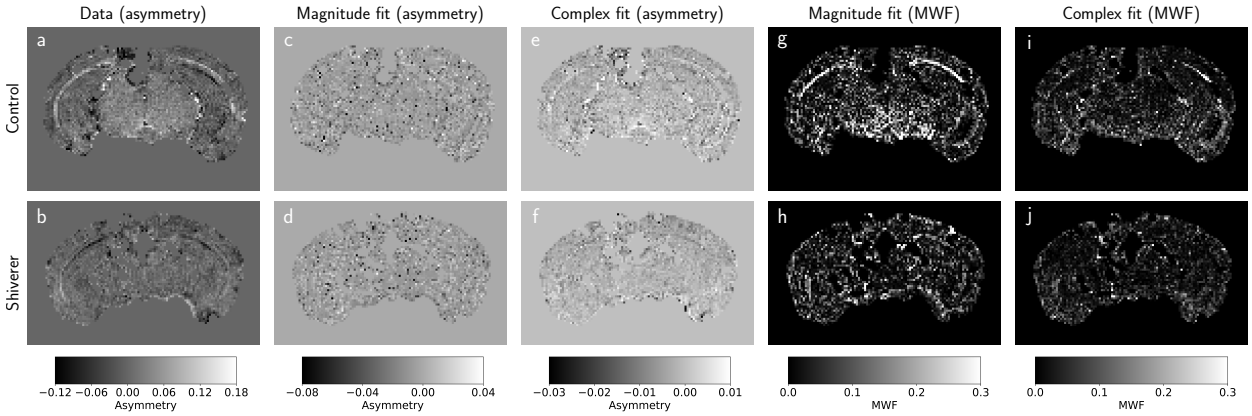

Figure 4.12: Representative coronal slices of images derived from (top) control and (bottom) shiverer samples. Images represent spatial distributions of (a–b) data-derived asymmetry, (c–d) magnitude-fit asymmetry, (e–f) complex-fit asymmetry, (g–h) magnitude-fit MWF, and (i–j) complex-fit MWF.

To explore the orientation-dependence of the model-estimated spectra, Figure 4.13 shows the mean asymmetry as a function of Γ, the angle between the orientation of the primary fiber population and B_0 for voxels with FA $\geq$ 0.6. Color-shaded regions represent the interquartile range (25–75th percentile) across all voxels within each angular bin, and gray-shaded regions represent regions where the difference between control and shiverer values was not found to be statistically significant using a t-test with $\alpha = 0.01$ after correcting for multiple comparisons. Both the data and the complex-fit asymmetry values show a clear relationship between asymmetry and Γ with good agreement with the susceptibility anisotropy model[162],

$$\text{asym}(\Gamma) = c_0 + c_1 \sin(2\Gamma + \phi_0) + c_2 \sin(4\Gamma + \phi_1), \tag{4.7}$$

though the angular effect is much less pronounced for the magnitude-fit model and both models once again show far less separation between control and shiverer values than observed from the data before model-fitting. Note that data-based adjusted R^2 values to the sus-

ceptibility anisotropy model are slightly lower for voxels with crossing fibers (Figure 4.13b) than for voxels with single fibers (Figure 4.13a), again suggesting that the performance of macroscopic imaging models are sensitive to the microstructural geometry of the underlying tissue.

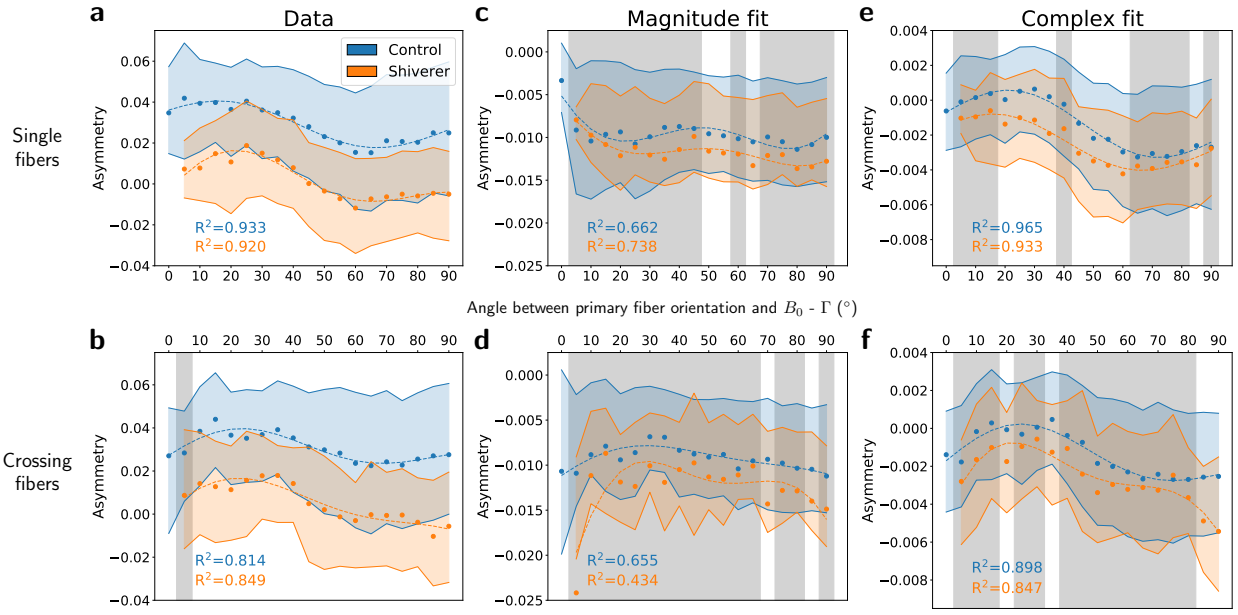

Figure 4.13: Relationship between asymmetry and Γ, the angle between the orientation of the primary fiber population and B_0 for (a–b) data (c–d) the magnitude-fit model, and (e–f) the complex-fit model. Points represent averages within angular bins with a width of 5° across all voxels with FA ≥ 0.6 containing either (a,c,e) single fibers or (b,d,f) crossing fibers. Color-shaded regions represent the interquartile range (25-75th percentiles) across all voxels. Dotted lines represent fits to the susceptibility anisotropy model with associated adjusted R^2 values. Gray regions represent angular bins for which the difference between control and shiverer values was not found to be significant with a t-test at $\alpha = 0.01$.

4.4 Discussion

This study aimed to characterize the extent to which water spectra derived from two biophysical signal models fit to EPSI MRI data are able to replicate the spectral characteristics observed directly from the data itself, specifically with respect to sensitivity to white-matter differences between control and shiverer mice. We used spectral asymmetry around the main

water peak as a summary metric to explore how data- and model-derived spectra differ over a range of microstructural environments, covering variations in white matter content using FA as a proxy metric, the role of crossing fibers, and the angle between the orientation of the primary fiber population and B_0. The goal was to use the asymmetry as a demonstrative spectral metric to reveal areas of improvement for future model development. Our overall finding is that independent of how well the models fit the temporal FID data, neither model was able to accurately reproduce the asymmetric broadening observed directly in the data. The simplicity of the models provides interpretability and computational advantage at the expense of failing to capture the full complexity of the spectra. This results in a dramatic underestimation of the magnitude of the asymmetric broadening effect (Figure 4.4), with model-derived values for asymmetry that only loosely correlate with those measured in the data in high-FA voxels (Figure 4.5). Most importantly, the process of fitting the data to these simple biophysical models effectively leads to compromised spectral sensitivity to changes in white matter structure under all microstructural conditions explored in this work (Figure 4.10 and 4.12).

While the above conclusions apply broadly to both the magnitude- and complex-fit models, the complex-fit model did perform slightly better with respect to certain spectral characteristics, a finding consistent with previous work comparing these two models[143]. Complex-fit asymmetries correlated more strongly with data-measured asymmetries across all FA bins (Figure 4.5) than did magnitude-fit asymmetries. Similarly, the axonal water compartment frequency shift estimated from the complex-fit model was the only compartmental frequency shown to have any correlation with the raw-data asymmetry (Figure 4.8). Complex-fit asymmetries were also shown to have a stronger relationship to the angle between the fiber orientation and B_0 than magnitude-fit asymmetries (Figure 4.13). Overall, however, both models showed relatively poor performance with respect to spectral white-matter sensitivity and contrast (Figures 4.10 and 4.12). The complex-fit model also showed slightly worse per-

formance than the magnitude-fit model with respect to white-matter sensitivity using the MWF metric, as well as consistently lower BIC values (Figure 4.7).

The data-derived asymmetry results presented in this work are consistent with previous studies demonstrating the utility of model-free analysis of fully-sampled MGE/EPSI data in the frequency domain towards white-matter imaging[65,66,125]. This work extends such analyses to reveal biases in existing biophysical models due in part to the simplicity of their underlying geometric assumptions[164]. Through full sampling of the FID to the noise floor, our results indicate that these biases are indeed present in the explored compartmental models even at the level of compressing the full spectral information into a single scalar asymmetry metric, promoting caution in the downstream interpretation of model-predicted spectra.

Notably, this work also demonstrates the robustness of the asymmetry metric under complex microstructural conditions. Measured asymmetries were shown to have comparable sensitivities to white matter (Figure 4.10) and demonstrate similar behavior with respect to fiber angle (Figure 4.13) in voxels with single and crossing fibers. A direction of future work will be to more rigorously characterize the spectral response to the specific number as well as relative strength and position of fiber populations within the voxel.

This analysis method of benchmarking spectroscopic MR data in the temporal domain against data in the spectral domain can be extended to existing datasets after applying a linear transform to the FID to produce absorption spectra. We note, however, the importance of sampling to the results in this work – the sensitivity of the spectral analysis is dependent on the increased spectral resolution that comes by sampling the FID into the noise floor. Figure 4.14 shows AUCs similar to Figure 4.10, and demonstrates that after truncating the FID to just the first 32 echoes, neither the data- nor the model-derived asymmetries show meaningful sensitivity to myelin, while Figure 4.15 shows that myelin sensitivity as represented by the AUC stabilizes for data-derived asymmetry around 64 echoes.

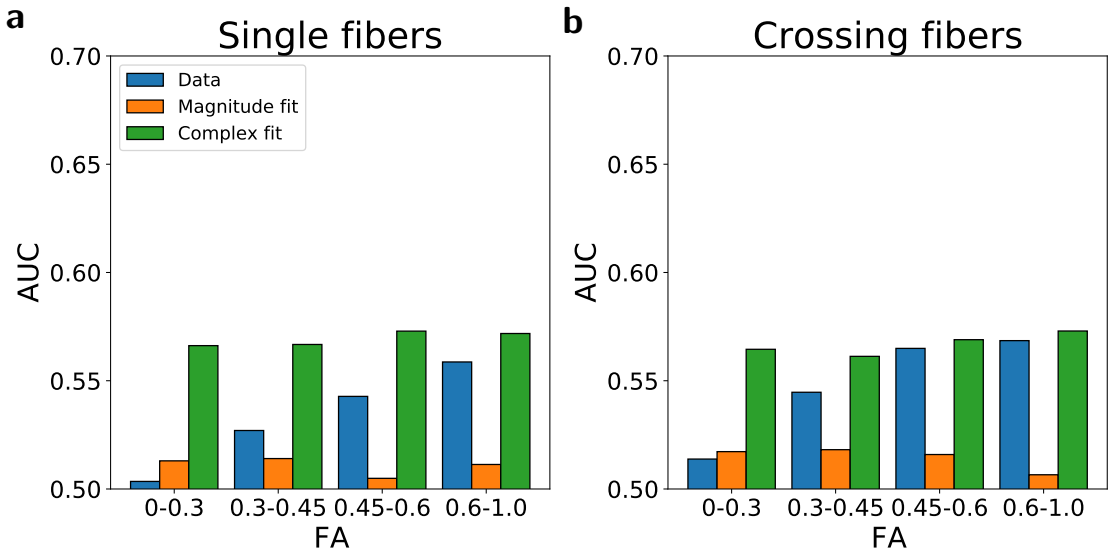

Figure 4.14: Values for the area under the ROC curve (AUC) using asymmetry as a one-variable classifier for control vs. shiverer data. FIDs were first truncated to 32 echoes prior to model-fitting and calculation of spectral asymmetry. Values represent AUCs for subsets of voxels in different FA bins containing either (a) single or (b) crossing fiber populations. With 32 echoes, neither the data nor either of the models is able to demonstrate meaningful sensitivity to myelin from the asymmetry, highlighting the need for high spectral resolution, or equivalently, extended FID sampling.

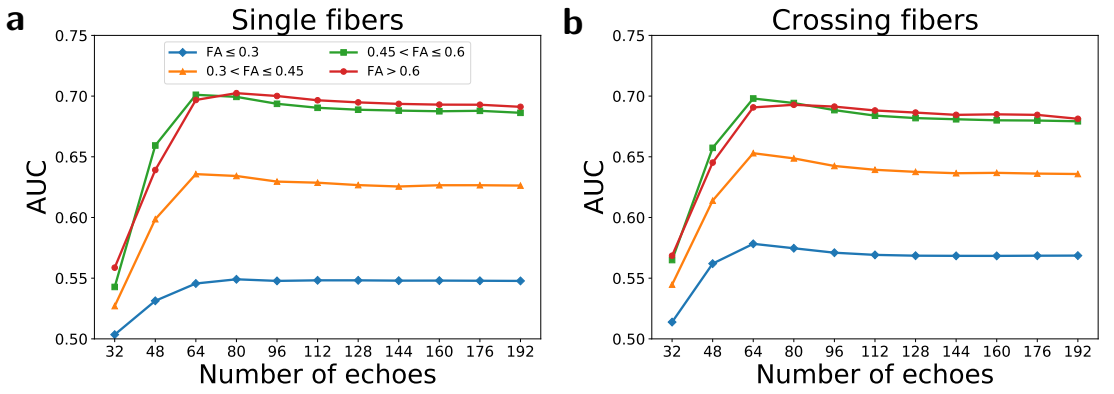

Figure 4.15: AUC values using data-derived asymmetry as a one-variable classifier for control vs. shiverer data as a function of the number of echoes in the FID. Subsampled-FIDs were created by truncating the full (192 echo) FIDs to the specified values prior to calculating asymmetry in the frequency domain. Values represent AUCs for subsets of voxels in different FA bins containing either (a) single or (b) crossing fiber populations. This demonstrates the importance of spectral resolution, or equivalently, extended FID sampling, and provides a roadmap for future benchmarking studies using EPSI spectral data.

As in previous work[125], the relationship of asymmetry to fiber angle was shown to be present, but diminished in magnitude in dysmyelinated shiverer mice relative to control mice. We hypothesize that differences in myelin content and structure between control and shiverer mice play a sizable role both in this effect and in additional findings of this study. We note, however, that we are unable to isolate myelin as a specific driver of spectral asymmetry without independent histological validation of myelin content. This raises the importance of such quantitative histological validation in future studies for analysis of both asymmetry and model-derived parameters such as MWF. Incorporating full demyelination models in future studies will also help further clarify the specific role of myelin in driving asymmetric broadening of the spectrum. More robust analysis of data from control and fully demyelinated mice will also help to identify specific spectral features beyond asymmetry that could potentially form new imaging biomarkers and motivate the development of new biophysical models that remain interpretable and clinically useful without compromising myelin sensitivity.

Notably, the highest AUC observed for the task of classifying structural differences in white matter between control and shiverer data came from the simple monoexponential R_2^* estimate in high-FA voxels (Figure 4.11), which outperformed both the data-derived spectral asymmetry and model-derived MWF values. This suggests that the failure of the multi-exponential models to faithfully estimate relevant spectral features in the data potentially weakened their sensitivity to the meaningful differences in white matter between control and shiverer mice. Equivalently, this suggests that improvements to the spectral components of future biophysical modeling pipelines could lead to improved sensitivity to relevant white-matter features such as myelin. While the R_2^* fit also outperformed the data-derived asymmetry in terms of AUC, we note that these two metrics provide independent, complementary information pertaining to white matter structure, highlighting the importance of both accurate temporal- and spectral-domain components to biophysical white-matter

models. This is demonstrated through scatterplots of data spectral asymmetry and R_2^* in Figure 4.16. Correlations between the two values are negligible; while the R_2^* metric indicates the total amount of broadening of the water resonance line, it does not communicate any information about the asymmetric nature of that broadening and whether it is up- or down-field.

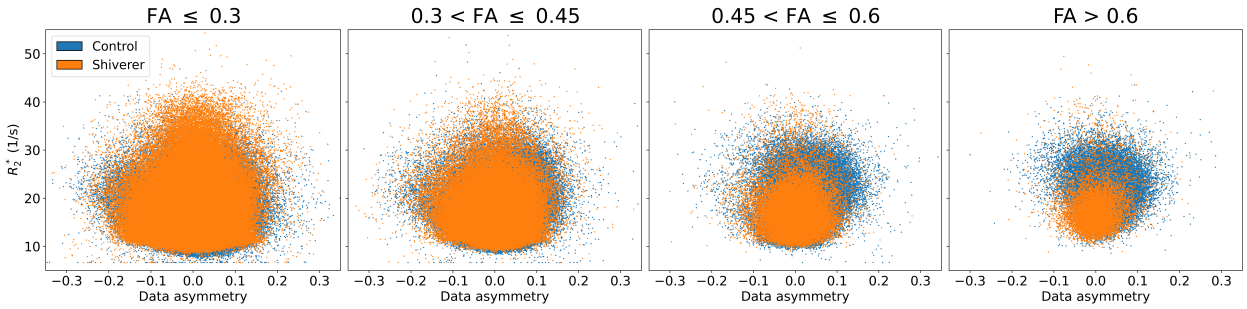

Figure 4.16: Scatterplots of data-derived asymmetry and R_2^* split by control (blue) and shiverer (orange) and FA bin. Correlations were negligible for all FA bins.

Overall, we feel that our analysis reveals that there is underutilized spectral information within EPSI data that yields important insight to white matter structure complementary to information from traditional temporal-domain metrics such as MWF and R_2^*. This motivates further the development of spectral-domain components of biophysical white-matter models. Model development and physical parameter ranges have typically relied on simulations using a simple underlying geometric model of white matter that uses nested, circular cylinders to describe axons[144,166,167]. A recent study[164] simulated the MR signal arising from axons under different 2D geometric models. It showed that as the axon geometry model becomes more realistic through the use of warped cylinders and segmented cross-sections from electron micrographs, the generated microscopic magnetic field becomes increasingly complex and the compartment-specific components of the resulting water spectra become much less pronounced and distinct, leading to asymmetric broadening around the main peak as opposed to discernible narrow peaks corresponding to each compartment. Though part of this effect could potentially be attributed to fixation-related warping of the axons imaged with

electron microscopy for the study, these results still suggest that quantitative microstructural imaging pipelines that rely on biophysical models might be biased by the models' assumed geometries. Recent analysis of mouse brain data using a novel multi-scale, multi-modal imaging pipeline[63] has demonstrated that the geometric complexity of axon populations increases dramatically in three dimensions; non-cylindrical nerve fibers undulate, fan, and cross within MRI-sized-voxels. Such datasets will be important for future MR simulation studies that use realistic 3D white-matter models to further explore the spectral signatures of white-matter tissue microstructure under different geometric configurations. In many results of this work, we observed that model performance was highly sensitive to the underlying tissue microstructure; for example, complex-fit asymmetry correlations to data-derived asymmetry increased with FA for control data but not for shiverer data. The results of realistic 3D simulation studies could potentially guide the development of hybrid microstructural myelin imaging approaches where geometric and structural information from dMRI data could be used for selection of relevant model components and parameters for EPSI data.

CHAPTER 5

CONCLUSIONS

In this work, we have seen that MR microstructure imaging methods such as dMRI and EPSI offer the potential to provide cellular-level neurological information at a macroscopic scale in vivo. By estimating sub-resolution tissue parameters, these methods show great promise in helping to bridge the gap between cellular imaging modalities that are prohibitively destructive for in vivo human imaging. By necessity, these MR approaches rely on heuristic or biophysical signal models in order to reconstruct relevant biological properties of the underlying tissue. Throughout this dissertation, we have introduced multi-modal datasets and analysis methods that demonstrate the necessity for validation of these MR methods with additional ground-truth imaging. A common theme has been that high-resolution information from validation modalities allows for the quantification of biases in MR signal and reconstruction models and these insights in turn can help guide the development of improved acquisition and reconstruction pipelines.

In Chapter 2, we demonstrated a processing pipeline developed for dMRI validation with synchrotron microCT. MicroCT provides isotropic resolution across whole mouse brains with no physical sectioning, addressing limitations in existing optical-based dMRI validation methods. Fiber orientations were estimated and processed into fODFs across the whole brain and spatially registered to dMRI data of the same specimen. Comparisons between modalities showed good agreement in the representation of local fiber geometries and the mapping of long-range fiber trajectories, demonstrating the utility of synchrotron microCT for future dMRI validation studies. Future analysis with the full multi-modal pipeline including follow-up imaging of small volumes with serial EM could potentially lead to sample-specific tractography connectome validation using automated machine-learning based axon segmentation routines, as well as to improvements in MR white-matter models through simulation studies built off of 3D EM datasets matched directly to MRI data from the same sample.

In Chapter 3, we used geometric surrogate graphs to explore the role of spatial embedding in the topological properties of the mouse structural brain network measured by neural tracer imaging and diffusion MRI tractography. We found that spatial embedding played a considerably larger role in the topology of tractography networks than tracer networks. Tractography approaches underestimate long-range connectivity, which leads to geometric biases in the estimated modular structure and placement of high-strength hub nodes. Our results demonstrate the caution required in the interpretation of tractography-derived network measurements that rely on long-range connections and motivate additional geometric consideration in the design of future tractography validation studies.

Through analysis of fully-sampled MR spectra from control and dysmyelinated mouse brain in Chapter 4, we revealed limitations in spectra estimated with existing biophysical compartmental models traditionally used for myelin imaging. We showed that spectra estimated from these biophysical models fail to accurately predict the extent of asymmetric broadening in white-matter voxels, leading ultimately to compromised sensitivity to important differences in white-matter structure. This work further demonstrates the utility of model-free analysis of the water resonance spectrum with fully-sampled EPSI data, promoting its continued development as a tool to benchmark novel biophysical signal models and as a potential future in vivo MRI biomarker for dysmyelination.

Throughout, we have aimed to highlight the value that high-resolution ground-truth imaging brings towards an understanding of the nature of the MR reconstruction problems themselves. The dMRI fODFs analyzed in Chapter 2 nominally represent orientation distributions of nerve fibers, but are actually driven by the process of water molecules diffusing and interacting with an extraordinarily complex microstructural tissue environment containing different cell types and geometric configurations. Structure tensor-derived fODFs from microCT do not characterize this diffusion process but instead provide benchmark estimations for the ultimately desired parameter of nerve fiber orientations. Accordingly,

while these two fODFs represent fundamentally different processes, we have demonstrated how structure tensor-derived fODFs can help filter out the "noise" parameters from diffusion data. Similarly, the geometric biases analyzed and discussed in Chapter 3 highlight the fact that tractography streamlines do not represent individual neurons; they instead represent probabilistic pathways through a field of estimated fiber orientations. Comparison to highly specific tracer measurements revealed limitations both in terms of connectivity reconstruction (step-wise reconstructions magnify errors at long distances) as well as a sense of the null space of diffusion tractography (tractography based on symmetric diffusion measurements cannot be used to reconstruct directed brain graphs).

In the future, our overall outlook on MR microstructure imaging of the brain is that additional multi-modal validation studies will be needed in order to optimize novel MR imaging pipelines that themselves make use of multi-modal information. Analysis methods such as the use of geometric surrogate graphs can be used to benchmark new tractography methods that seek to address the geometric biases identified in this work. Such validation studies will be particularly useful for the identification of additional MRI biomarkers that can be used as regularizers to help better condition the tractography problem[103]. New tractography pipelines will need to make use of a suite of MRI approaches that incorporate anatomic regularization for streamline seeding and termination, navigate crossing fiber populations using measures of axon diameters and myelin integrity, etc. Large-volume validation datasets from microCT and EM in model organisms will be important for understanding and developing MR signal models that can be used to reconstruct these meaningful priors, ultimately helping to deliver key clinical and basic insights into the structure and function of the human brain.

APPENDIX A

DATA AVAILABILITY

MicroCT data from Chapter 2 can be viewed online through Neuroglancer at the following link: http://tinyurl.com/cxmbjy6b. Tools developed for the calculation and visualization of fiber orientations and ODFs from 3D intensity data in Chapter 2 have been released as the open-source Python package "Fiberorient" available for download at https://github.com/scott-trinkle/fiberorient. The package can also be installed with pip: `pip install fiberorient`

Raw diffusion data, connectivity matrices, and distance matrices for the construction of geometric and random surrogate graphs in Chapter 3 are available for download at https://knowledge.uchicago.edu/record/3310. Analysis and visualization tools developed for Chapter 3 have been released as the open-source Python package "Braingraphgeo" available for download at https://github.com/scott-trinkle/braingraphgeo. The package can also be installed with pip: `pip install braingraphgeo`.

References

1. Ramón y Cajal S. *Texture of the Nervous System of Man and the Vertebrates.* New York: Spring Science & Business Media 2002.

2. Kasthuri N, Hayworth KJ, Berger DR, et al. Saturated Reconstruction of a Volume of Neocortex. *Cell.* 2015;162:648–61.

3. Eberle A, Mikula S, Schalek R, Lichtman J, Knothe Tate M, Zeidler D. High-resolution, high-throughput imaging with a multibeam scanning electron microscope. *Journal of Microscopy.* 2015;259:114–120.

4. Stejskal EO, Tanner JE. Spin diffusion measurements: Spin echoes in the presence of a time-dependent field gradient. *The Journal of Chemical Physics.* 1965;42:288–292.

5. Lauterbur PC. Image formation by induced local interactions: Examples employing nuclear magnetic resonance. *Nature.* 1973;242:190–191.

6. Descoteaux M. High Angular Resolution Diffusion Imaging (HARDI). *Wiley Encyclopedia of Electrical and Electronics Engineering.* 2015:1–25.

7. Moseley ME, Cohen Y, Kucharczyk J, et al. Diffusion-weighted MR imaging of anisotropic water diffusion in cat central nervous system. *Radiology.* 1990;176:439–445.

8. Douek P, Turner R, Pekar J, Patronas N, Le Bihan D. MR color mapping of myelin fiber orientation. *Journal of Computer Assisted Tomography.* 1991;15:923–929.

9. Basser PJ, Mattiello J, Lebihan D. Estimation of the Effective Self-Diffusion Tensor from the NMR Spin Echo. *Journal of Magnetic Resonance, Series B.* 1994;103:247–254.

10. Basser PJ, Mattiello J, LeBihan D. MR diffusion tensor spectroscopy and imaging. *Biophysical journal.* 1994;66:259–67.

11. Pierpaoli C, Jezzard P, Basser PJ, Barnett A, Di Chiro G. Diffusion tensor MR imaging of the human brain. *Radiology.* 1996;201:637–648.

12. Callaghan PT, Eccles CD, Xia Y. NMR microscopy of dynamic displacements: K-space and q-space imaging. *Journal of Physics E: Scientific Instruments.* 1988;21:820–822.

13. Callaghan P. *Principles of Nuclear Magnetic Resonance Microscopy.* Oxford: Oxford University Press 1991.

14. Tuch DS. *Diffusion MRI of complex tissue structure.* PhD thesisMassachusetts Institute of Technology 2002.

15. Tuch DS. Q-ball imaging. *Magnetic Resonance in Medicine.* 2004;52:1358–1372.

16. Tournier JD, Calamante F, Gadian DG, Connelly A. Direct estimation of the fiber orientation density function from diffusion-weighted MRI data using spherical deconvolution. *NeuroImage.* 2004;23:1176–1185.

17. Tournier JD, Calamante F, Connelly A. Robust determination of the fibre orientation distribution in diffusion MRI: Non-negativity constrained super-resolved spherical deconvolution. *NeuroImage.* 2007;35:1459–1472.

18. Raffelt D, Tournier JD, Rose S, et al. Apparent Fibre Density: A novel measure for the analysis of diffusion-weighted magnetic resonance images. *NeuroImage.* 2012;59:3976–3994.

19. Jeurissen B, Descoteaux M, Mori S, Leemans A. Diffusion MRI fiber tractography of the brain. *NMR in Biomedicine.* 2019;32:e3785.

20. Sporns O, Tononi G, Kötter R. The Human Connectome: A Structural Description of the Human Brain. *PLoS Computational Biology.* 2005;1:e42.

21. Essayed WI, Zhang F, Unadkat P, Cosgrove GR, Golby AJ, O'Donnell LJ. White matter tractography for neurosurgical planning: A topography-based review of the current state of the art. *NeuroImage: Clinical.* 2017;15:659–672.

22. Basser PJ, Pajevic S, Pierpaoli C, Duda J, Aldroubi A. In vivo fiber tractography using DT-MRI data. *Magnetic Resonance in Medicine.* 2000;44:625–632.

23. Behrens T, Woolrich M, Jenkinson M, et al. Characterization and propagation of uncertainty in diffusion-weighted MR imaging. *Magnetic Resonance in Medicine.* 2003;50:1077–1088.

24. Smith RE, Tournier JD, Calamante F, Connelly A. Anatomically-constrained tractography: Improved diffusion MRI streamlines tractography through effective use of anatomical information. *NeuroImage.* 2012;62:1924–1938.

25. Smith RE, Tournier JD, Calamante F, Connelly A. The effects of SIFT on the reproducibility and biological accuracy of the structural connectome. *NeuroImage.* 2015;104:253–265.

26. Smith RE, Tournier JD, Calamante F, Connelly A. SIFT2: Enabling dense quantitative assessment of brain white matter connectivity using streamlines tractography. *NeuroImage.* 2015;119:338–351.

27. Jbabdi S, Woolrich MW, Andersson JL, Behrens TE. A Bayesian framework for global tractography. *NeuroImage.* 2007;37:116–129.

28. Mangin JF, Fillard P, Cointepas Y, Le Bihan D, Frouin V, Poupon C. Toward global tractography. *NeuroImage.* 2013;80:290–296.

29. Liewald D, Miller R, Logothetis N, Wagner HJ, Schüz A. Distribution of axon diameters in cortical white matter: an electron-microscopic study on three human brains and a macaque. *Biological Cybernetics.* 2014;108:541–557.

30. Basser PJ, Pierpaoli C. Microstructural and Physiological Features of Tissues Elucidated by Quantitative-Diffusion-Tensor MRI. *Journal of Magnetic Resonance, Series B.* 1996;111:209–219.

31. Novikov DS, Fieremans E, Jespersen SN, Kiselev VG. Quantifying brain microstructure with diffusion MRI: Theory and parameter estimation. *NMR in Biomedicine.* 2019;32:e3998.

32. Fieremans E, Novikov DS, Jensen JH, Helpern JA. Monte Carlo study of a two-compartment exchange model of diffusion. *NMR in Biomedicine.* 2010;23:711–724.

33. Fieremans E, Jensen JH, Helpern JA. White matter characterization with diffusional kurtosis imaging. *NeuroImage.* 2011;58:177–188.

34. Kroenke CD, Ackerman JJ, Yablonskiy DA. On the nature of the NAA diffusion attenuated MR signal in the central nervous system. *Magnetic Resonance in Medicine.* 2004;52:1052–1059.

35. Jespersen SN, Kroenke CD, Østergaard L, Ackerman JJ, Yablonskiy DA. Modeling dendrite density from magnetic resonance diffusion measurements. *NeuroImage.* 2007;34:1473–1486.

36. Zhang H, Schneider T, Wheeler-Kingshott CA, Alexander DC. NODDI: Practical in vivo neurite orientation dispersion and density imaging of the human brain. *NeuroImage.* 2012;61:1000–1016.

37. Assaf Y, Blumenfeld-Katzir T, Yovel Y, Basser PJ. AxCaliber: a method for measuring axon diameter distribution from diffusion MRI. *Magnetic resonance in medicine.* 2008;59:1347–1354.

38. Alexander DC, Hubbard PL, Hall MG, et al. Orientationally invariant indices of axon diameter and density from diffusion MRI. *NeuroImage.* 2010;52:1374–1389.

39. Tae WS, Byung-Joo H, Sung-bom P, Kang SH, Kim BJ. Current Clinical Applications of Diffusion-Tensor Imaging. *Journal of Clinical Neurology.* 2018;14:129–140.

40. Budde MD, Frank JA. Examining brain microstructure using structure tensor analysis of histological sections. *NeuroImage.* 2012;63:1–10.

41. Budde MD, Annese J. Quantification of anisotropy and fiber orientation in human brain histological sections. *Frontiers in Integrative Neuroscience.* 2013;7:1–8.

42. Khan AR, Cornea A, Leigland LA, Kohama SG, Jespersen SN, Kroenke CD. 3D structure tensor analysis of light microscopy data for validating diffusion MRI. *NeuroImage.* 2015;111:192–203.

43. Seehaus A, Roebroeck A, Bastiani M, et al. Histological validation of high-resolution DTI in human post mortem tissue. *Frontiers in Neuroanatomy.* 2015;9:1–12.

44. Schilling KG, Janve V, Gao Y, Stepniewska I, Landman BA, Anderson AW. Histological validation of diffusion MRI fiber orientation distributions and dispersion. *NeuroImage.* 2018;165:200–221.

45. Axer M, Strohmer S, Gräßel D, et al. Estimating Fiber Orientation Distribution Functions in 3D-Polarized Light Imaging. *Frontiers in Neuroanatomy.* 2016;10:1–12.

46. Mollink J, Kleinnijenhuis M, Cappellen van Walsum AM, et al. Evaluating fibre orientation dispersion in white matter: Comparison of diffusion MRI, histology and polarized light imaging. *NeuroImage.* 2017;157:561–574.

47. Wang H, Lenglet C, Akkin T. Structure tensor analysis of serial optical coherence scanner images for mapping fiber orientations and tractography in the brain. *Journal of Biomedical Optics.* 2015;20:036003.

48. Lefebvre J, Delafontaine-Martel P, Pouliot P, Girouard H, Descoteaux M, Lesage F. Fully automated dual-resolution serial optical coherence tomography aimed at diffusion MRI validation in whole mouse brains. *Neurophotonics.* 2018;5:045004.

49. Dyrby TB, Søgaard LV, Parker GJ, et al. Validation of in vitro probabilistic tractography. *NeuroImage.* 2007;37:1267–1277.

50. Dauguet J, Peled S, Berezovskii V, et al. Comparison of fiber tracts derived from in-vivo DTI tractography with 3D histological neural tract tracer reconstruction on a macaque brain. *NeuroImage.* 2007;37:530–538.

51. Seehaus AK, Roebroeck A, Chiry O, et al. Histological Validation of DW-MRI Tractography in Human Postmortem Tissue. *Cerebral Cortex.* 2013;23:442–450.

52. Donahue CJ, Sotiropoulos SN, Jbabdi S, et al. Using Diffusion Tractography to Predict Cortical Connection Strength and Distance: A Quantitative Comparison with Tracers in the Monkey. *The Journal of neuroscience.* 2016;36:6758–70.

53. Calabrese E, Badea A, Cofer G, Qi Y, Johnson GA. A Diffusion MRI Tractography Connectome of the Mouse Brain and Comparison with Neuronal Tracer Data. *Cerebral Cortex.* 2015;25:4628–4637.

54. Ourselin S, Bardinet E, Dormont D, et al. Fusion of Histological Sections and MR Images: Towards the Construction of an Atlas of the Human Basal Ganglia. in *Medical Image Computing and Computer-Assisted Intervention - MICCAI 2001* (Niessen WJ, Viergever MA. , eds.):743–751Springer, Berlin, Heidelberg 2001.

55. Jespersen SN, Leigland LA, Cornea A, Kroenke CD. Determination of Axonal and Dendritic Orientation Distributions Within the Developing Cerebral Cortex by Diffusion Tensor Imaging. *IEEE Transactions on Medical Imaging.* 2012;31:16–32.

56. Ju T, Warren J, Carson J, et al. 3D volume reconstruction of a mouse brain from histological sections using warp filtering. *Journal of Neuroscience Methods.* 2006;156:84–100.

57. Mikula S, Binding J, Denk W. Staining and embedding the whole mouse brain for electron microscopy. *Nature Methods.* 2012;9:1198–1201.

58. Mikula S, Denk W. High-resolution whole-brain staining for electron microscopic circuit reconstruction. *Nature Methods.* 2015;12:541–546.

59. Bonse U, Busch F. X-ray computed microtomography (μCT) using synchrotron radiation (SR). 1996.

60. Zehbe R, Haibel A, Riesemeier H, et al. Going beyond histology. Synchrotron microcomputed tomography as a methodology for biological tissue characterization: from tissue morphology to individual cells. *Journal of The Royal Society Interface.* 2010;7:49–59.

61. Dyer EL, Gray Roncal W, Prasad JA, et al. Quantifying Mesoscale Neuroanatomy Using X-Ray Microtomography. *eNeuro.* 2017;4:e0195–17.2017.

62. Ding Y, Vanselow DJ, Yakovlev MA, et al. Computational 3D histological phenotyping of whole zebrafish by X-ray histotomography. *eLife.* 2019;8.

63. Foxley S, Sampathkumar V, De Andrade V, et al. Multi-modal imaging of a single mouse brain over five orders of magnitude of resolution. *NeuroImage.* 2021:118250.

64. Trinkle S, Foxley S, Kasthuri N, La Rivière P. Synchrotron X-ray micro-CT as a validation dataset for diffusion MRI in whole mouse brain. *Magnetic Resonance in Medicine.* 2021:mrm.28776.

65. Foxley S, Domowicz M, Karczmar GS, Schwartz N. 3D high spectral and spatial resolution imaging of ex vivo mouse brain. *Medical Physics.* 2015;42:1463–1472.

66. Foxley S, Karczmar GS, Takahashi K. The effects of variations in tissue microstructure from postmortem rat brain on the asymmetry of the water proton resonance. *Magnetic Resonance in Medicine.* 2018;00:1–11.

67. Tournier JD, Calamante F, Connelly A. MRtrix: Diffusion tractography in crossing fiber regions. *International Journal of Imaging Systems and Technology.* 2012;22:53–66.

68. Veraart J, Fieremans E, Novikov DS. Diffusion MRI noise mapping using random matrix theory. *Magnetic Resonance in Medicine.* 2016;76:1582–1593.

69. Veraart J, Novikov DS, Christiaens D, Ades-aron B, Sijbers J, Fieremans E. Denoising of diffusion MRI using random matrix theory. *NeuroImage.* 2016;142:394–406.

70. Garyfallidis E, Brett M, Amirbekian B, et al. Dipy, a library for the analysis of diffusion MRI data. *Frontiers in Neuroinformatics.* 2014;8:8.

71. Schindelin J, Arganda-Carreras I, Frise E, et al. Fiji: an open-source platform for biological-image analysis. *Nature Methods.* 2012;9:676–682.

72. Tournier JD, Calamante F, Connelly A. Determination of the appropriate b value and number of gradient directions for high-angular-resolution diffusion-weighted imaging. *NMR in Biomedicine.* 2013;26:1775–1786.

73. Vescovi RF, Cardoso MB, Miqueles EX. Radiography registration for mosaic tomography. *Journal of Synchrotron Radiation.* 2017;24:686–694.

74. Gürsoy D, De Carlo F, Xiao X, Jacobsen C. TomoPy: A framework for the analysis of synchrotron tomographic data. *Journal of Synchrotron Radiation.* 2014;21:1188–1193.

75. Bigun J, Granlund GH. Optimal Orientation Detection of Linear Symmetry. in *Proceedings of the IEEE First International Conference On Computer Vision*(London):433–438IEEE 1987.

76. Alimi A, Ussou Y, Pierre-Simon J, Michalowicz G, Deriche R. An Analytical Fiber ODF Reconstruction in 3D Polarized Light Imaging. in *15th IEEE International Symposium on Biomedical Imaging (ISBI)*(Washington, D.C.):1276–1279 2018.

77. Deslauriers-Gauthier S, Marziliano P, Paquette M, Descoteaux M. The application of a new sampling theorem for non-bandlimited signals on the sphere: Improving the recovery of crossing fibers for low b-value acquisitions. *Medical Image Analysis.* 2016;30:46–59.

78. Deslauriers-Gauthier S, Marziliano P. Sampling Signals With a Finite Rate of Innovation on the Sphere. *IEEE Transactions on Signal Processing.* 2013;61:4552–4561.

79. Avants BB, Tustison NJ, Stauffer M, Song G, Wu B, Gee JC. The Insight ToolKit image registration framework. *Frontiers in neuroinformatics.* 2014;8:44.

80. Klein A, Andersson J, Ardekani BA, et al. Evaluation of 14 nonlinear deformation algorithms applied to human brain MRI registration. *NeuroImage.* 2009;46:786–802.

81. Avants BB, Epstein CL, Grossman M, Gee JC. Symmetric diffeomorphic image registration with cross-correlation: evaluating automated labeling of elderly and neurodegenerative brain. *Medical image analysis.* 2008;12:26–41.

82. Raffelt D, Tournier JD, Crozier S, Connelly A, Salvado O. Reorientation of fiber orientation distributions using apodized point spread functions. *Magnetic Resonance in Medicine.* 2012;67:844–855.

83. Daducci A, Canales-Rodriguez EJ, Descoteaux M, et al. Quantitative comparison of reconstruction methods for intra-voxel fiber recovery from diffusion MRI. *IEEE Transactions on Medical Imaging.* 2014;33:384–399.

84. Anderson AW. Measurement of fiber orientation distributions using high angular resolution diffusion imaging. *Magnetic Resonance in Medicine.* 2005;54:1194–1206.

85. Avants BB, Tustison NJ, Wu J, Cook PA, Gee JC. An Open Source Multivariate Framework for n-Tissue Segmentation with Evaluation on Public Data. *Neuroinformatics.* 2011;9:381–400.

86. Tournier JD, Calamante F, Connelly A. Improved probabilistic streamlines tractography by 2nd order integration over fibre orientation distributions. in *Proceedings of the International Society for Magnetic Resonance in Medicine*;1670 2010.

87. Titarenko S, Titarenko V, Kyrieleis A, Withers PJ, IUCr . A priori information in a regularized sinogram-based method for removing ring artefacts in tomography. *Journal of Synchrotron Radiation.* 2010;17:540–549.

88. Titarenko V, IUCr . Analytical formula for two-dimensional ring artefact suppression. *Journal of Synchrotron Radiation.* 2016;23:1447–1461.

89. Prell D, Kyriakou Y, Kalender WA. Comparison of ring artifact correction methods for flat-detector CT. *Physics in Medicine and Biology.* 2009;54:3881–3895.

90. Passingham RE. What we can and cannot tell about the wiring of the human brain. *NeuroImage.* 2013;80:14–17.

91. Griffa A, Baumann PS, Thiran JP, Hagmann P. Structural connectomics in brain diseases. *NeuroImage.* 2013;80:515–526.

92. Yeh C, Jones DK, Liang X, Descoteaux M, Connelly A. Mapping Structural Connectivity Using Diffusion MRI: Challenges and Opportunities. *Journal of Magnetic Resonance Imaging.* 2020:jmri.27188.

93. Glasser MF, Smith SM, Marcus DS, et al. The Human Connectome Project's neuroimaging approach. *Nature Neuroscience.* 2016;19:1175–1187.

94. Rubinov M, Sporns O. Complex network measures of brain connectivity: Uses and interpretations. *NeuroImage.* 2010;52:1059–1069.

95. Kaiser M. A tutorial in connectome analysis: Topological and spatial features of brain networks. *NeuroImage.* 2011;57:892–907.

96. Sizemore AE, Phillips-Cremins J, Ghrist R, Bassett DS. The importance of the whole: topological data analysis for the network neuroscientist. *Network Neuroscience.* 2018;3:656–673.

97. Latora V, Marchiori M. Efficient Behavior of Small-World Networks. *Physical Review Letters.* 2001;87:198701.

98. Sporns O, Betzel RF. Modular Brain Networks. *Annual Review of Psychology.* 2016;67:613–640.

99. Heuvel MP, Sporns O. Network hubs in the human brain. *Trends in Cognitive Sciences.* 2013;17:683–696.

100. Schilling K, Gao Y, Janve V, Stepniewska I, Landman BA, Anderson AW. Can increased spatial resolution solve the crossing fiber problem for diffusion MRI? *NMR in Biomedicine.* 2017;30:e3787.

101. Maier-Hein KH, Neher PF, Houde JC, et al. The challenge of mapping the human connectome based on diffusion tractography. *Nature Communications.* 2017;8:1349.

102. Thomas C, Ye FQ, Irfanoglu MO, et al. Anatomical accuracy of brain connections derived from diffusion MRI tractography is inherently limited. *Proceedings of the National Academy of Sciences.* 2014;111:16574–16579.

103. Schilling KG, Nath V, Hansen C, et al. Limits to anatomical accuracy of diffusion tractography using modern approaches. *NeuroImage.* 2019;185:1–11.

104. Aydogan DB, Jacobs R, Dulawa S, et al. When tractography meets tracer injections: a systematic study of trends and variation sources of diffusion-based connectivity. *Brain Structure and Function.* 2018;223:2841–2858.

105. Horvát S, Gămănuț R, Ercsey-Ravasz M, et al. Spatial Embedding and Wiring Cost Constrain the Functional Layout of the Cortical Network of Rodents and Primates. *PLOS Biology.* 2016;14:e1002512.

106. Ercsey-Ravasz M, Markov NT, Lamy C, et al. A Predictive Network Model of Cerebral Cortical Connectivity Based on a Distance Rule. *Neuron.* 2013;80:184–197.

107. Rubinov M, Ypma RJF, Watson C, Bullmore ET. Wiring cost and topological participation of the mouse brain connectome. *Proceedings of the National Academy of Sciences.* 2015;112:10032–10037.

108. Roberts JA, Perry A, Lord AR, et al. The contribution of geometry to the human connectome. *NeuroImage.* 2016;124:379–393.

109. Perinelli A, Tabarelli D, Miniussi C, Ricci L. Dependence of connectivity on geometric distance in brain networks. *Scientific Reports.* 2019;9:13412.

110. Supekar K, Musen M, Menon V. Development of Large-Scale Functional Brain Networks in Children. *PLoS Biology.* 2009;7:e1000157.

111. Jbabdi S, Sotiropoulos SN, Haber SN, Van Essen DC, Behrens TE. Measuring macroscopic brain connections in vivo. *Nature Neuroscience.* 2015;18:1546–1555.

112. Oh SW, Harris JA, Ng L, et al. A mesoscale connectome of the mouse brain. *Nature.* 2014;508:207–214.

113. Markov NT, Ercsey-Ravasz MM, Ribeiro Gomes AR, et al. A Weighted and Directed Interareal Connectivity Matrix for Macaque Cerebral Cortex. *Cerebral Cortex.* 2014;24:17–36.

114. Bota M, Sporns O, Swanson LW. Architecture of the cerebral cortical association connectome underlying cognition. *Proceedings of the National Academy of Sciences.* 2015;112:E2093–E2101.

115. Girard G, Caminiti R, Battaglia-Mayer A, et al. On the cortical connectivity in the macaque brain: A comparison of diffusion tractography and histological tracing data. *NeuroImage.* 2020;221:117201.

116. Ragan T, Kadiri LR, Venkataraju KU, et al. Serial two-photon tomography for automated ex vivo mouse brain imaging. *Nature Methods.* 2012;9:255–258.

117. Dong HW. *The Allen reference atlas: A digital color brain atlas of the C57Bl/6J male mouse.* Hoboken, NJ, US: John Wiley & Sons Inc 2008.

118. Chen H, Liu T, Zhao Y, et al. Optimization of large-scale mouse brain connectome via joint evaluation of DTI and neuron tracing data. *NeuroImage.* 2015;115:202–213.

119. Henderson JA, Robinson PA. Using Geometry to Uncover Relationships Between Isotropy, Homogeneity, and Modularity in Cortical Connectivity. *Brain Connectivity.* 2013;3:423–437.

120. Bullmore E, Sporns O. The economy of brain network organization. *Nature Reviews Neuroscience.* 2012;13:336–349.

121. Trinkle S, Foxley S, Wildenberg G, Kasthuri N, La Rivière P. The role of spatial embedding in mouse brain networks constructed from diffusion tractography and tracer injections. *NeuroImage.* 2021;244:118576.

122. Knox JE, Harris KD, Graddis N, et al. High-resolution data-driven model of the mouse connectome. *Network Neuroscience.* 2019;3:217–236.

123. Ypma RJF, Bullmore ET. Statistical Analysis of Tract-Tracing Experiments Demonstrates a Dense, Complex Cortical Network in the Mouse. *PLOS Computational Biology.* 2016;12:e1005104.

124. Gămănuţ R, Kennedy H, Toroczkai Z, et al. The Mouse Cortical Connectome, Characterized by an Ultra-Dense Cortical Graph, Maintains Specificity by Distinct Connectivity Profiles. *Neuron.* 2018;97:698–715.e10.

125. Foxley S, Wildenberg G, Sampathkumar V, Karczmar GS, Brugarolas P, Kasthuri N. Sensitivity to myelin using model-free analysis of the water resonance line-shape in postmortem mouse brain. *Magnetic Resonance in Medicine.* 2020:mrm.28440.

126. Tournier JD, Smith R, Raffelt D, et al. MRtrix3: A fast, flexible and open software framework for medical image processing and visualisation. *NeuroImage.* 2019;202:116137.

127. Hagberg AA, Schult DA, Swart PJ. Exploring network structure, dynamics, and function using NetworkX. *7th Python in Science Conference (SciPy 2008).* 2008:11–15.

128. Coletta L, Pagani M, Whitesell JD, Harris JA, Bernhardt B, Gozzi A. Network structure of the mouse brain connectome with voxel resolution. *Science Advances.* 2020;6:eabb7187.

129. Blondel VD, Guillaume JL, Lambiotte R, Lefebvre E. Fast unfolding of communities in large networks. *Journal of Statistical Mechanics: Theory and Experiment.* 2008;2008:P10008.

130. Newman MEJ. Analysis of weighted networks. *Physical Review E - Statistical Physics, Plasmas, Fluids, and Related Interdisciplinary Topics.* 2004;70:9.

131. Guimerà R, Amaral LA. Cartography of complex networks: Modules and universal roles. *Journal of Statistical Mechanics: Theory and Experiment.* 2005:1–13.

132. Girard G, Whittingstall K, Deriche R, Descoteaux M. Towards quantitative connectivity analysis: reducing tractography biases. *NeuroImage.* 2014;98:266–278.

133. Stadelmann C, Timmler S, Barrantes-Freer A, Simons M. Myelin in the central nervous system: Structure, function, and pathology. *Physiological Reviews.* 2019;99:1381–1431.

134. Knaap MS, Bugiani M. Leukodystrophies: a proposed classification system based on pathological changes and pathogenetic mechanisms. *Acta Neuropathologica.* 2017;134:351–382.

135. Arshad M, Stanley JA, Raz N. Test–retest reliability and concurrent validity of in vivo myelin content indices: Myelin water fraction and calibrated T1w/T2w image ratio. *Human Brain Mapping.* 2017;38:1780–1790.

136. Haller S, Kövari E, Herrmann FR, et al. Do brain T2/FLAIR white matter hyperintensities correspond to myelin loss in normal aging? A radiologic-neuropathologic correlation study. *Acta Neuropathologica Communications.* 2014;2:14.

137. Uddin MN, Figley TD, Marrie RA, Figley CR. Can T1w/ T2w ratio be used as a myelin-specific measure in subcortical structures? Comparisons between FSE-based T2w/ T2w ratios, GRASE-based T1w/ T2w ratios and multi-echo GRASE-based myelin water fractions. *NMR in Biomedicine.* 2018;31:e3868.

138. Mackay A, Whittall K, Adler J, Li D, Paty D, Graeb D. In vivo visualization of myelin water in brain by magnetic resonance. *Magnetic Resonance in Medicine.* 1994;31:673–677.

139. MacKay AL, Laule C. Magnetic Resonance of Myelin Water: An in vivo Marker for Myelin. *Brain Plasticity.* 2016;2:71–91.

140. Du YP, Chu R, Hwang D, et al. Fast multislice mapping of the myelin water fraction using multicompartment analysis of T2* decay at 3T: A preliminary postmortem study. *Magnetic Resonance in Medicine.* 2007;58:865–870.

141. Kwon OI, Woo EJ, Du YP, Hwang D. A tissue-relaxation-dependent neighboring method for robust mapping of the myelin water fraction. *NeuroImage.* 2013;74:12–21.

142. Lenz C, Klarhöfer M, Scheffler K. Feasibility of in vivo myelin water imaging using 3D multigradient-echo pulse sequences. *Magnetic Resonance in Medicine.* 2012;68:523–528.

143. Nam Y, Lee J, Hwang D, Kim DH. Improved estimation of myelin water fraction using complex model fitting. *NeuroImage.* 2015;116:214–221.

144. Sati P, Gelderen P, Silva AC, et al. Micro-compartment specific T2* relaxation in the brain. *NeuroImage.* 2013;77:268–278.

145. Hwang D, Kim DH, Du YP. In vivo multi-slice mapping of myelin water content using T2* decay. *NeuroImage.* 2010;52:198–204.

146. Gelderen P, Zwart JA, Lee J, Sati P, Reich DS, Duyn JH. Nonexponential T2* decay in white matter. *Magnetic Resonance in Medicine.* 2012;67:110–117.

147. Rosenbluth J. Central myelin in the mouse mutant shiverer. *Journal of Comparative Neurology.* 1980;194:639–648.

148. Du W, Karczmar GS, Uftring SJ, Du YP. Anatomical and functional brain imaging using high-resolution echo-planar spectroscopic imaging at 1.5 Tesla. *NMR in Biomedicine.* 2005;18:235–241.

149. Foxley S, Guo X, Karczmar GS. Functional brain imaging with high spectral and spatial resolution MRI at 3T. in *25th Annual Meeting and Exhibition of the International Society of Magnetic Resonance in Medicine*(Honolulu, HI, USA):5261 2017.

150. Du W, Du YP, Fan X, Zamora MA, Karczmar GS. Reduction of spectral ghost artifacts in high-resolution echo-planar spectroscopic imaging of water and fat resonances. *Magnetic Resonance in Medicine.* 2003;49:1113–1120.

151. Fan X, Du W, MacEneaney P, Zamora M, Karczmar G. Structure of the water resonance in small voxels in rat brain detected with high spectral and spatial resolution MRI. *Journal of Magnetic Resonance Imaging.* 2002;16:547–552.

152. Brouwer H. Evaluation of algorithms for automated phase correction of NMR spectra. *Journal of Magnetic Resonance.* 2009;201:230–238.

153. Al-Hallaq HA, Fan X, Zamora M, River JN, Moulder JE, Karczmar GS. Spectrally inhomogeneous BOLD contrast changes detected in rodent tumors with high spectral and spatial resolution MRI. *NMR in Biomedicine.* 2002;15:28–36.

154. Liu T, Khalidov I, Rochefort L, et al. A novel background field removal method for MRI using projection onto dipole fields (PDF). *NMR in Biomedicine.* 2011;24:1129–1136.

155. Schweser F, Deistung A, Lehr BW, Reichenbach JR. Quantitative imaging of intrinsic magnetic tissue properties using MRI signal phase: An approach to in vivo brain iron metabolism? *NeuroImage.* 2011;54:2789–2807.

156. Smith SM. Fast robust automated brain extraction. *Human Brain Mapping.* 2002;17:143–155.

157. Foxley S, Fan X, Mustafi D, et al. Sensitivity to tumor microvasculature without contrast agents in high spectral and spatial resolution MR images. *Magnetic Resonance in Medicine.* 2009;61:291–298.

158. Miller KL. Asymmetries of the balanced SSFP profile. Part I: Theory and observation. *Magnetic Resonance in Medicine.* 2010;63:385–395.

159. Tustison NJ, Avants BB, Cook PA, et al. N4ITK: improved N3 bias correction. *IEEE transactions on medical imaging.* 2010;29:1310–20.

160. Oouchi H, Yamada K, Sakai K, et al. Diffusion anisotropy measurement of brain white matter is affected by voxel size: Underestimation occurs in areas with crossing fibers. *American Journal of Neuroradiology.* 2007;28:1102–1106.

161. Bender B, Klose U. The in vivo influence of white matter fiber orientation towards B0 on T2* in the human brain. *NMR in Biomedicine.* 2010;23:1071–1076.

162. Lee J, Gelderen P, Kuo LW, Merkle H, Silva AC, Duyn JH. T2*-based fiber orientation mapping. *NeuroImage.* 2011;57:225–234.

163. Li W, Wu B, Avram AV, Liu C. Magnetic susceptibility anisotropy of human brain in vivo and its molecular underpinnings. *NeuroImage.* 2012;59:2088–2097.

164. Xu T, Foxley S, Kleinnijenhuis M, Chen WC, Miller KL. The effect of realistic geometries on the susceptibility-weighted MR signal in white matter. *Magnetic Resonance in Medicine.* 2018;79:489–500.

165. Oh SH, Kim YB, Cho ZH, Lee J. Origin of B0 orientation dependent R2* (=1/T2*) in white matter. *NeuroImage.* 2013;73:71–79.

166. Wharton S, Bowtell R. Fiber orientation-dependent white matter contrast in gradient echo MRI. *Proceedings of the National Academy of Sciences of the United States of America.* 2012;109:18559–18564.

167. Chen WC, Foxley S, Miller KL. Detecting microstructural properties of white matter based on compartmentalization of magnetic susceptibility. *NeuroImage.* 2013;70:1–9.